STRUCTURE AND MECHANISM OF MERB

by

GREGORY C. BENISON

(Under the direction of James Prestegard)

ABSTRACT

The three major naturally occurring forms of mercury- elemental, ionic, and organic- are widely distributed throughout the biosphere. All three forms are constantly interconverted by a variety of abiotic and biological mechanisms. Microbial mechanisms dominate the conversion of ionic mercury to organic mercury compounds, especially methyl mercury. Some microorganisms are also capable of transforming ionic or organic mercury into elemental mercury. This capability constitutes a detoxification mechanism due to the lower toxicity of elemental mercury relative to ionic or organic mercury. Organic and ionic mercury resistance is due to a dedicated set of plasmid-encoded mercury resistance genes (the *mer* operon.) *merR* is a regulatory gene. *merP* and *merT* are involved in mercury binding and transport. *merA* encodes for a reductase which reduces ionic mercury to elemental mercury using NADPH. *merB* encodes for an organomercurial lyase, which converts organomercurials into ionic mercury and a reduced organic product. In this study, the preparation of several mercury-containing MerB complexes is described. Of the complexes prepared, the most stable was identified by Nuclear Magnetic Resonance (NMR) and Extended X-Ray Absorption Fine Structure (EXAFS) spectroscopy as a complex of MerB, a mercuric ion, and one molecule of dithiothreitol (DTT). The mercuric ion is in a trigonal geometry, coordinated by both sulfur atoms of DTT as well as the sulfur atom of C96 from MerB. The stability of the MerB/Hg/DTT complex, even in the presence of a large excess of competing cysteine, was demonstrated by NMR and dialysis. The structure of the MerB/Hg/DTT complex was determined by NMR to 1.11 Å resolution. Due to the toxicity of mercuric ions, some mercury resistance proteins may employ a mechanism in which mercuric ions pass directly between the proteins, without diffusing through the cytosol. In order to investigate the possibility of direct transfer between MerB and MerA, the MerB/Hg/DTT complex was used as a substrate for MerA in an enzyme buffering test. The observed MerA activity was higher than the expected activity assuming free diffusion of the mercuric ion from MerB to MerA, which suggests that the mercuric ion can be directly transferred between the two enzymes.

INDEX WORDS: NMR, protein structure, mercury resistance, substrate channeling

STRUCTURE AND MECHANISM OF MERB

by

GREGORY C. BENISON

B.S., University of California, Davis, 1998

A Dissertation Submitted to the Graduate Faculty

of The University of Georgia in Partial Fulfillment

of the

Requirements for the Degree

DOCTOR OF PHILOSOPHY

ATHENS, GEORGIA

2004

STRUCTURE AND MECHANISM OF MERB

by

GREGORY C. BENISON

Approved:

Major Professor: James Prestegard

Committee: James Omichinski
Pascale Legault
Robert Scott
Michael Johnson

Electronic Version Approved:

Maureen Grasso
Dean of the Graduate School
The University of Georgia
May 2004

ACKNOWLEDGMENTS

This work was supported by a Graduate Research Fellowship from the National Science Foundation. I thank my advisors, my advisory committee, and the members of the Omichinski / Legault lab for their guidance and for teaching me the skills necessary to complete this project. I thank Dr. Robert Scott, members of the Scott group, and the Stanford Synchrotron Radiation Laboratory for the opportunity to perform EXAFS studies. I thank Dr. Michael Adams and the members of his lab for assistance with anaerobic sample preparation. I thank Ryan Slackman and Lindsay Hawkins for assistance in preparation of protein samples. I thank Dr. Anne O. Summers and Keith Pitts for the plasmid containing R831b MerB, and for introducing me to this interesting research problem. I thank Dr. Richard Meagher for the pNS2 MerA plasmid and for stimulating discussions about MerA and phytoremediation. I thank Dr. Frank Delaglio, Dr. Bruce Johnson, and Dr. Daniel Garrett for supplying NMR data processing and analysis programs, and Dr. Lewis Kay for supplying NMR pulse sequences. I thank Effie Greathouse for being a spouse of the highest quality. Finally, I would like to thank the authors of the many Free Software programs upon which I have relied. Their generous contributions have made the pursuit of this degree a much more rewarding and enjoyable experience.

TABLE OF CONTENTS

LIST OF FIGURES

LIST OF TABLES

CHAPTER 1

LITERATURE REVIEW

1.1 METHYLMERCURY- TOXICITY, OCCURRENCE, AND REMEDIATION

1.1.1 TOXICITY OF METHYLMERCURY AND OTHER ORGANOMERCURIALS

The human toxicity of organomercurial compounds was first widely observed in several accidental, large-scale poisoning episodes [1]. In the first reported, consumption of fish contaminated with methylmercury derived from a nearby chemical factory led to large-scale poisoning in Japan from 1953-1960. A common name for methylmercury poisoning, "Minamata disease", is derived from this incident. In another large episode, organomercurial compounds used as preservatives on grain led to a large-scale poisoning in Iraq in 1970.

The toxicity of organomercurial compounds has been described at scales ranging from the whole organism to single molecules. At the organismal level, clinical symptoms of acute methylmercury poisoning are different from poisoning by elemental or ionic mercury. The early symptoms are lesions on nervous tissue, followed by loss of sensory and motor skills, and finally death [2]. Following initial observations of methylmercury's human toxicity in the Minamata episode, animal studies further clarified the target organs of the poison [3, 4]. Many organs can be affected, although the nervous system is the primary target. Methylmercury crosses the blood-brain barrier more easily than other forms of mercury do [5], probably due to its hydrophobicity. At the cellular level, it has been demonstrated that methylmercury disrupts many cellular signalling pathways and leads to

apoptosis [6]. At the molecular level, the toxicity of ionic mercury and organomercurials is due to their ability to bind almost any available thiol group in biological molecules [7].

1.1.2 Occurrence of Organomercurials

Large-scale, acute poisonings due to direct industrial use of organomercurials such as those seen in Iraq and Japan are less likely to occur today due to the higher awareness of the dangers of mercury. There are still some areas of the world in which acute methylmercury pollution is a problem [8]. Perhaps a broader problem is the low level of methylmercury pollution that can appear in unexpected places, through indirect means [9]. The mechanisms for this type of pollution are discussed below.

Mercury, like other metals, differs fundamentally from organic pollutants in that it will never be completely destroyed [10]. For example, a substance like dioxin might be just as harmful as methylmercury, but it would be possible to devise a remediation scheme which converts dioxin to completely harmless substances. In contrast, methylmercury can only be relocated or transformed to other, perhaps less toxic, mercury compounds. However, whatever form the mercury takes, it is always a candidate for reconversion to methylmercury, as long as it remains in the biosphere. Therefore, any consideration of methylmercury pollution must take into account the entire global cycle of mercury, including its movement and chemical transformation.

Mercury exists in the biosphere in a variety of forms, and in a variety of locations [11]. The primary forms, from most abundant to least, are elemental mercury (Hg(0)), ionic mercury (Hg(II)), methylmercury (MeHg), and dimethylmercury (Me_2Hg). The organic forms are usually several orders of magnitude less abundant than the inorganic forms. For example, in open ocean waters, total mercury content is usually near 1 pM, whereas organic mercury is typically below 50 fM [12]. There is a large pool of atmospheric mercury consisting mainly of Hg(0), but with small amounts of the other mercury species [13].

All of the various forms of mercury can move between different portions of the biosphere through a variety of mechanisms. For example, there is a large emission of mercury from the ocean into the atmosphere, amounting to thousands of tons per year [14]. Increases in terrestrial mercury content can be traced to increased atmospheric deposition [9], and the rate of deposition depends on many atmospheric and terrestrial conditions [13]. Mercury in the elemental form in the atmosphere can remain mobile for years, dispersing over a particularly wide area, while other mercury species are redeposited on land in a shorter time [12]. One of the most important transport processes is the bioaccumulation of methylmercury in higher organisms such as fish [15, 16, 17].

Equally important to the transportation of mercury throughout the biosphere is its transformation between its various forms [18]. There are both abiotic and biotic mechanisms for the interconversion of the forms of mercury [11]. For the interconversion of organomercurials and inorganic mercury, biological transformation by microorganisms is generally the fastest mechanism. For example, the rate of abiotic methylmercury demethylation in lakes has been measured at near 10^{-6} s^{-1}, corresponding to a half life of several months [19]. In contrast, microorganisms can achieve an equilibrium between inorganic and methyl mercury within several days [15, 20]. Many types of microorganism are capable of methylating inorganic mercury [18, 11, 21, 22]. The methylation appears to be accidental; that is, it is not the consequence of a dedicated mercury methylation pathway, but rather a side product of many ordinary metabolic methylation pathways [23, 24].

Human activities have altered the environmental distribution of organomercurials in three major ways. The first is the direct introduction of organomercurials as either intended or accidental products of industrial activities. This type of introduction was the cause of the most major acute poisoning episodes [1]. Due to increasing awareness about the dangers of organomercurials, this type of introduction is becoming less likely. Now, human activity is likely to increase the incidence of organomercurials through two less direct

ways: by introducing inorganic mercury which can then be methylated, or by altering conditions in a way that promotes mercury methylation.

An increase in total mercury in the biosphere is clearly attributable to human activity [11]. Many industrial activities have involved taking mercury from sources outside of the biosphere, such as coal mines or mercury ore. Because there is generally no mechanism which returns mercury to these sources, all of the extracted mercury becomes distributed throughout the biosphere, increasing the total mercury available for methylation. For example, centuries of silver mining in South America released tremendous amounts of mercury, and gold mining continues to do so to a smaller extent [25]. The most prominent modern input of mercury into the biosphere is the combustion of coal, accounting for thousands of tons per year [26, 13].

Even where there is no obvious anthropogenic source of inorganic or organic mercury, organomercury levels can still increase through anthropogenic influences on the rate of methylation. One place in particular where this phenomenon is observed is in dammed rivers [27]. It is believed that the increase in sediment organic matter and creation of anoxic environments promotes methylation in dammed reservoirs by anaerobic bacteria. These conditions have been shown in laboratory experiments to promote methylation by anaerobic, sulfate-reducing bacteria [28]. This source of methylmercury is significant enough to cause advisories on the consumption of mercury-contaminated fish.

1.1.3 Remediation of Methylmercury Pollution

Due to the established dangers of mercury pollution, there are efforts both to reduce the amount of mercury released, and to remediate sites already contaminated with inorganic or organic mercury. Remediation methods for mercury and other pollutants can be categorized into non-biological and biological techniques [29]. Some non-biological methods intend to prevent the migration of mercury pollutants, but not to actually remove them.

$$R - Hg^{+} \xrightarrow{MerB} Hg^{++} + RH$$

$$Hg^{++} \xrightarrow{MerA} Hg(0)$$

Figure 1.1: Bacterial detoxification of organic mercury.

Examples are solidification of contaminated soil to prevent leaching, construction of barriers against leaching, and complete removal of soil. Other methods actually remove mercury from contaminated material, such as by heating to induce vaporization.

As an alternative to physical remediation methods, several methods are under development which utilize a set of proteins found in certain strains of mercury-resistant bacteria. Resistance to organomercurial compounds is due to a two-step process (Figure 1.1) mediated by two enzymes, MerA and MerB [30]. In the first step, an organomercurial lyase (MerB) cleaves the carbon-mercury bond, resulting in a mercuric ion and a reduced organic product. In the second step, the enzyme mercuric reductase (MerA) reduces the mercuric ion to elemental mercury. The conversion to a neutral mercury atom constitutes detoxification, because the Hg(0) is much less toxic to the cell than is either HgR^{+} or Hg(II), and Hg(0) can easily leave the cell due to its volatility.

One approach for using the MerA/MerB system in organomercury remediation has been to employ mercury-resistant bacteria themselves in polluted areas [31]. This approach is limited due to the relatively small biomass of the bacteria [32]. In one interesting application of mercury-resistant microbes, a bioreactor has been designed which is very efficient at removing ionic mercury from industrial wastewater flows [33]. In addition to the high efficiency of mercury removal, this method also promises to be considerably cheaper than non-biological alternatives.

The technique of using plants to clean up pollutants is known as phytoremediation, and is in use or under development for a wide variety of pollutants [10, 34]. The types of subject molecules range from organic solvents, to explosives such as TNT, to metals, including mercury. In some cases, organisms can be found which naturally degrade the target compounds. In other cases, such as for methylmercury, it is necessary to genetically modify the organisms. Plants offer many potential advantages for remediation [10]. Their large biomass and large amount of available energy from sunlight can be tapped to process pollutants faster than microbes can. Phytoremediation promises to be cheaper than physical remediation methods. It also avoids undesirable side effects associated with physically moving large amounts of soil or sediment. Also, in addition to actually removing pollutants, the plants can provide the benefit of simply maintaining a root system in areas where other, non-resistant plants may not grow.

Phytoremediation is a potentially very useful way of using the mercury resistance genes found in bacteria [35]. Initial studies have demonstrated that bacterial mercury resistance proteins can be inserted into plants which then become mercury-resistant. *Arabidopsis* plants expressing MerA are capable of growing on concentrations of inorganic mercury several orders of magnitude higher than what wild-type plants can tolerate [36]. Further, the plants have been shown to release elemental mercury into the air, and produce a dramatic decline in the mercury content of their growth media [34]. Because the best choice of plant species for a particular remediation task will depend on the location, it is desirable to have a variety of mercury-resistant species. For this reason, an inorganic-mercury-resistant yellow poplar tree has been developed as well [32]. Resistance to organic mercury compounds, as well as inorganic mercury, is achieved when both *merB* and *merA* are inserted into the plants [35]. The doubly-transformed plants are able to survive on organic mercury concentrations an order of magnitude higher than normal. Elemental mercury is expired, demonstrating that the full bacterial detoxification pathway has been replicated in plants. A somewhat surprising observation was that plants

Table 1.1: Most common proteins of the *mer* operon [39].

MerA	Reduce mercuric ion Hg^{++} to elemental mercury, $Hg(0)$
MerB	Cleave carbon-mercury bonds in a wide variety of substrates
MerP	Periplasmic protein involved in mercury binding and transport
MerT	Membrane protein; transports Hg^{++} across the cell membrane
MerR	Regulatory protein for the *mer* operon

transformed only with *merB*, but not with *merA*, were also resistant to organomercurials [37], although to a lesser extent. The mechanism may have to do with sequestration of the mercuric ions.

1.2 Mercury Resistance Proteins

Bacterial resistance to inorganic and organic mercury has been observed in a variety of bacterial strains [38]. Since the first observations of mercury resistance, it has been discovered that the resistance is due to a dedicated set of mercury resistance genes which are regulated together and known as the *mer* operon [39]. The genes of the *mer* operon are summarized in Table 1.1. The *mer* operon occurs in a large variety of bacteria, and tends to occur on transferable elements such as transposons and plasmids [11]. There has been a significant amount of research on the structures and mechanisms of the proteins involved in mercury resistance [30, 40].

1.2.1 Transport and Regulation

The expression of mercury resistance proteins occurs only in response to the presence of mercury [40]. The *mer* operon is regulated by the *merR* gene [41]. Even in the absence of mercury, MerR remains associated with the *mer* operon regulatory region as well as with RNA polymerase, allowing a fast response to mercury influx [42]. Mercury causes a

conformational change in MerR, which in turn causes a conformational change in DNA that activates expression. The mechanism of mercury binding to MerR has been described by extended X-Ray absorption fine structure spectroscopy (EXAFS), secondary structure predictions, and circular dichroism spectroscopy [43]. The core domain involved in mercury binding contains a helix with a pair of cysteine residues at one end, and a lone cysteine at the other. MerR is a dimer, and in the dimer structure one of these cysteine-containing helices from each subunit come together in an antiparallel fashion to form a three-coordinate mercury binding site.

There is a dedicated transport system for bringing mercuric ions into the cell, where they will be reduced by mercuric reductase [40]. The mercuric ion transport system consists of the periplasmic protein MerP and the membrane transporter MerT [44]. The role of MerP is to scavenge periplasmic mercuric ions and transfer them to MerT for transport into the cytosol. The three-dimensional structure of MerP has been solved by NMR spectroscopy in both the free and mercury-bound states [45], revealing a ferredoxin-like $\alpha - \beta$ fold. MerP possesses two cysteines in a CXXC mercury-binding motif. Less is known about the structure of MerT, although it is predicted to be a transmembrane helix bundle [11]. No MerT structure has yet been solved. There are two cysteine pairs (one on the cytosolic face, and one on the periplasmic face) believed to be involved in mercuric ion transport.

It is somewhat unusual that there is a transport system dedicated to the import of a toxic substance; it is more common for there to be a transport system dedicated to the efflux of toxic substances. However, there is ample evidence that the import system enhances mercury resistance. Strains retaining the mercuric reductase and regulatory gene, yet lacking the transport system, have a reduced resistance to mercury [44]. In the opposite situation, when the mercury transport ability is intact but there is no functional mercuric reductase, cells become hypersensitive; they are more sensitive to mercury than cells lacking the *mer* operon entirely [46].

1.2.2 ORGANOMERCURIAL LYASE

Some, but not all, *mer* operons include a MerB gene, which encodes for an organomercurial lyase [39]. *mer* operons containing MerB confer resistance to organomercurial substances as well as inorganic mercury. Apparently the organomercurial substrates enter the cytosol via diffusion due to their hydrophobicity; there is no dedicated organomercurial import system. MerB has been shown *in vitro* to cleave the carbon-mercury bond of a wide variety of substrates [47]. There are several sequenced MerB genes from a variety of bacterial sources. Most have significant homology to each other in both primary sequence and predicted secondary structure, but little to no homology to other known proteins [48]. No three-dimensional structure of a MerB protein has yet been solved. One feature apparently conserved among MerB proteins from disparate sources is a set of cysteine residues. On the basis of predicted secondary structure and sequence homology, MerB genes from a variety of bacterial hosts were grouped into three families A, B, and C [48]. A representative member of family A is the MerB gene from plasmid R831b. R831b contains four cysteine residues: C96, C117, C159, and C160. C96 and several surrounding residues are strongly conserved, and C96 is essential for catalytic activity. C117 is also strongly conserved. This would seem to indicate an important catalytic role for C117; however, thiol modification evidence suggests that it is buried and plays a structural role instead [48]. About half of the sequences classified into family A contain an adjacent pair of cysteines at C159/C160. In the R831b MerB gene, C159 is essential for catalysis. C160 is not essential, but mutants lacking this cysteine are catalytically impaired. The other half of the sequences classified into family A have only a single cysteine in the C159/C160 region, but have an additional pair of cysteine residues located near the carboxy terminus. Because the paired cysteine motif at C159/C160 in R831b has been shown to have an important role in optimum catalytic activity, it is likely that the paired cysteine motif found at the carboxy terminus takes over this role in sequences lacking one of the C159/C160 pair.

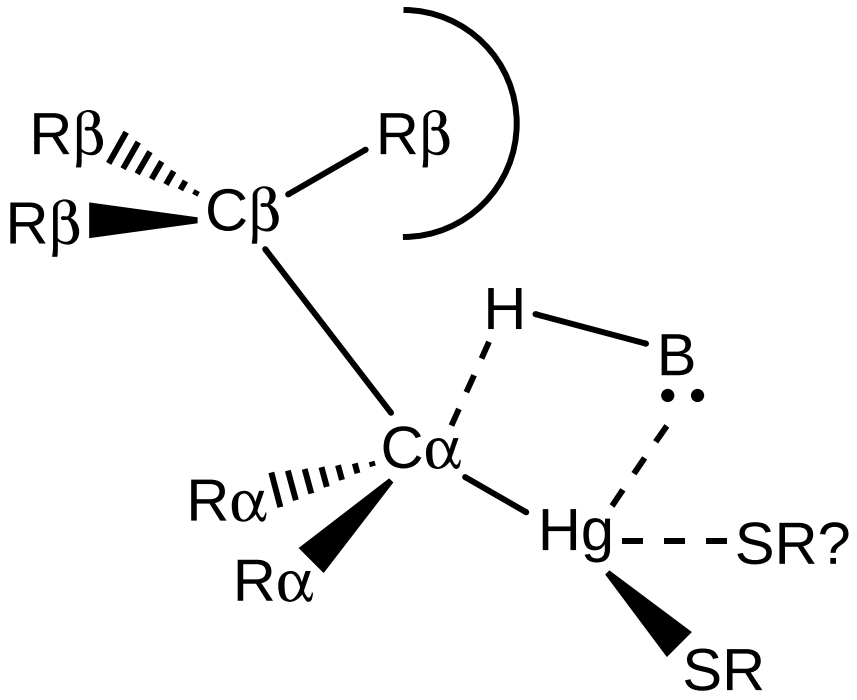

Figure 1.2: Concerted S_E2 mechanism for carbon-mercury bond cleavage by MerB [47].

The reaction mediated by MerB can be divided roughly into three stages: substrate binding, carbon-mercury bond cleavage, and product release. Of these three, the carbon-mercury bond cleavage step is by far the best understood. Studies using a variety of organomercurial substrates demonstrated that the reaction occurs via a concerted S_E2 mechanism [47]. In this mechanism, an electrophile (H^+ in this case) attacks the carbon atom from the same side as the mercury atom, resulting in retention of stereochemistry at C_α (see Figure 1.2). Electron-donating (eg. methyl) substituents on C_α tend to enhance the reaction rate; for example, ethyl mercury reacts faster than methyl mercury. The slower rate observed with heavily β-substituted organomercurials such as neopentyl mercuric chloride is probably due to steric clash between the β substituents and the attacking electrophile (Figure 1.2.)

Although carbon-mercury bonds are generally resilient and require harsh conditions for cleavage, there are several known non-enzymatic mechanisms for this reaction, which provide insight into the MerB mechanism. These reactions involve a variety of reagents but have a common theme: activation of the mercury atom by nucleophilic ligands, followed by protonolysis of the carbon-mercury bond. Examples of nucleophiles used in this reaction include iodide ions [49], and bromide ions [50]. The limiting factor in these reactions seems to be the formation of organomercurial substrates with high (eg. three) coordination numbers. Once the ligands are present, protonolysis is relatively easy. This is why multidentate ligands are more effective in promoting catalysis. For example, when vicinal dithiols are used as ligands to promote carbon-mercury bond cleavage [51], the required conditions are less harsh than what is needed with simple monovalent ligands like iodide, but still more harsh than the conditions under which MerB operates. In one dramatic example, a tridentate phosphine compound promotes protonolysis under very mild temperature and pH conditions [52]. It is reasonable to expect that MerB accomplishes its reaction in a similar manner: by coordinating the mercury atom with a high number (probably three) of thiol ligands and then providing a proton for cleavage. The arrangement of activating nucleophiles in MerB must be particularly favorable, because the enzyme actually operates optimally under basic conditions [53]. The required thiols could come from either a cysteine residue, or one of the obligate exogenous thiols as described below.

It has been shown *in vitro* that MerB requires exogenous thiols for turnover [47]. Most mono-thiol compounds such as cysteine promote catalysis, but dithiols such as dithiothreitol (DTT) do not. It was subsequently shown that DTT, even in small amounts, inhibits the reaction even in the presence of monothiols [48]. Further, it was shown that the turnover rate continues to increase with increasing monothiol concentration, even to concentrations as high as 20 mM. These thiols may be required as mercury-activating nucleophiles, as

described above, but there are other conceivable roles as well, such as preventing non-specific mercury binding to the protein, or promoting product release.

1.2.3 MERCURIC REDUCTASE

The mercuric reductase encoded by *merA* is present in all *mer* operons and performs the key step of reducing ionic mercury Hg(II) to elemental mercury Hg(0)[40]. MerA is similar in sequence, structure, and mechanism to other members of the disulfide oxidoreductase family of enzymes [54, 55, 56, 57]. Like other members of the family, MerA requires FAD and NADPH cofactors [58]. The two electrons required for reduction originate on NADPH, from there pass to FAD, from there to a redox-active disulfide pair, and finally to the substrate. MerA contains two structural features absent from other members of the disulfide oxidoreductase family. One is a short (~ 20) residue carboxyl terminal extension containing a pair of adjacent cysteines [55]. The second is an amino terminal domain homologous to MerP [40]. This amino terminal domain is easily lost during purification of the protein, and does not appear necessary for catalytic activity *in vitro* [59]. Both the amino terminal and carboxyl terminal extensions are less well defined than the core of the molecule in the X-ray crystal structure [56]. MerA is dimeric in its native form. The active site is composed of the NADPH and FAD groups, the redox-active disulfide, and the carboxyl terminal cysteine pair from the opposite monomer. It has been proposed that this arrangement allows an “alternating sites” mechanism, in which the two active sites cycle between a high- and low-affinity mercury-binding state [60].

The mechanism of MerA is a complicated, multi-step process. The reaction rate is strongly dependent on buffer thiol conditions [59], and all multiple-turnover assays to date depend on millimolar buffer thiol concentrations [11]. This may be due, in part, to the formation of a NADPH-Hg complex in the absence of thiols [61]. There is ample evidence, from studies involving mutagenesis of the cysteine residues and single-turnover observation of the electronic absorption spectrum of the cofactors, that the reaction begins with

the replacement of buffer thiols on Hg(II) by the carboxyl terminal cysteine pair [62, 63]. In single-turnover experiments it was shown that the carboxyl terminal cysteines are not required for the reduction step, and that when the substrate lacks thiol ligands, reduction actually happens significantly faster than wild-type turnover even when the carboxyl terminal cysteines are missing [62]. This observation that removal of buffer thiols can be rate-limiting is one explanation for the observed strong dependence of steady-state rate on the buffer thiol composition. From the carboxyl terminal cysteines, the mercuric ion passes to the redox-active disulfide pair. When the enzyme does not have both reduced FAD and NADPH present, it can accumulate in a form containing the mercuric ion bound in bicoordinate geometry by the redox active disulfide pair; this form was observed by extended X-ray absorption fine structure (EXAFS) [64].

1.3 Direct transfer of mercuric ions

There are at least three places within the mercury resistance pathway where it has been proposed that mercuric ions pass directly between the proteins, without diffusing through the cytosol or periplasmic space: from MerP to MerT, from MerT to MerA, and from MerB to MerA. Each of these direct transfer mechanisms would minimize the opportunity for highly toxic mercuric ions to bind to other cellular components.

1.3.1 MerP to MerT

The best evidence for direct transfer within the bacterial mercury resistance system is in the case of MerP-MerT transfer. There is a low abundance of small thiols in the periplasm, and MerP has a high affinity for mercury [11]. Therefore, in the absence of direct transfer, it is not clear how mercuric ions would diffuse from MerP to MerT. There is also more direct evidence available from a MerP mutant lacking one of its cysteines [65]. This mutant blocks mercuric ion uptake by MerT, probably through the formation

of a MerP/Hg/MerT complex involving the remaining cysteine on MerP and one or both of the periplasmic-face MerT cysteines. This model could be better supported by a direct observation of the MerP/Hg(II)/MerT complex. It may be difficult, however, to obtain such a complex between the soluble MerP and the membrane-bound MerT in a form suitable for structural study.

1.3.2 MerT to MerA

It has also been proposed that direct transfer takes place between the cytosolic side of MerT and MerA [11]. It was originally proposed that the paired cysteines of the amino terminal domain of MerA might be involved in a direct transfer of mercury from the cytosolic face of MerT [66]. It was later shown that this is at least not always true, because even if the amino terminal cysteines of MerA are removed, the bacterium can still possess a mercury-resistant phenotype [67]. Although this does not rule out the possibility of direct MerT-MerA transfer involving the amino terminal domain, it does show that there must be at least one other mechanism. There are at least two reasonable alternatives. One is transfer mediated by low molecular weight thiols. The other is transfer mediated by the carboxyl terminal cysteine pair of MerA. Although there is presently lack of clear evidence for the importance of the amino terminal domain of MerA, the observation that this domain is highly conserved suggests that there is some function. More recent work indicates that the amino terminal domain may be important under some thiol conditions, but not others [11]. Specifically, the amino terminal domain may be important when thiol concentrations are low, or the thiol molecular weight is high. So the role of the amino terminal domain of MerA, including the possibility of direct transfer from MerT, remains an open question.

1.3.3 MerB to MerA

Direct transfer between MerB and MerA has also been proposed [40]. This type of direct transfer between subsequent enzymes of a metabolic pathway has been termed substrate channeling (see Figure 1.3.) Although there is currently no published evidence for or against substrate channeling between MerB and MerA, the biological implications of this transfer seem particularly large, because MerB converts an organomercurial toxin into a mercuric ion, which is actually more reactive. Presumably it would be of physiological benefit to the cell if MerB did not release its toxic mercuric ion product directly into the cytoplasm.

1.3.4 Other Examples of Substrate Channeling

Outside of the mercury resistance pathway, there are numerous examples of proposed substrate channeling [69, 70, 71, 72]. The evidence for channeling usually consists of some combination of kinetic experiments and a structural basis for the proposed interaction between the enzymes in question. The number of different kinds of kinetic tests for substrate channeling remains small, although there is variation in their implementation.

In the isotope dilution method [73, 74], the second enzyme in the pathway (E2 in Figure 1.3) is presented with intermediate metabolite X from two sources: from the reaction catalyzed by the first enzyme E1, and by direct introduction of X into the reaction mixture. An isotopic label is applied to only one of these sources. The presence or absence of the label in the product then indicates which source of intermediate metabolite X is used by the second enzyme, E2.

Another method is based on the transient kinetics of intermediate X buildup and product P formation. The channeling and free diffusion hypotheses make different predictions about these rates, allowing a distinction between the two mechanisms. This argu-

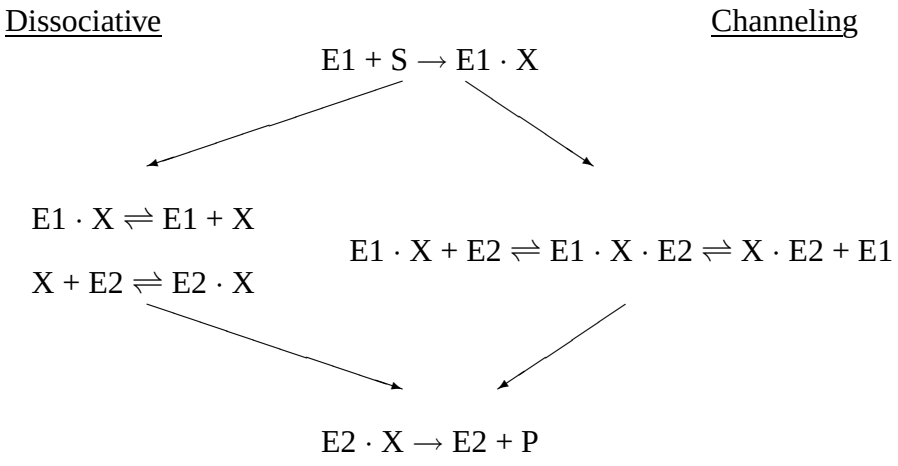

Figure 1.3: Dissociative vs. channeling mechanism for metabolite transfer in sequential reactions, using the notation of Ovadi [68]. The initial substrate S is converted into the final product P by two sequential enzymatic reactions catalyzed by enzymes E1 and E2. The intermediate metabolite X is the product of the reaction catalyzed by the enzyme E1. X is also the substrate for the reaction catalyzed by the enzyme E2. In the dissociative mechanism (left), the E1-X complex dissociates, yielding free X in solution. X then diffuses to and binds E2 in the second step. In the channeling mechanism (right), the E1-X complex binds E2 to yield a transient E1-X-E2 complex. E1 then dissociates from this complex to yield the X-E2 complex. In no part of the channeling mechanism does metabolite X exist freely in solution.

ment has been used to find evidence both for substrate channeling [75, 76, 77], and against it [78, 79].

The competing reaction method measures the coupled reaction of the putative channeling pair in the presence of a third enzyme which can compete for the intermediate metabolite X. The channeling hypothesis predicts that the intermediate will not be available to this third enzyme [80].

The enzyme buffering method is based on a comparison of the expected and observed steady-state rate of the E2 reaction in the presence of a large amount of the first enzyme, E1, and the intermediate metabolite, X [72]. Because there is no substrate S present, the first enzyme E1 does not catalyze any reaction; rather, it serves only to sequester free metabolite X. If the dissociation constant for E1-X is known, and the kinetic behavior of E2 with respect to free X is known, a predicted rate can be calculated, assuming only free diffusion of the intermediate metabolite. If the observed rate is higher than expected, then the diffusion hypothesis must be false, and the most likely alternative explanation is substrate channeling. This method was used to argue for channeling of NADH between many glycolytic enzymes [69, 81], and between mitochondrial dehydrogenases and NADH:ubiquinone oxidoreductase complex I [82, 83]. Some of these examples have been challenged because the method is sensitive to errors in the measured kinetic constants and the purity of the enzymes used [84]. There has also been considerable confusion surrounding this method because it can only offer either a conclusion of substrate channeling (when the observed and expected rates are different), or no conclusion at all (when the rates are not different). For many of the proposed instances of channeling in glycolytic enzymes, it is also possible to find substrate concentration regimes where the method is inconclusive [85, 86]. As with any method, it is important to consider whether the conditions *in vitro* under which channeling can be demonstrated are similar to the conditions *in vivo*.

The most recent kinetic method for the study of substrate channeling is the one developed by Geck and Kirsch [87]. In this method, the E1-E2 coupled reaction rate is measured in the presence of a catalytically impaired enzyme $E1^*$. If $E1^*$ is still capable of interacting with E2 in the same manner as normal E1, yet $E1^*$ cannot complete its reaction, then the substrate channeling hypothesis predicts that increasing amounts of $E1^*$ will decrease the overall reaction rate as $E1^*$ competes with E1 for E2. The advantage of this method is that, unlike enzyme buffering, it can be conclusive either for or against substrate channeling. The Geck-Kirsch method also avoids some potential problems associated with the large amounts of E1 required for enzyme buffering. The original implementation of this method concluded against channeling of oxaloacetate in a part of glutamate metabolism. A subsequent study used the method (in a different enzyme system) to conclude in favor of substrate channeling of β-aspartyl phosphate between aspartate kinase and aspartate semialdehyde dehydrogenase in the aspartate synthesis pathway [88].

The known degree of association between enzyme pairs involved in substrate channeling ranges all the way from covalent attachment of the two, to very transient association. In the enzyme carbamoyl phosphate synthase, channeling of ammonia occurs between active sites which are on the same monomer, yet separated by many tens of angstroms [89]. In other examples, the active sites involved in channeling are on different subunits of tightly associated quaternary structures. This is the case in tryptophan synthase [70], lumazine synthase / riboflavin synthase [75], and the pyruvate dehydrogenase complex [90]. For most of the proposed channeling pairs among glycolytic enzymes, no stable complex has been isolated, but transient association can be detected using gel filtration [91, 92].

It is supportive of the channeling hypothesis if, in addition to evidence for association between the enzymes, there is a structural basis for the transfer of the metabolite from one active site to the other. In the case of tryptophan synthase, it is well established that indole is channeled through a long hydrophobic tunnel from one active site to another active

site on a different monomer [70]. It has even been shown that mutations which block the tunnel impair channeling [79]. In ferrochelatase from the heme synthesis pathway, there is a mutation on the protein surface which impairs *in vivo* but not *in vitro* activity, implying that the residue is involved in a transient association [93]. The structure of aconitase revealed a protein recognition domain near the active site which may be important for channeling [94]. The pyruvate dehydrogenase complex has long "arms" which are known to mediate transfer of intermediates between distant active sites [90]. Simulations have shown that some degree of channeling can occur due to an electric field that favors substrate migration between two active sites, even if there is no physical linkage between them [95].

1.4 Structure Determination

1.4.1 Heteronuclear NMR

Early protein structure determinations by Nuclear Magnetic Resonance (NMR) were performed on samples of natural isotopic abundance, and were limited to proteins of less than $\sim$10 kDa molecular weight [96]. The adoption of isotopic labelling with ^{15}N and ^{13}C extended the size limit for NMR structure determination [97, 98, 99]. The main advantages of this technique are increased separation of NMR signals through the well-dispersed heteronuclear dimensions, which can allow complete assignments [100], as well as better transfer of magnetization through large single-bond scalar couplings [101]. The increased number of assignments allows the assignment of a greater number of Nuclear Overhauser (NOE) restraints, which is the most important factor in determining the resolution of a structure [102].

1.4.2 DEUTERATION

Extension of NMR structure determination to molecular weight above ∼20 kDa is limited mainly by the relaxation properties of proteins. As molecular weight increases, transverse relaxation time decreases, leading to a decrease in signal to noise ratio [103]. Because much of the relaxation of heteronuclei is due to their directly attached protons, a significant decrease in heteronuclear relaxation rate can be achieved by replacing protons with deuterons [104, 105]. Deuteration has been used to improve sequential assignments through C_α. In protonated samples, relaxation precludes the use of constant-time evolution in the carbon dimension. As a result, C_α resonances are broadened by the C_α-C_β scalar coupling. In deuterated samples, relaxation of the carbon nuclei is slower, allowing the recording of constant-time HNCA and HN(CO)CA experiments with greatly increased resolution [106, 107]. Deuteration has also been used to improve side chain assignments. In fully protonated samples, relaxation of side chain carbons can be fast enough to prevent observation of signals in spectra involving magnetization transfer along the aliphatic carbon chain to the backbone atoms. In partially deuterated samples, there is a tradeoff. There are fewer protons available to provide magnetization, but the loss of magnetization through carbon relaxation is much slower. In larger proteins, the benefit of slower relaxation often outweighs the loss of protons [108, 109].

1.4.3 RESIDUAL DIPOLAR COUPLINGS

When the orientation of a molecule in solution does not average to zero, structural information can be obtained from residual dipolar couplings between pairs of nuclei [110, 111, 112]. The required alignment of the molecule can be due to the molecule's own magnetic susceptibility anisotropy, or it can be augmented by an anisotropic medium. An anisotropic medium is required for most proteins, except for those with an unusually large susceptibility anisotropy. There are now many types of anisotropic media avail-

able [113]. Residual dipolar couplings can provide long-range orientational information in a way that other restraints often cannot; for example, residual dipolar couplings can define relative protein domain orientations when there are few NOE restraints between the domains [114]. In the opposite extreme, residual dipolar couplings can improve the local geometry of structural regions which yield poor NOE or torsion angle data [115]. When residual dipolar couplings are used in tandem with other types of restraints, there is often a synergistic effect, where the strengths of one type of restraint compensate for the shortcomings of another. For example, a small number of backbone residual dipolar couplings together with a small number of NOE restraints yielded a structure of the acyl carrier protein very similar to a structure determined by a large number of NOE's [116]. This type of synergism can also be seen in sequential assignments, where residual dipolar couplings can be used to resolve ambiguities [117].

1.5 SUMMARY

A unique system for the detoxification of inorganic and organic mercury has evolved in bacteria. This mercury resistance system has been a productive study area for several themes in biology, including metal-protein interactions, gene regulation, enzyme mechanisms, and direct transfer of metabolites. The mercury resistance system is also of practical interest due to the continuing problem of inorganic and organic mercury pollution, and the potential for the widespread use of the *mer*-encoded enzymes for mercury remediation. There are varying degrees of structural and mechanistic knowledge about the mercury resistance proteins. The structures of MerP, MerA, and MerR are well-characterized. Little is known about the structures of MerT and MerB, other than that they are a transmembrane protein and a globular cytosolic protein, respectively. The mechanism of operon regulation and DNA binding by MerR has been described in some detail. The mechanism of MerA is very well-described through a combination of muta-

genesis and electronic absorption spectroscopy involving the flavin moiety. The roles of the inner and carboxyl terminal cysteines are well-described, although there are still outstanding questions about the role of the amino terminal cysteines. Kinetic studies with MerB together with inorganic model systems which mimic MerB have elucidated much about how MerB cleaves the carbon-mercury bond. Kinetic and mutagenesis studies have also allowed some insight into the roles of protein and buffer thiols in the mechanism. However, relation of the mechanistic observations to specific protein residues of MerB is not as clear as the corresponding relationships in MerA due to the lack of structural information about MerB. Direct transfer of mercuric ions between proteins of the *mer* operon has important biological consequences, because it would minimize the exposure of the cell to toxic mercuric ion intermediates. Direct transfer has been proposed in several places in the mercury resistance system, but to date evidence for it only exists in the case of direct transfer from MerP to MerT.

The goals of the present study are two-fold. The first is to structurally characterize the MerB enzyme in a mercury-bound intermediate state. This structural knowledge will be useful in tying the many mechanistic observations about MerB to specific structural features. The second goal is to use a kinetic method to test the hypothesis that MerB can transfer its product, the mercuric ion, directly to MerA. Both of these studies will be of potential use to the ongoing efforts to utilize the MerB and MerA enzymes in a phytoremediation system.

CHAPTER 2

INITIAL DESCRIPTION OF THE MERB/HG/DTT COMPLEX

An initial characterization of a mercury-containing MerB complex was based only on backbone chemical shift assignments, EXAFS, and 2D ^{1}H-^{15}N HSQC NMR spectra. This initial characterization was sufficient to identify the composition of the complex as MerB/Hg/DTT, and to provide an estimate of the mercury binding site.

2.1 METHODS

2.1.1 MERB PURIFICATION

The *merB* gene from plasmid R831b [118] was amplified by PCR, and the *NdeI* / *XhoI* fragment was ligated into the expression vector pET21b (Novagen). The resulting plasmid was identical to pQZB1 [48] except for the insertion of a stop codon between the *XhoI* site and the MerB-encoding sequence. This construct prevented the expression of the histidine tag present in pET21b.

MerB protein was purified from BL21(DE3) cells containing the MerB-encoding plasmid. Unlabeled protein was produced by growing cells in Luria-Bertani (LB) broth at 37^{o}C for 24 hours. Uniform ($>$ 98%) ^{15}N-labeled MerB protein was produced by growing cells in modified minimal medium containing ^{15}N-labeled NH_4Cl as the sole nitrogen source. The growth medium contained 10 - 20 μM isopropyl D-thiogalactoside (IPTG) to continually induce MerB expression. ^{15}N/^{13}C-labeled MerB was prepared by growing cells in minimal medium containing ^{15}N-labeled NH_4Cl and ^{13}C-labeled glucose as the sole nitrogen and carbon sources, respectively. In LB broth, there was sufficient

expression without any induction by IPTG. All media contained 0.1 mg / mL ampicillin to retain the plasmid.

Purification was based on the scheme of Begley et. al. [53]. All steps were performed at 4^oC, and DTT-containing solutions were freshly prepared before use.

The cells from 3 liters of culture were harvested by centrifugation in a Beckman JA-10 rotor at 5000g for 20 minutes, and then suspended in 150 mL of buffer A (20 mM Tris (pH 8.0), 1 mM DTT, 1 mM EDTA) plus 1 mg / mL benzamidine. The suspension was passed through a French press and centrifuged at $100,000g$ for one hour. The supernatant was applied to a DEAE-sepharose Fast Flow (Amersham Biosciences) column (50 mm i.d. x 40 cm length) equilibrated with buffer A, and MerB was eluted with a salt gradient of 0-1 M NaCl over 1.5 L. MerB-containing fractions were identified by polyacrylamide gel electrophoresis, pooled, dialyzed with a 10K ultrafiltration membrane (Millipore) into buffer B (20 mM sodium phosphate (pH 7.2), 1 mM EDTA, 1 mM DTT), applied to a Q-sepharose Fast Flow (Amersham Biosciences) column (26 mm i.d. x 40 cm length) equilibrated with buffer B, and eluted with a 0-1 M NaCl gradient over 700 mL. The MerB-containing fractions were pooled. To prevent aggregation, the buffer of the pooled fractions was adjusted to a final concentration of 20 mM Tris (pH 8.0) and 100 mM NaCl. The pooled fractions were then concentrated to 10 mL and applied in 0.5 mL injections to a Superose-12 (Amersham Biosciences) gel filtration column equilibrated with buffer C (10 mM sodium phosphate (pH 7.5), 100 mM NaCl, 1 mM EDTA, and 1 mM DTT). MerB-containing fractions were stored at 4^oC in buffer C.

2.1.2 NMR Sample Preparation and Spectroscopy

Purified MerB protein samples were concentrated to 1 mM by centrifugation in a 10K cutoff Centricon ultrafiltration device (Millipore). Samples were exchanged into an NMR buffer by three cycles of dilution to 2.5 mL and reconcentration to 0.5 mL. The NMR

buffer consisted of 10 mM sodium phosphate (pH 7.5), 10 mM NaCl, 1 mM EDTA, 5-10 mM DTT, and 10% D_2O.

The MerB/Hg/DTT complex was prepared by adding at least one equivalent of an organomercurial substrate to an NMR sample of the free protein. The substrates used were: phenylmercuric acetate [62-38-4], mersalyl [492-18-2], ρ-hydroxymercuri benzoic acid (PHMBA), merbromin [129-16-8], and ρ-hydroxymercuri benzenesulfonic acid (PHMSA). Organomercurial substrates were all purchased from Sigma-Aldrich.

MerB/Hg/DTT samples with optically active l-DTT (2R, 3R - dithiothreitol) were prepared by diluting a MerB/Hg/DTT sample with l-DTT-containing buffer and reconcentrating, several times. MerB/Hg/DTE (dithioerythritol) samples were prepared in the same way. l-DTT and DTE were purchased from Sigma-Aldrich.

Gradient-enhanced ^{1}H-^{15}N HSQC spectra were collected on a 600 MHz Varian Inova spectrometer [119]. The NMR data were processed with NMRPipe/NMRDraw [120]. Contour plots were prepared with gri (http://gri.sourceforge.net/).

2.1.3 X-Ray Absorption Spectroscopy

A MerB/Hg/DTT sample was prepared by adding 1.5 equivalents of PHMSA in the presence of 5 mM fresh DTT. This sample was concentrated to 2 mM and a final volume of 0.5 mL in a 10K cutoff Centricon device (Millipore). This sample was then exchanged into 10 mM sodium phosphate (pH = 7.5), 20% v/v glycerol, by increasing the volume to 2.5 mL and reconcentrating three times. This procedure also separated unbound mercury, PHMSA, and DTT from the protein. The sample was loaded into a 24 x 3 x 2 mm polycarbonate cuvet (with one 24 x 3-mm wall consisting of 0.001-in Mylar tape), and immediately frozen in liquid nitrogen. X-ray absorption spectra were collected at the Stanford Synchrotron Radiation Laboratory (SSRL) on beamline 7-3 with the SPEAR ring operating at 3.0 GeV, 60-100 mA. Fluorescence excitation spectra were recorded with the sample at 10K using 1 mm vertically apertured beam incident on a Si[220]

double-crystal monochromator that was detuned to 50% maximum reflectivity for harmonic rejection. The averaged XAS data represent 8 scans, each of 21-minute duration. EXAFSPAK software (www-ssrl.slac.stanford.edu/exafspak.html) was used for data reduction and analysis, according to standard procedures [121]. The Fourier Transforms (FT's) of the extended X-ray absorption fine structure (EXAFS) spectra were generated using sulfur-based phase correction.

2.1.4 Anaerobic Sample Preparation

A series of experiments was designed with the goal of producing a MerB complex involving mercury, but not DTT. Due to the tendency of the cysteines of MerB to oxidize, measures were taken to protect MerB from oxygen. A 10 mL sample of free MerB and 20 mM DTT was placed in a sealed container. The air was then removed from the container by application of vacuum. After 20 minutes, the container was filled with argon at slightly higher than atmospheric pressure. This cycle was repeated three times. The sample was then transfered to a 10 mL injection loop in an anaerobic chamber to avoid exposure of the sample to air during the transfer process. The sample was injected onto a 200 mL gel filtration column composed of superdex-75 (Pharmacia). Prior to the procedure, the buffer running through the column was made anaerobic by cycles of vacuum and argon. The entire pathway for the column buffer, including the source buffer vessel, column, and collection vessel, constituted a sealed environment, filled with argon maintained at a pressure slightly higher than atmospheric. The collection vessel contained one equivalent of $HgCl_2$ and 1-20 equivalents of a small thiol such as cysteine or glutathione. Both protein and DTT in the column effluent were monitored by UV absorption; only protein-containing effluent was collected in the mercury-containing vessel.

The collected fraction was concentrated to $\sim$1 mM under an atmosphere of argon and sealed into an NMR tube with a rubber septum.

2.1.5 Sequential Assignment

A sequential assignment was performed using the HNCO [122, 123], HNCACB [122], (HB)CBCA(CO)NNH [122, 119, 98], and C(CC)TOCSY-NNH [124, 125, 126] experiments (see Table A.1 for acquisition parameters). WALTZ-16 decoupling was used to decouple ^{15}N and $^{1}H_N$ during acquisition [127].

2.2 Results and Discussion

2.2.1 Preparation of a mercury-containing MerB complex

In order to elucidate the structure and mechanism of MerB, the goal was to prepare a stable complex of MerB involving either an organomercurial substrate or a mercuric ion. It was seen that at pH 7.5 and in the presence of fresh DTT, free MerB adopts a single, well-folded conformation, as shown by the 2D ^{1}H-^{15}N HSQC spectrum (Figure 2.1A). For this reason, such a sample was used as a starting point for complex preparation.

2.2.2 Evidence for MerB/Hg/DTT

A mercury-containing MerB complex was prepared by adding the organomercurial substrate PHMBA to a sample of free MerB. The resulting 2D ^{1}H-^{15}N HSQC spectrum (Figure 2.1B) is very similar to the spectrum of the free form (Figure 2.1A), although there are small differences. This shows that the organomercurial substrate does bind the protein, yet the global fold remains the same. This procedure was repeated with a variety of organomercurial substrates (Figure 2.2), but the resulting spectrum was the same for all substrates. This result indicates that the organic portion is not present in the complex, because the different substrates with their quite different aromatic ring structures would be expected to change the chemical shifts of neighboring residues in different ways. This was confirmed by preparing a MerB/Hg/DTT complex using only free Hg(II) as a substrate; the resulting spectrum is the same as with organomercurial substrates.

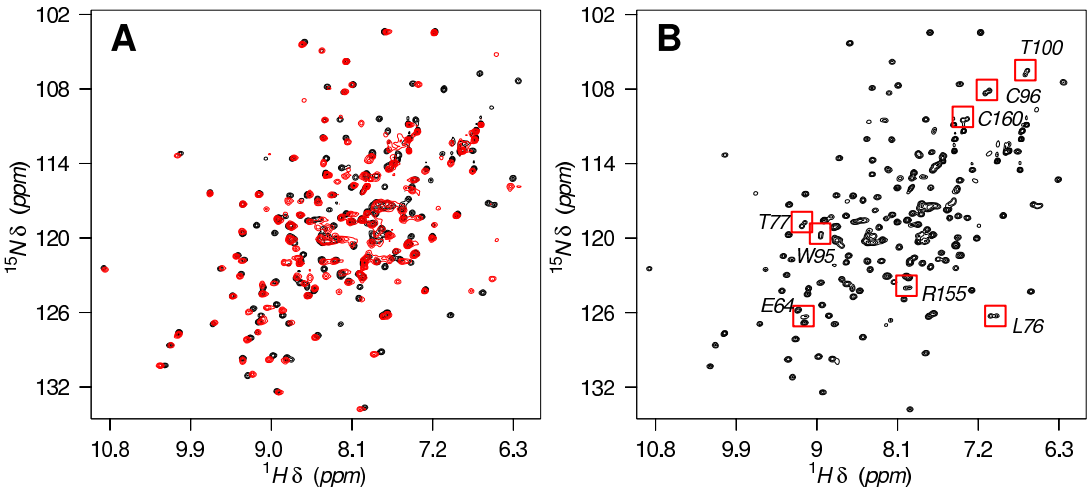

Figure 2.1: **A)** 2D ^{1}H-^{15}N HSQC spectra of free MerB (red) and MerB/Hg/DTT complex prepared with (l)-DTT (black). **B)** 2D ^{1}H-^{15}N HSQC spectrum of the MerB/Hg/DTT complex prepared with racemic DTT. Boxes indicate signals which appear as paired peaks in the presence of racemic DTT, but as single peaks in the presence of (l)-DTT.

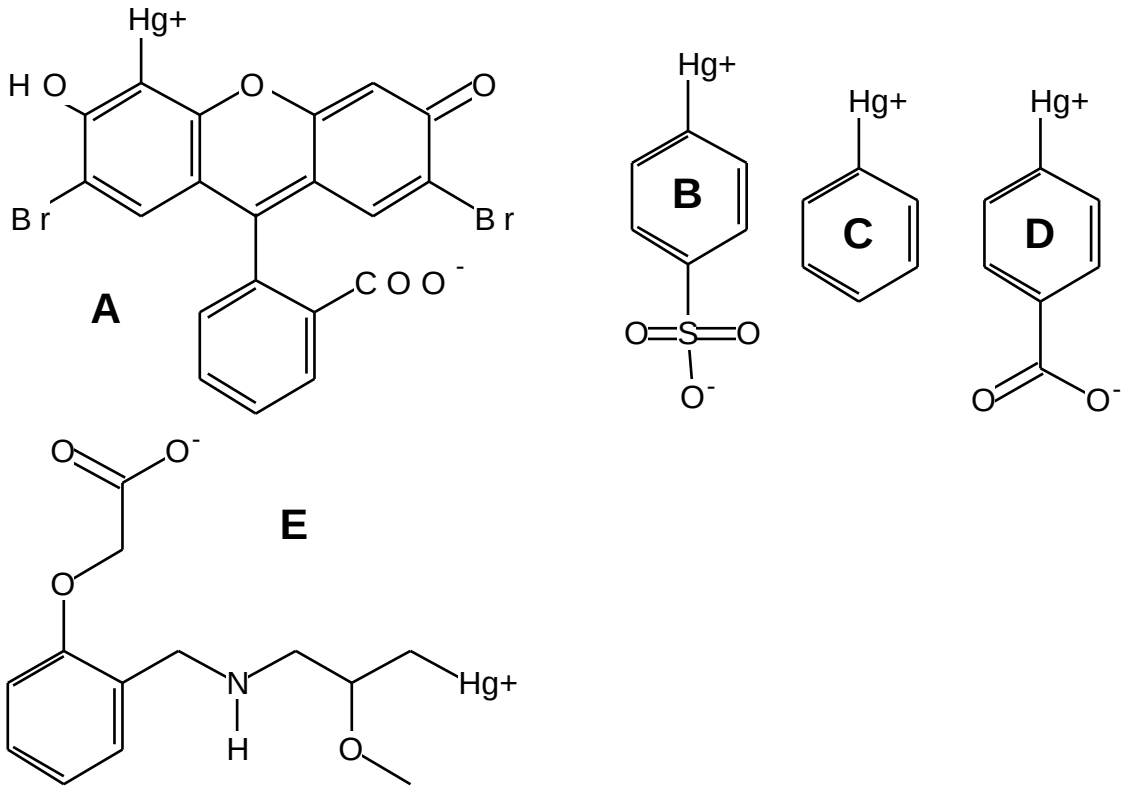

Figure 2.2: Organomercurial substrates used to prepare MerB/Hg/DTT complex: (A) merbromin, (B) PHMSA, (C) PMA, (D) PHMBA, and (E) mersalyl.

When complexes are prepared with substrate to protein ratios ranging from 1 to 2.5, the resulting spectrum is the same. This places an upper limit of 1 on the stoichiometry of mercury binding. Extensive buffer exchange or dilution and reconcentration of the complex in the absence of additional mercury or organomercurial does not change the spectrum. This suggests that the mercuric ion binds tightly, and places a lower limit of 1 on the stoichiometry of mercury binding.

Evidence that DTT is present in the complex also comes from the HSQC spectrum. One feature of the MerB/Hg/DTT spectrum not seen in the free protein spectrum is the presence of several closely spaced pairs of peaks (Figure 2.1B). When the complex is prepared with pure optically active (l)-DTT instead of a 50/50 racemic mixture of DTT, only one of each pair of peaks remains (Figure 2.3 A and B). The paired peaks belong to residues affected by the binding of DTT, and arise from the fact that MerB/Hg/(l)-DTT and MerB/Hg/(d)-DTT have slightly different spectra.

No such pairing of peaks occurs in the free protein spectrum in the presence of DTT (Figure 2.1A), which indicates that DTT does not associate with the free protein. Further, this implies that the association of the DTT molecule to the protein is mediated by the mercury atom. The DTT molecule could associate with the mercury atom either through only one of its sulfurs in a linear conformation, or through both of its sulfurs in a cyclic conformation. In order to distinguish between the cyclic and the linear binding modes, Analogous complexes were prepared with the *meso* compound dithioerythritol (DTE), which is not chiral, but is otherwise chemically equivalent to DTT. There are two possible linear MerB/Hg/DTE complexes, but only one possible cyclic MerB/Hg/DTE complex if there is free rotation about Hg-S bonds (Figure 2.4). Because the two linear forms are diastereomers, they would have different NMR spectra, and the MerB/Hg/DTE spectrum would exhibit paired peaks similar to those seen in the presence of a racemic mixture of DTT. The pairing of peaks does not occur in the MerB/Hg/DTE spectrum (Figure

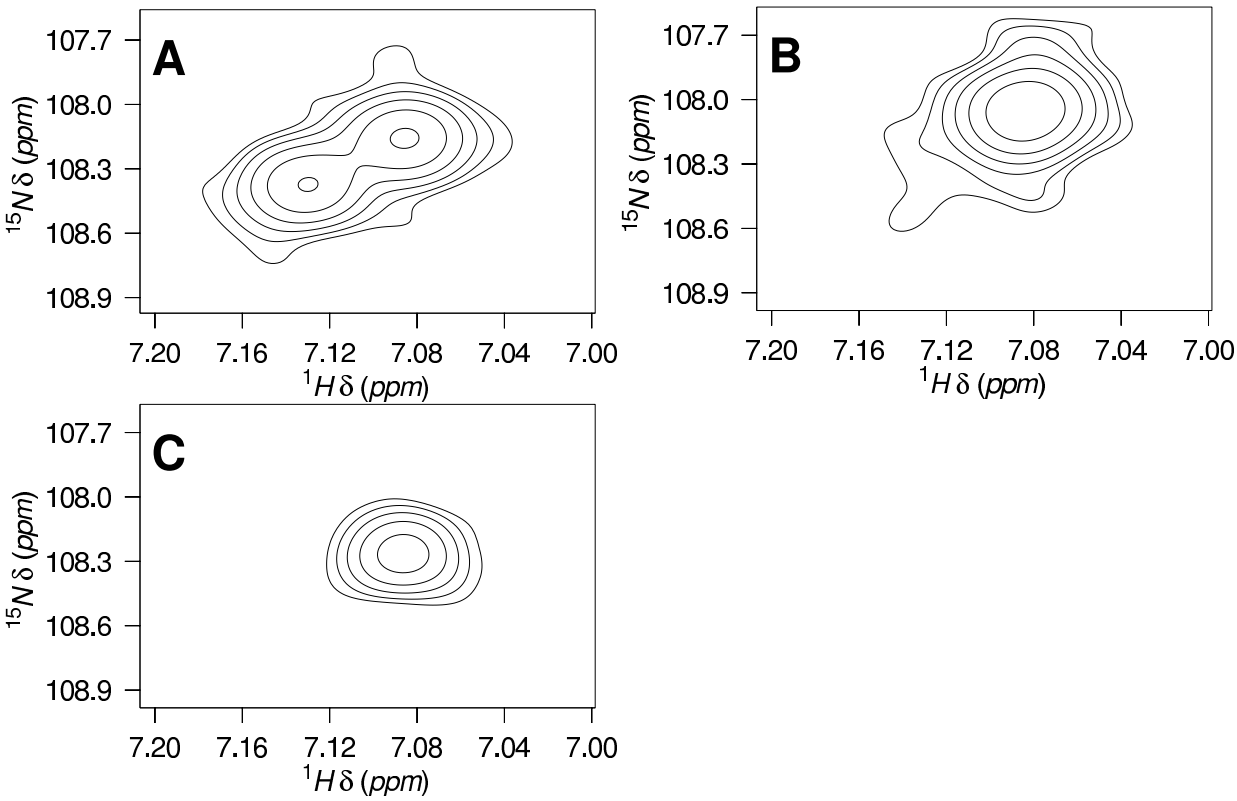

Figure 2.3: Evidence for MerB/Hg/DTT complex. Highlighted region of 2D ^{1}H-^{15}N HSQC spectra (Figure 2.1B) of ^{15}N-labeled MerB/Hg/DTT complex at 27^{o}C when it is prepared with **A)** racemic DTT, **B)** (l)-DTT, or **C)** DTE. The highlighted region corresponds to residue C96.

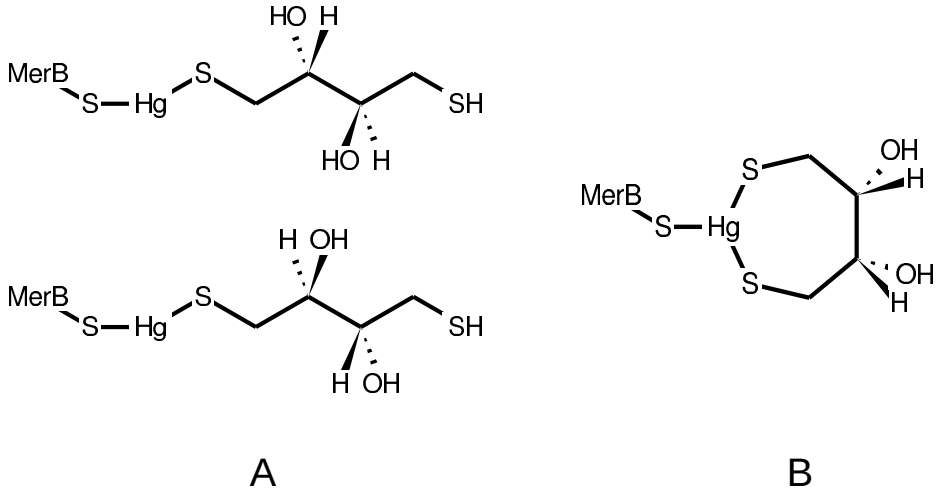

Figure 2.4: Two possible binding modes of DTE in the MerB/Hg/DTE complex. **A)** In the linear mode, two complexes are possible, leading to two distinct spectra. **B)** In the cyclic mode, only one complex is possible if there is free rotation about the Hg-S bond, leading to a single spectrum.

2.3C). The observation of only a single peak with DTE is only consistent with a cyclic conformation, bound to the mercury through both sulfur atoms (Figure 2.4B).

2.2.3 EXAFS STUDIES OF MERB/HG/DTT COMPLEX

In order to determine the geometry of ligands associated with the Hg(II), EXAFS data were collected on the MerB/Hg/DTT complex. The EXAFS data of the MerB/Hg/DTT complex are most consistent with a coordination sphere for mercury consisting of three sulfur atoms (Table 2.1 and Figure 2.5). Although models with 2, 3, or 4 sulfurs all can provide good fits to the data, the Debye-Waller value (σ^2_{as}) for the HgS_3 case is the most physically reasonable one. The Hg-S bond distances (2.42 $\pm$ 0.02 Å) also coincide with other mononuclear, mercuric-thiolate compounds that have a coordination number of three [128].

Table 2.1: Curve fitting results for Hg EXAFS[a]

Sample filename (k range) $k^3\chi$	Fit	Shell	R_{as} (Å)	σ^2_{as} (Å)	ΔE_0 (eV)	f'[b]
MerB/Hg/DTT	1	Hg-S	2.42	-0.0010	-3.93	0.103
HBDTA (2-12 Å^{-1})	2	Hg-S_2	2.42	0.0025	-1.91	0.091
$k^3\chi$ = 10.74	3	Hg-S_3	2.43	0.0051	-0.73	0.092
	4	Hg-S_4	2.43	0.0074	-0.02	0.099

[a] Shell is the chemical unit defined for the multiple scattering calculation. Subscripts denote the number of scatterers per metal. R_{as} is the metal-scatterer distance. σ^2_{as} is a mean square deviation in R_{as}. ΔE_0 is the shift in E_0 for the theoretical scattering functions.
[b] f' is a normalized error (chi-squared):

$$f' = \frac{\left\{ \sum_i \left[k^3 \left(\chi_i^{obs} - \chi_i^{calc} \right) \right]^2 / N \right\}^{1/2}}{\left[\left(k^3 \chi^{obs} \right)_{max} - \left(k^3 \chi^{obs} \right)_{min} \right]}$$

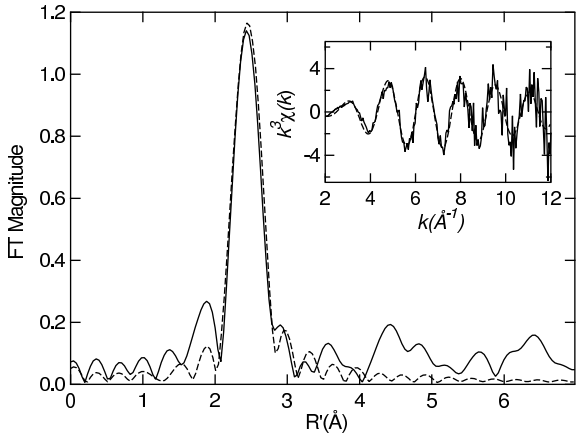

Figure 2.5: Fourier transforms of the Hg L_3 EXAFS of MerB/Hg/DTT(solid) and theoretical best fit (dashed) corresponding to a coordination shell of HgS_3 using the parameters of Fit 3, Table 2.1. The k^3-weighted EXAFS (solid) and theoretical best fit (dashed) are displayed as inset.

2.2.4 NMR Spectroscopy of Other MerB/Hg/thiol Complexes

In the presence of oxygen and the absence of DTT, MerB oxidizes rapidly and becomes misfolded or aggregated. Such samples have little or no chemical shift dispersion in ^{1}H-^{15}N HSQC spectra (data not shown). The result is the same if a small monothiol such as cysteine or glutathione replaces DTT; at the high concentrations required for NMR, these compounds are not competent at protecting MerB from oxygen. The high stability of the MerB/Hg/DTT complex ensures that any mercury-containing MerB sample prepared in the presence of DTT will consist of entirely MerB/Hg/DTT. It would be instructive to obtain a structurally characterizable MerB sample containing mercury and a more physiological thiol such as cysteine or glutathione. For this reason, a protocol was developed to produce MerB/Hg complexes in the absence of both DTT and oxygen (see methods).

The anaerobic protocol began with a mixture of DTT and MerB to ensure that the protein began in a reduced state. The gel filtration column step in the anaerobic protocol served to separate the protein from DTT in the absence of oxygen, while minimizing the time between separation of protein and DTT and exposure of protein to mercury. The total time that the protein was exposed to neither DTT nor mercury was no longer than the elution time of the column, which was approximately 30 minutes.

The ^{1}H-^{15}N HSQC spectra of the resulting complex indicated that in fact the anaerobic procedure protected MerB from oxidation (Figure 2.6). The chemical shift dispersion was nearly as good as in the MerB/Hg/DTT complex. The equivalent experiment performed under aerobic conditions gave a complex with nearly no chemical shift dispersion (not shown). However, the reproducibility of the MerB/Hg/cys complex was not as good as that of the MerB/Hg/DTT complex (see Figure 2.6). From the sequential assignment of the MerB/Hg/DTT complex (see below), peaks in the MerB/Hg/cys HSQC spectrum could be tentatively assigned by proximity to MerB/Hg/DTT peaks. The assignments revealed that the least reproducible (and often missing) peaks in the MerB/Hg/cys spectrum correspond

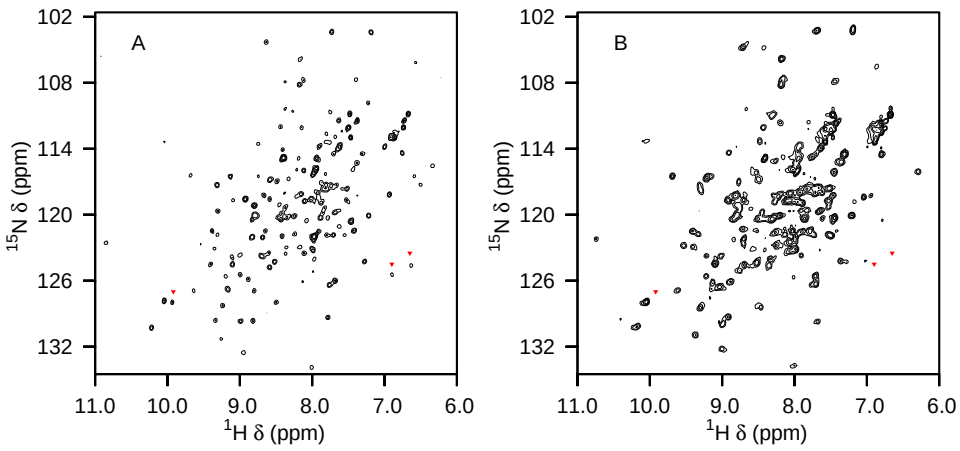

Figure 2.6: ^{1}H-^{15}N HSQC spectra of two representative MerB/Hg/cys complexes prepared by anaerobic gel filtration. Arrows mark several peaks present in (A) which are absent in (B).

to residues near the active site. For this reason, further structural studies were not pursued with the MerB/Hg/cys complex. The results were similar with a MerB/Hg/glutathione complex.

2.2.5 Sequential Backbone Assignment

Due to the consistent quality and stability of the MerB/Hg/DTT complex, this complex was selected for further structural analysis. Sequential backbone assignments were performed on a ^{15}N/^{13}C-labeled MerB/Hg/DTT sample.

The peaks in the HNCO experiment were very intense and well-resolved. It was used to define amide proton and nitrogren chemical shifts for a number of (unassigned) H-HN moieties. $C_{\alpha,i-1}$ and $C_{\beta,i-1}$ peaks were then assigned to these moieties from the (HB)CBCA(CO)NNH experiment. $C_{\alpha,i}$ and $C_{\beta,i}$ peaks were assigned to each moiety from the HNCACB experiment. Moieties were placed in sequential order by matching

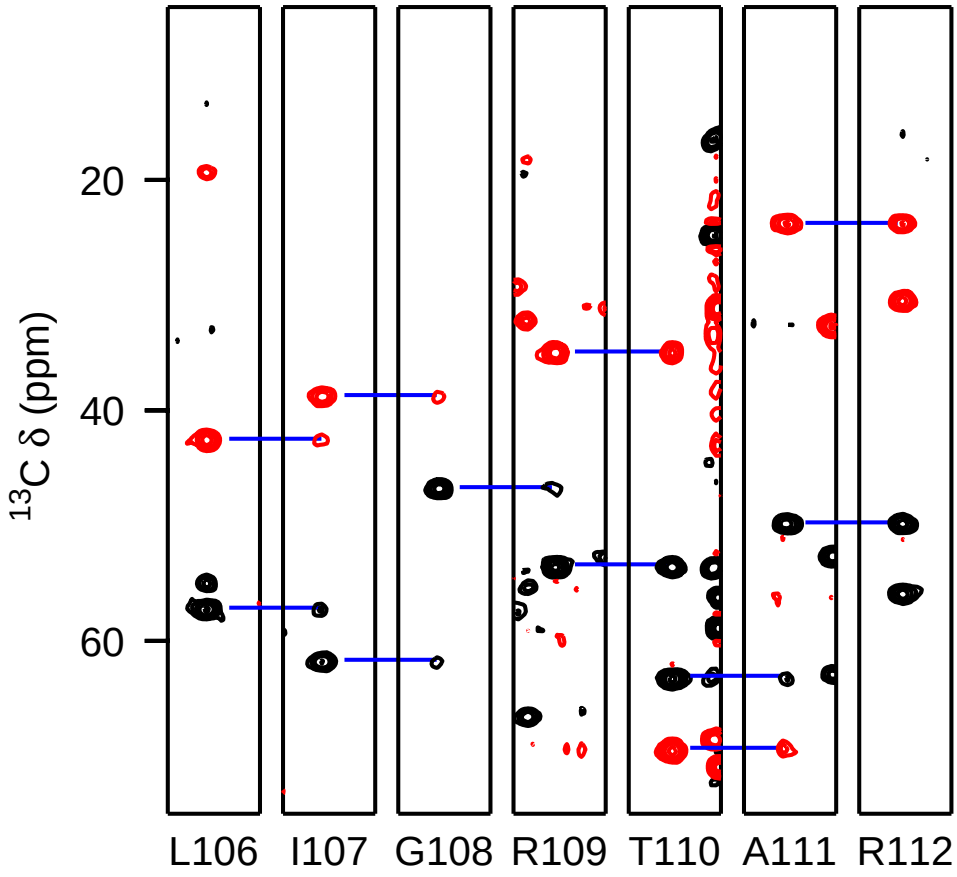

Figure 2.7: Sequential backbone assignment of the MerB/Hg/DTT complex using the HNCACB experiment. Strips are taken at the ^{1}H and ^{15}N frequencies of the amide atoms of the residues shown. Horizontal lines indicate connectivity between C_i and C_{i-1} peaks.

the chemical shifts of the C_α and C_β peaks. A representative stretch of sequential backbone assignments in the HNCACB experiment for residues 106 - 112 is shown in Figure 2.7. The C(CC)TOCSY-NNH experiment allowed each moiety to be grouped into a set of probable amino acid types based on aliphatic ^{13}C chemical shift. This aided assignment of sequential connections ambiguous in C_α / C_β chemical shift and helped map assigned moieties to the protein sequence.

Table 2.2: Residues which exhibit paired peaks in the ^{1}H-^{15}N HSQC spectrum in the MerB/Hg/DTT complex prepared with racemic DTT.

E64	L76
T77	W95
C96	T100
R155	C160

For the first 25 residues of the sequence, a few weak amide signals could be tentatively assigned. None of these assignments were used in structural calculations. The lack of observable amide signals for the first 25 residues was probably due to rapid amide proton exchange at pH 7.5 and/or line broadening caused by rapid conformational exchange. For residues 26-212, 166 of 177 (HN_i, N_i, C_{i-1}) moieties were assigned by the procedure described above.

The backbone chemical shifts of free MerB and the MerB/Hg/DTT complex are very similar (Figure 2.8). The largest differences occur in two regions, one centered around C96 and the other centered around C159/C160. Also, several residues near C96 not assigned in the free form were assigned in the complex. Residues near C117 do not display large chemical shift differences, which suggests that the mercuric ion is not bound to C117.

The sequential assignment also allowed the residues which display paired peaks in the presence of racemic DTT to be mapped to the sequence (Table 2.2). Eight paired peaks have been assigned to the residues E64, L76, T77, W95, C96, T100, R155, and C160. The regions displaying paired peaks correlate roughly with the regions displaying the largest chemical shift differences between the free and bound forms.

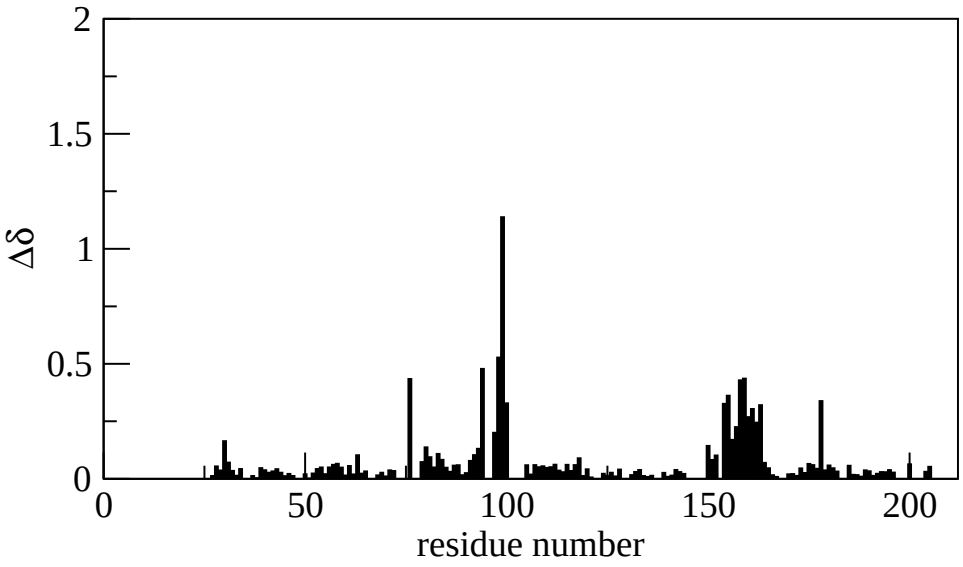

Figure 2.8: Comparison of backbone chemical shifts between free MerB and the MerB/Hg/DTT complex. The quantity $\Delta\delta$ is a weighted average of chemical shift differences for amide proton, amide nitrogen, and carbonyl atoms:

$$\Delta\delta = (0.17(\delta N_{free} - \delta N_{complex})^2 + 0.39(\delta C_{free} - \delta C_{complex})^2 + (\delta H_{free} - \delta H_{complex})^2)^{1/2}$$

where the weighting coefficients reflect the relative chemical shift dispersion of each type of nucleus [129].

2.2.6 CYSTEINE C_β CHEMICAL SHIFT

The C_β chemical shifts of the cysteine residues provide evidence that C96 is the only cysteine involved in mercury binding in the MerB/Hg/DTT complex. This cysteine residue has been shown to be critical for MerB catalysis [48]. In the free protein, C117, C159, and C160 all display standard C_β chemical shifts for reduced cysteines, and the chemical shift of C96 C_β was not assigned. In the MerB/Hg/DTT complex, the C_β shifts of C117, C159, and C160 are also in the normal reduced range, but for C96 the C_β shift (37.9ppm) is unusually downfield (Table 2.3). The downfield C_β shift of C96 could be explained by formation of a disulfide bond involving this residue [130], but it is unlikely that such a disulfide bond is present given the absence of available thiol groups. Indeed, no free thiol is available in the buffer, there is no evidence that other cysteines in the MerB monomer form a disulfide bond, and there is no evidence from the NMR spectra that the MerB/Hg/DTT complex forms a dimer. The more likely explanation for the chemical shift of C96 C_β is coordination to the mercuric ion. Cysteine C_β chemical shifts are sensitive to mercuric ion binding at the thiolate group. In solution NMR studies of $Hg(SR)_n$ complexes, C_β generally shifts downfield as the number of thiol ligands *n* increases [131]. The observed chemical shift of C96 C_β in the MerB/Hg/DTT complex is consistent with a population of essentially 100% HgS_3. The C_β chemical shift of C159 is slightly downfield from the standard range for reduced cysteine (Table 2.3), but much less so than that of C96. This observation allows the possibility of a small degree of exchange between C96 and C159. In the calculated structure of the MerB/Hg/DTT complex (to be described in chapter 4,) the distance between the sulfur atoms of C159 and C96 is 9 Å, which is close enough to allow some exchange without excessive conformational shifts.

Table 2.3: C_β chemical shift (ppm) for cysteine residues in MerB/Hg/DTT complex.

Residue	δC_β (ppm)
C96	37.9
C117	29.7
C159	32.8
C160	26.7

2.3 SUMMARY

Simple addition of an organomercurial substrate to MerB in the presence of DTT results in a very stable, reproducible MerB/Hg/DTT complex. The evidence for this complex consists of a pattern of paired resonances in the ^{1}H-^{15}N HSQC spectrum (Figure 2.1) which is only consistent with a single DTT molecule bound to the mercury atom through both of its sulfur atoms. EXAFS studies of the MerB/Hg/DTT complex indicate that mercury is coordinated by three sulfur atoms. The C_β chemical shifts of cysteine residues in the MerB/Hg/DTT complex indicate that the mercury atom is bound to C96. Taken together, the data are consistent with a model for the MerB/Hg/DTT complex in which the mercuric ion is bound by both sulfur atoms from DTT and the sulfur atom of C96. The backbone chemical shifts of free MerB and the MerB/Hg/DTT complex are very similar, showing that the two forms have the same overall fold. The largest differences are clustered around C96 and C159/C160, the probable binding site for mercury.

CHAPTER 3

DIRECT TRANSFER FROM MERB TO MERA[1]

It has been suggested that product release from MerB occurs via a direct-transfer mechanism, in which the mercuric ion passes directly from the active site of MerB to the active site of MerA without first diffusing through the cytoplasm [40]. This mechanism would prevent the release of the toxic mercuric ion product of MerB into the cytoplasm. The type of mechanism in which a metabolite passes directly between enzymes is known as substrate channeling, and is an alternative to a dissociative mechanism (see Figure 1.3). The occurrence of substrate channeling has been proposed for many other enzyme pairs [69, 70].

A variety of kinetic methods have been developed to test for substrate channeling. The approach we use here is the enzyme-buffering test [72], in which the activity of E2 is measured in the presence of X and an excess of E1 (using the notation from Figure 1.3). An expected activity is calculated assuming that only the dissociative mechanism is operating. If the observed activity is higher than expected, then the assumption must be wrong, and the most plausible alternative explanation is the channeling mechanism. There are three components to this test. The first is a measurement of the dissociation constant of the E1-X complex (MerB/Hg/DTT in this case). The second is a measurement of the kinetic parameters (K_M and v_{max}) of E2 with free X substrate, which in this case correspond to MerA and Hg(II). The third component is the measurement of MerA activity with the MerB/Hg/DTT complex as a substrate.

[1]Reproduced in part with permission from Biochemistry, submitted for publication. Unpublished work copyright 2004 American Chemical Society.

The choice of assay conditions is important for the enzyme buffering test. In this study, assays were performed in the presence of 1 mM cysteine because this reflects the physiological situation, and because all reported multiple-turnover studies of MerA to date require the presence of cysteine or another single-sulfhydryl small molecule. The MerB/Hg/DTT complex was chosen as a substrate because of its excellent stability, homogeneity, and reproducibility.

3.1 METHODS

3.1.1 MERA PURIFICATION

The Tn21 MerA gene was obtained in the form of plasmid pNS2 [36] from Dr. Richard Meagher at the University of Georgia. Plasmid pGB5 was created by ligating the Xba I / Hind III fragment of pNS2 into expression vector pET-21b (Novagen) cut with the same two restriction enzymes. *E. coli* BL21-DE3 cells were transformed with pGB5 and grown at 37^{o}C in Luria-Bertani broth with 0.1 mg / mL ampicillin. Upon reaching an O.D. of 1.0, the cultures were induced with 0.4 mM IPTG, and incubated for another 2-3 hours before harvesting. Purification was based on the procedure of Rinderle et al. [59] with modifications. The cells from 6 liters of culture were harvested by centrifugation in a Beckman JA-10 rotor at 5000 g for 20 minutes, suspended in 200 mL of buffer A (20 mM Tris (pH 8.0), 1 mM EDTA, 1 mM DTT) plus 1 mg / mL benzamidine, then lysed by passage through a French press. The lysate was cleared by centrifugation at 100,000g and applied to a DEAE-sepharose Fast Flow (Amersham Biosciences) column (50 mm i.d. x 40 cm length) equilibrated with buffer A, and MerA was eluted with a salt gradient of 0-1 M NaCl over 1.5 L. MerA-containing fractions were identified by the kinetic assay described below. Active fractions were pooled and dialyzed with a 10K-cutoff membrane into buffer B (20 mM sodium phosphate (pH 7.2), 1 mM EDTA, 1 mM DTT), then applied to a Blue Sepharose Fast Flow (Amersham Biosciences) column (1.5 in. i.d.; 3 in. length)

equilibrated with buffer B, and eluted with a 0-1 M NaCl gradient over 700 mL. Active fractions were concentrated to 10 mL and separated on a 200 mL Superdex-75 gel filtration column equilibrated with buffer D (10 mM sodium phosphate (pH 7.3), 1 mM EDTA, 1 mM DTT, and 100 mM NaCl). MerA-containing fractions were reconcentrated to 5 mL, reduced with additional DTT, and then applied in 0.5 mL batches to a disposable PD-10 sephadex G25 desalting column (Amersham Biosciences) equilibrated with a storage buffer consisting of 50 mM sodium phosphate (pH 7.0), 100 mM NaCl, and 30% glycerol. The column eluent was immediately divided into 0.5 mL aliquots and stored at -80^{o}C.

3.1.2 KINETIC ASSAYS

MerA activity was followed by monitoring the consumption of NADPH:

$$N(t) = [NADPH]_o - [NADPH] \tag{3.1}$$

where N(t) is the total reaction progress. NADPH concentration was measured by UV absorbance (A_{340}=6.22 $mM^{-1}cm^{-1}$). Reaction mixtures contained 50 mM sodium phosphate (pH 7.0), 100 mM NaCl, 100 μM NADPH, 1 mM cysteine, and varied concentrations (0 - 10 μM) of Hg(II) or MerB/Hg/DTT substrate. Assays were performed at room temperature. Reactions were initiated by adding 20 μL of a MerA aliquot to 1 mL of reaction mixture. The mixtures were well mixed before recording began. Each MerA aliquot was thawed immediately before use. One aliquot was used for a series of 10 experiments plus 2-3 control experiments. The control experiments contained 4 μM Hg(II) as a substrate.

MerB/Hg/DTT samples for use as MerA substrates in kinetic assays were prepared by adding 1.5 equivalents of PHMSA to a sample of purified MerB in the presence of fresh DTT. In order to remove excess mercury, organomercurial, and DTT from the buffer, the complex was purified by injecting 5-8 mL on a sephadex G-25 gel filtration column with a void volume of 12 mL. A 10 mL fraction after the void volume was

collected as the protein-containing fraction. Because residual DTT, mercury, or PHMSA in the MerB/Hg/DTT sample could potentially interfere with the assay results, we indirectly determined the degree of separation between protein and small molecules by using riboflavin as a tracer. Because riboflavin has a strong visible absorbance at ∼450 nm, its concentration in the MerB-containing fraction was easily measured. By this measure, the degree of separation between riboflavin and protein was at least 1:1000. Other small molecules such as unbound mercury, organomercurials, and DTT should behave in a similar way.

A stock of free MerB free of contaminating NADPH oxidase activity was prepared for use in enzyme buffering tests. A 10 mL sample of free MerB was dialyzed into 20 mM sodium phosphate pH 7.4, 1 mM EDTA, and 1 mM DTT, and then applied to a Blue Sepharose Fast Flow (Amersham Biosciences) column (1.5 in. i.d.; 3 in. length) equilibrated with the same buffer. MerB was collected from the flow-through of this column. No significant NADPH oxidase activity was detected in this MerB stock. Aliquots were freshly reduced and separated from DTT before use in kinetic assays by the following procedure. DTT was added to a final concentration of 4 mM to an 0.5 mL aliquot of 0.5 mM free MerB. The aliquot was then injected onto a PD-10 desalting column, and 1.5 mL of MerB-containing eluent was collected for use in enzyme buffering tests. The free MerB stock was used within four hours of preparation and kept on ice until use in the assays.

3.1.3 Analysis of kinetic data

As noted in several other multiple-turnover studies of MerA activity, the reaction proceeds with a rapid initial velocity which decays to a slower, constant final velocity. The change in velocity cannot be ascribed simply to substrate depletion or product buildup, because it can happen before substrate concentrations change significantly. The change can be explained by conversion of enzyme between a more active and a less active form, the rate of conversion being dependent on thiol and substrate conditions. The reaction velocity

will then follow an exponential course [59]:

$$v = v_f + (v_o - v_f)e^{-kt} \tag{3.2}$$

where v_f is the final steady state velocity, v_o is the initial rapid velocity, and k is the net rate of conversion between the two MerA forms. The total reaction progress (which is the quantity measured in MerA assays) is obtained by integrating equation (3.2) to obtain:

$$N(t) = \int_0^t v(t) = v_f t - \frac{v_o - v_f}{k} e^{-kt} + \frac{v_o - v_f}{k} \tag{3.3}$$

All measured reaction curves were fit to equation (3.3) by adjusting the parameters v_f, v_o, and k. The normalized, relative activity v_o^{rel} is defined as the ratio of v_o for that assay to the average v_o for the control experiments (4 μM Hg(II)) in that assay series. This ensures that any differences in MerA activity between aliquots does not affect the comparison of measurements taken using different aliquots.

3.1.4 Calculation of K_D

The stability of the MerB/Hg/DTT complex was measured by dialysis against a cysteine-containing buffer. 1 mL of $\sim$1 mM MerB/Hg/DTT was dialyzed into one liter of buffer, and the appearance of free MerB was monitored by NMR. Prior to dialysis, all unbound DTT was removed from the MerB/Hg/DTT sample by several rinses and reconcentrations with DTT-free buffer. Dialysis was performed in a disposable, 2 mL, 10K-cutoff device (Spectrum Laboratories). The concentrations of free protein, bound protein, and free mercury are controlled by the dissociation constant K_D:

$$\begin{aligned} K_D &= \frac{[merB] \times [Hg/DTT]}{[MerB/Hg/DTT]} \\ &= \frac{f^2}{(1-f)} \frac{v_i}{v_o} [MerB/Hg/DTT]_o \end{aligned} \tag{3.4}$$

where f is the fraction of MerB/Hg/DTT that has dissociated, v_i is the volume containing protein, v_o is the volume of the dialysis buffer, and $[merB/Hg/DTT]_o$ is the initial concentration of MerB/Hg/DTT being dialyzed. The fraction f can be measured by NMR because free MerB and MerB/Hg/DTT have distinct ^{1}H-^{15}N HSQC spectra. Dialysis was allowed to proceed for 24 hours before NMR measurements were made. When none of the free form was observed in a spectrum, the parameter f was set to a lower bound of 15%. This number is based on the minimum reversion to the free form that would be clearly visible in the spectrum given its signal-to-noise ratio.

3.2 Results

3.2.1 Measurement of K_M and v_{max}

All kinetic traces were fit to equation 3.3 as described in the methods. The quality of fit was determined from the sum of squared residuals between the data and the predicted values from equation 3.3. For all experiments used in the kinetic analysis, the RMSD between the observed and expected values was below 0.05 μM (i.e. $\chi_n^2 < 1$ for a 0.05 μM error in NADPH concentration measurement.) A typical fit with an RMSD value of 0.03 μM is shown in Figure 3.1.

In the first series of assays, the kinetic parameters of MerA with a mercuric chloride substrate were measured. All assays contained 1 mM cysteine, and a series of mercuric chloride substrate concentrations from 0 - 4 μM was used. The results are shown in Figure 3.2. The activity was fit to a Michaelis-Menten model with parameters K_M=1.0 μM, v_{max}^{rel}=1.2. v_{max}^{rel} is in the unitless scale described in the methods (i.e. the activity at 4 μM Hg(II) is 1.0 by definition).

Although it is the relative velocity, and not the absolute velocity, that is needed for the enzyme buffering tests, we also measured the absolute velocity for the purpose of comparison with other studies. A MerA concentration of 0.7 μM was measured in one aliquot by

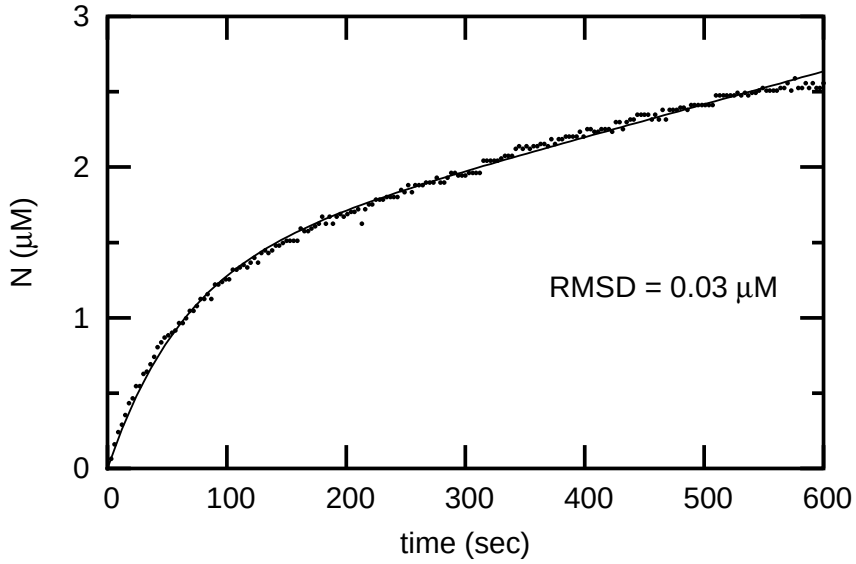

Figure 3.1: Typical progress curve for MerA assay. Reaction contained 1 mM cysteine and 9.3 μM MerB/Hg/DTT complex as a substrate, plus standard components described in the methods. The fitted line corresponds to equation 3.3 with the parameters v_o= 23.3 $nM{\cdot}sec^{-1}$, v_f= 2.1 $nM{\cdot}sec^{-1}$, k = 0.015 sec^{-1}. The RMSD between the observed N(t) and the calculated N(t) for this particular curve is 0.03 μM.

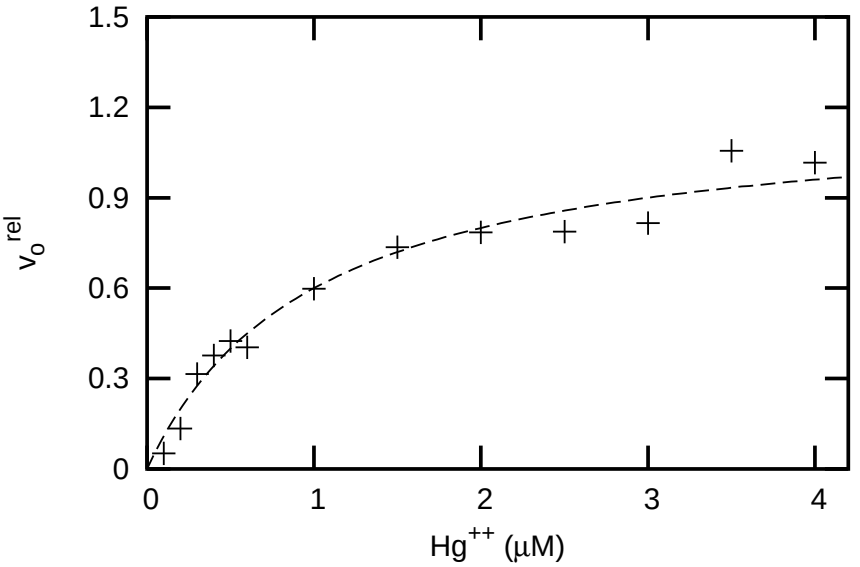

Figure 3.2: Measurement of MerA kinetic properties with Hg(II) substrate. The initial velocity was determined using equation 3.3 and normalized to a control experiment as described in the methods. Assays contained 1 mM cysteine. The fitted line corresponds to K_M=1.0 μM, v_{max}=1.2. v_{max} is a unitless ratio as described in the methods.

Table 3.1: Summary of K_D measurements by NMR. f is defined as in equation 3.4.

thiol	f	K_D
none	$< 15\%$	$< 26nM$
1 mM cysteine	$< 15\%$	$< 26nM$
10 mM cysteine	65%	1.6 μM

absorbance at 455 nm due to the flavin cofactor, using a value of $\varepsilon_{455} = 11.3 mM^{-1} \cdot cm^{-1}$ [59]. Because the aliquots were diluted by a factor of 50 in the assays, the final concentration of MerA in the assays was 14 nM. The average value of v_o in the control experiments with 4 μM Hg(II) was 24 $nM \cdot sec^{-1}$. The value of v_{max}^{rel} was 1.2 (see Figure 3.2), so the absolute value of v_{max} is 28.8 $nM \cdot sec^{-1}$. Dividing by the MerA concentration gives a specific activity of 123 min^{-1} for our MerA preparation.

3.2.2 Measurement of K_D

The stability of the MerB/Hg/DTT complex measured under several thiol conditions is reported in Table 3.1. Dissociation of the complex was detectable only at high (10 mM) cysteine concentration. At 0 - 1 mM cysteine concentration, an upper bound of K_D=26 nM was found.

3.2.3 MerA Assays with MerB/Hg/DTT substrate

In the second set of assays, the reaction mixtures contained an initial concentration of 9.3 μM MerB/Hg/DTT and 1 mM cysteine. Various amounts of excess free MerB were also added to the assay mixtures. For each assay, an expected free mercury concentration $[Hg(II)]_{calc}$ was calculated on the basis of equation 3.4 and the value for K_D in Table 3.1. Note that "free" Hg(II) in this sense means Hg(II) not bound to protein, although it is bound to whatever small thiol is present. The expected MerA velocity was then calculated

Table 3.2: Enzyme-buffering test results with the MerB/Hg/DTT complex and MerA[a].

free MerB (μM)	Hg(II)$_{calc}$ (μM)	v^{rel}_{calc}	v^{rel}_{obs}	v^{rel}_{obs} / v^{rel}_{calc}
0	0.47	0.38	0.69	1.82
0.9	0.21	0.20	0.43	2.15
1.8	0.12	0.13	0.37	2.87
2.7	0.08	0.09	0.46	5.11
3.6	0.06	0.07	0.62	8.86
4.5	0.05	0.05	0.27	5.40
5.4	0.04	0.05	0.45	9.00
9.1	0.02	0.03	0.28	9.33

[a] All assays contained 9.3 μM MerB/Hg/DTT plus varied amounts of free excess MerB (0-9.1 μM). Hg(II)$_{calc}$ was determined from the K_D reported for 1 mM cysteine in Table 3.1. v^{rel}_{calc} was determined as described in the text. v^{rel}_{obs} is the measured MerA velocity (reported as a unitless ratio as described in the Methods).

based on [Hg(II)]$_{calc}$. For all concentrations of free MerB used, the observed velocity was higher than what is expected from a purely dissociative mechanism, sometimes by a factor of as high as 9 (Table 3.2).

3.3 Discussion

The results of the enzyme buffering test (Table 3.2) are inconsistent with an entirely dissociative mechanism of mercuric ion transfer from MerB to MerA. The most reasonable alternative mechanism is substrate channeling. In general, the higher the ratio of v_{obs} to v_{calc}, the stronger the conclusion of substrate channeling. The ratios reported in this study are similar to the ratios ($\sim$ 10) reported for NADH channeling in the NADH:ubiquinone complex I [82], which are among the highest reported using the enzyme buffering test. The conclusion of substrate channeling depends on accurate measurement of kinetic parame-

ters. It is therefore useful to discuss measures taken to ensure accuracy of those measurements.

3.3.1 Controls for Artifacts

The enzyme-buffering method is subject to several known artifacts relating to enzyme impurity and errors in kinetic parameter estimation. A prerequisite for the enzyme-buffering test is knowledge of the behavior of E2 using free X as a substrate. This is needed in order to calculate the expected activity. This information can be taken from the literature, but it is better to redetermine the kinetic parameters in the same laboratory where the enzyme-buffering experiments are done. This is because many factors may influence the activity of E2, such as: the purity of the preparation, the exact gene sequence, the storage conditions, the temperature of the assays, and the buffer conditions. However, if the control and enzyme buffering experiments are performed in the same laboratory, these factors will influence the control and the enzyme-buffering experiments equally, and so will not affect the final conclusion of experiments done in tandem.

It is also important that the model for E2 activity corresponds to the conditions and range of X concentrations likely to be encountered in the enzyme buffering test. Over an Hg(II) concentration range of 0-4 μM, we measured a specific v_{max} of 123 min^{-1} and a K_M of 1.0 μM (Figure 3.2). This concentration range corresponds to the free Hg(II) expected in the enzyme buffering test (Table 3.2). Because MerA is a dimeric enzyme with a fairly complicated mechanism [60, 59], this simple Michaelis-Menten model cannot be expected to accurately describe the behavior of MerA outside of this concentration range. This is probably the most important reason why the present measurement of the absolute v_{max} (123 min^{-1}) is lower than the absolute v_{max} (1044 min^{-1}) measured in the realm of 100 μM mercuric ion substrate [59]. Another measurement placed v_{max} of MerA at 340 min^{-1} [30], which may be higher than our measurement largely due to the higher temperature used in that study (37^{o}C vs. 21^{o}C). The laboratory-specific factors mentioned

above also certainly contribute to the differences observed between this measurement of the MerA kinetic parameters and previous measurements. The differences also illustrate the necessity of performing independent measurements of E2 kinetic parameters when doing enzyme buffering experiments.

There are also issues relating to E1 (MerB) impurity [132]. If the E1 preparation is impure, i.e. the true E1 concentration is lower than what is reported, then the calculated free X concentration (second column in Table 3.2) will be artificially low. This in turn leads to an underestimation of v_{calc}, which can lead to a false conclusion of substrate channeling. This potential problem is mitigated in our study by the way in which the E1/X (MerB/Hg/DTT) complex is prepared. The MerB/Hg/DTT complex used in enzyme buffering experiments was thoroughly separated from excess mercury and thiols by gel filtration. The only way a mercuric ion can make it to the enzyme buffering assay is as part of a MerB/Hg/DTT complex. This ensures that the E1/X ratio is at least 1:1. The addition of excess free MerB increases the ratio above 1:1. Even if the MerB preparation used were only 50% pure, the final results would not be greatly altered. Still, it should be noted that our MerB preparations appeared at least 95% pure on a Coomassie Blue-stained gel, and this pure band represents a protein population which adopts a single conformation, as judged by NMR spectroscopy.

Error in the measurement of the dissociation constant for the E1/X complex can also potentially lead to false conclusions in the enzyme buffering test. Because v_{calc} increases with increasing K_D, an underestimation of K_D can lead to a false conclusion of channeling. For this reason, steps were taken to prevent underestimation of K_D. The generous lower limit of 15% used for the extent of dissociation f in equation 3.4 means that the reported K_D of 26 nM is probably not an underestimate. Table 3.1 shows the results of the K_D measurements under several thiol conditions. The condition with 1 mM cysteine is the most important for this study, because that is the condition used in the enzyme buffering tests. No dissociation was detected in the presence of zero to 1 mM cysteine, leading to an

upper bound of 26 nM for the apparent K_D (Table 3.1). The measurement of an apparent K_D of 1.6 μM in the presence of 10 mM cysteine indicates that the dialysis method is capable of showing dissociation and that, at sufficiently high concentration, cysteine is capable of removing mercury from the MerB/Hg/DTT complex. The high stability seen at low cysteine concentration is consistent with the observation that the MerB/Hg/DTT complex always remained intact through cycles of dilution and reconcentration even in the absence of Hg(II) or DTT. Changes in the volume v_i of the dialysis tube during dialysis can be shown not to affect the final K_D estimate. Because the total amount of MerB present in the system remains constant, the quantity $[\text{MerB/Hg/DTT}]_0 v_i$ in equation 3.4 is constant; i.e. a change in v_i due to change of buffer volume during dialysis is exactly counteracted by an opposite change in dialysate concentration.

Another potential source of error in enzyme buffering tests is contaminating "E2-like" catalytic activity in the E1 preparation. A relatively large concentration (several μM) of E1 is used, whereas only a catalytic amount (nM) of E2 is used. Because of this, even minor contaminants in E1 that have enzymatic activity similar to E2 can cause problems. An E1 contaminant that produces false E2 activity will raise the observed activity, but not the expected activity, and can therefore lead to a false conclusion of channeling [133]. Fortunately this problem is easily detected by control assays in which E2 is omitted. In this study no significant MerA-like activity was detected in the absence of MerA.

3.3.2 Initial Rate Approximation

The derivation of equation 3.3 does not take into account the fact that substrate and product concentrations are changing during the course of the reaction. However, analysis of kinetic data and the enzyme buffering test were based entirely on consideration of initial reaction rates. So, the conclusions depend mainly on the ability of equation 3.3 to accurately describe the initial part of the reaction. For the initial part of the curve, the assumption that substrate concentrations are not very different from their initial values is valid. For

example, in Figure 3.1, it is apparent that the intial reaction rate is well-established when less than 10% of the substrate has been consumed. Equation 3.3 may indeed be a poor model for the reaction at longer times ($>$ 2 minutes) at low substrate concentrations. However, the RMSD measure and examination of the curves showed that equation 3.3 provided a good fit to the initial reaction velocity at all concentrations.

3.3.3 Other tests for channeling

Recently Geck and Kirsch [87] have developed a new test for substrate channeling based on inactivated forms of the E1 enzyme. This test also avoids some of the potential problems associated with the need for large amounts of E1 in the enzyme buffering test. Also, the Geck-Kirsch method can disprove the channeling hypothesis, whereas the enzyme buffering test can only disprove the dissociative mechanism, and is inconclusive in cases where channeling does not occur. The Geck-Kirsch method requires a variant of E1 that is unable to complete its reaction, but interacts with E2 in the same way normal E1 does (assuming such interaction occurs at all). It may be difficult to meet both of these conditions simultaneously in the case of the MerA-MerB pair, because the proposed interaction (Figure 3.3) occurs through the mercuric ion itself. There are several catalytically impaired variants of MerB available [48], but it is not clear if they bind mercury in the same way, or could be expected to interact with MerA in the same way, as wild-type MerB.

3.3.4 The MerA-MerB interaction

The initial characterization of the MerB/Hg/DTT complex (Chapter 2) allows several observations about product release from MerB. The first observation is that monothiol compounds such as cysteine or glutathione compete very poorly with dithiol compounds for the mercuric ion bound to MerB; this is shown by the dissociation experiments and

is consistent with previous observations on the inhibitory role of DTT. The second observation is that MerB can accommodate an exogeneous dithiol molecule in its active site, with the mercuric ion bound by both exogeneous sulfur atoms as well as C96 of MerB. The third observation is that although exogeneous monothiols cannot displace the bound dithiol easily, exogeneous dithiols can. For example, DTE easily displaces bound DTT.

Based on these results, it appears that mercury release from MerB *in vivo* would be efficiently accomplished by a protein containing two or more sulfhydryls located in close proximity to each other. Interestingly, all MerA proteins contain two adjacent cysteine residues at the extreme carboxyl-terminal of the protein and these two cysteine residues have been shown to be essential for normal catalytic turnover. Further, these cysteines have been shown to be involved in removing tightly bound thiol ligands from mercuric ions before they pass to the MerA active site [62]. Because MerB can be thought of as a very large, tightly-bound thiol ligand, it is a reasonable hypothesis that the carboxyl terminal cysteines of MerA serve the same function in the MerA-MerB interaction. In analogy to the MerB/Hg/DTT complex, the mercuric ion in the MerA/Hg/MerB complex would be coordinated by C96 of MerB and both carboxyl terminal cysteines of MerA (Figure 3.3). This type of mechanism may be a common theme throughout bacterial mercury detoxification; for example, the MerT membrane mercury transporter contains two cysteines on its periplasmic face which are implicated in direct transfer from MerP, and two cysteines on its cytosolic face which may be involved in direct transfer of mercury to MerA [11].

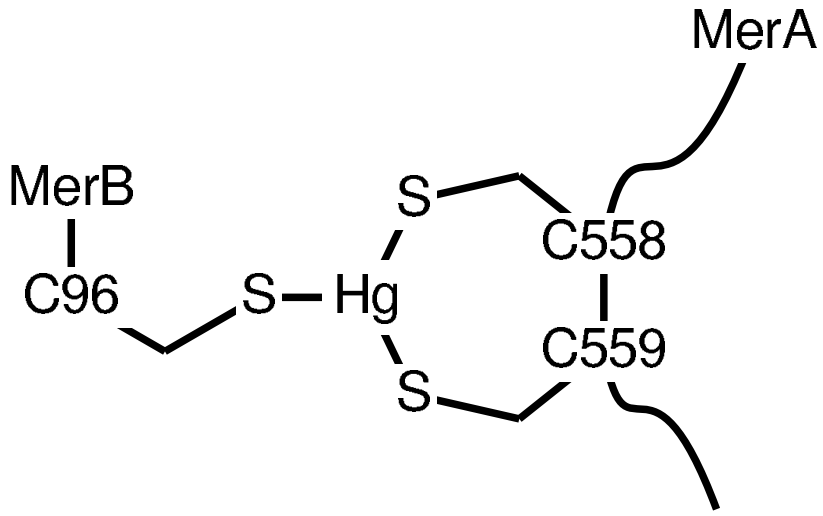

Figure 3.3: Proposed intermediate in the MerA-MerB interaction. The carboxyl terminal cysteines of MerA are involved in removing the mercuric ion from the MerB active site, and form a trigonal intermediate similar to the MerB/Hg/DTT complex.

CHAPTER 4

NMR STRUCTURE OF THE MERB/HG/DTT COMPLEX

The structure of the MerB/Hg/DTT complex was solved using heteronuclear triple-resonance NMR experiments (see Table A.1). Shortly before the structure determination of the MerB/Hg/DTT complex, the structure of the free MerB protein was also determined by NMR [134].

4.1 METHODS

4.1.1 SAMPLE PREPARATION IN D_2O

The HCCH-COSY, HCCH-TOCSY, (^{1}H-^{13}C)CT-HSQC, and 3D ^{13}C-edited HMQC-NOESY experiments were performed on a ^{13}C/^{15}N-labeled MerB/Hg/DTT sample dissolved in D_2O. NMR buffer in D_2O was prepared from standard NMR buffer in H_2O by several cycles of lyophilization and resuspension in D_2O. A ^{13}C/^{15}N-labeled MerB/Hg/DTT sample was exchanged into the deuterated NMR buffer by six cycles of 5:1 dilution and reconcentration, which yields a theoretical minimum remaining H_2O fraction of $\sim$1/15,000, or $\sim$3 mM H_2O. The remaining water signal in the spectra recorded in D_2O was consistent with this level of exchange.

4.1.2 EXPERIMENTS FOR SIDE-CHAIN RESONANCE ASSIGNMENTS

Aliphatic side-chain atom assignments were derived from the HCCH-COSY [135], HCCH-TOCSY [136], 3D HCCTOCSY-NNH and (H)C(CC)TOCSY-NNH [124, 125, 126] experiments in combination with the sequential backbone assignments which have

been described in chapter 2. The 3D HCCTOCSY-NNH experiment correlates side-chain aliphatic proton resonances in F_1 to backbone ^{15}N and H_N in F_2 and F_3, respectively. Magnetization from the aliphatic side-chain proton is transferred through the scalar coupling to its attached ^{13}C atom, then to C_α via isotropic mixing, then to C' through the scalar coupling, and then to ^{15}N and ^{1}H. The (H)C(CC)TOCSY-NNH experiment is similar, except ^{13}C chemical shifts are detected in F_1. In the HCCH-COSY experiment, magnetization from aliphatic side-chain protons (F_1) is transferred to the attached ^{13}C (F_2), to an adjacent ^{13}C through the scalar coupling, and then to an attached proton vicinal to the first (F_3). In the HCCH-TOCSY experiment, isotropic mixing is used for the carbon-carbon transfer, such that all protons in the same spin system will be correlated in F_1 and F_3, rather than just vicinal protons.

The HCCH-COSY and HCCH-TOCSY experiments employed a constant-time evolution period in the F_2 (^{13}C) dimension [137]. Therefore, mirror-image linear prediction was used to double the number of time domain complex points from 40 to 80 in both experiments [138, 139]. Linear prediction was also useful for improving the resolution in the F_1 (^{1}H) dimension, because the acquisition time in this dimension was sufficiently short (17 msec) that many signals were truncated. Forwards-backwards linear prediction [139], rather than mirror-image linear prediction, was employed because signals decay in t_1 with different rate constants. The performance of linear prediction generally degrades as the number of frequency components (i.e. peaks) in the predicted dimension increases, and the method fails entirely if the number of frequency components exceeds the number of data points [140]. Therefore, a protocol was used in which a time-domain dimension was extended by linear prediction only when all other dimensions were in the frequency domain. The data were first Fourier transformed in t_3 and t_1, then extended by linear prediction and transformed in t_2. An inverse transformation on t_1 was then performed, making this the only time-domain dimension. The data in t_1 were extended by linear prediction and then re-transformed, yielding a final spectrum processed with linear prediction

in both F_1 and F_2. The improvement achieved in F_1 by linear prediction in two dimensions is shown in Figure 4.1.

Peaks in the HCCH-COSY experiment were correlated to peaks in the H(CC)TOCSY-NNH experiment via the H1 and H2 (F_1 and F_3, respectively) chemical shifts, and to peaks in the (H)C(CC)TOCSY-NNH experiment via the ^{13}C (F_2) chemical shift. Although the chemical shifts of side-chain atoms were available from the H(CC)-TOCSY-NNH and C(CC)-TOCSY-NNH experiments, the assignments were taken from the HCCH-COSY and HCCH-TOCSY experiments in all cases because of the superior resolution for both ^{13}C and ^{1}H in those experiments. The ^{13}C resolution is better in the HCCH-COSY and HCCH-TOCSY experiments due to the constant-time evolution period in F_2, which eliminates broadening due to C-C scalar couplings. The ^{1}H resolution is better because in the HCCH-COSY and HCCH-TOCSY experiments, the side-chain ^{1}H chemical shift is measured in the directly detected dimension, whereas in the H(CC)-TOCSY-NNH experiment the side-chain ^{1}H chemical shift is measured in the F_1 dimension.

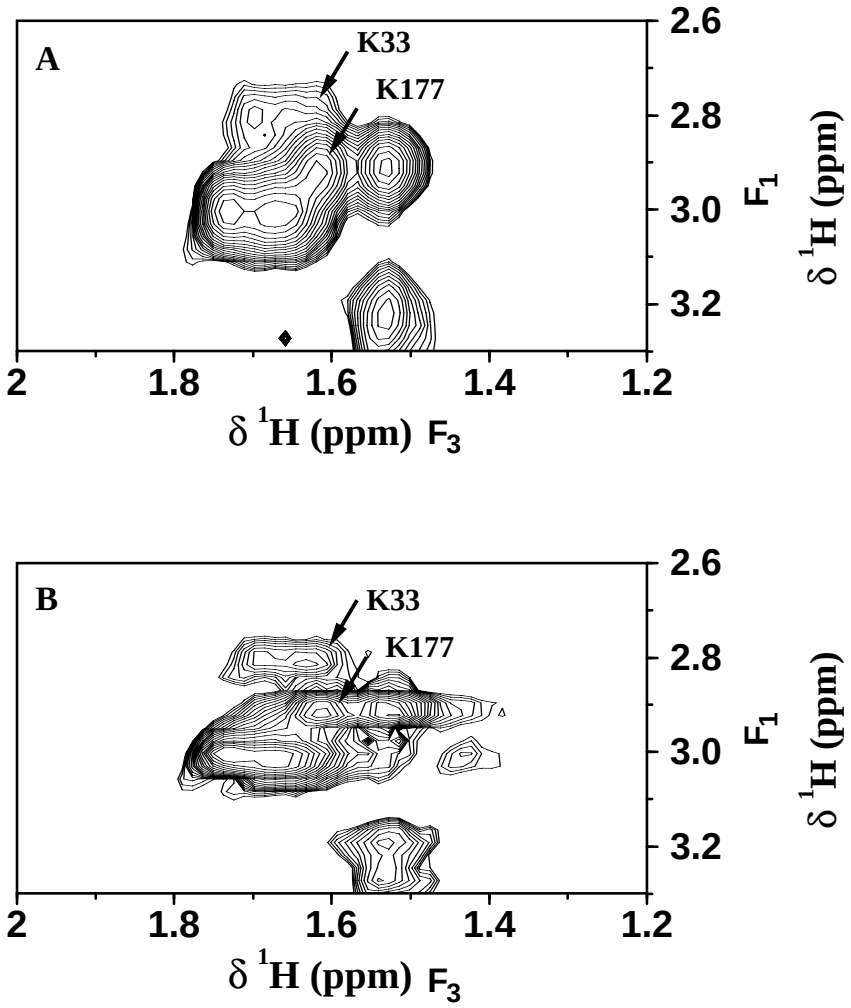

Figure 4.1: F_1-F_3 slices of an HCCH-COSY spectrum of MerB/Hg/DTT processed without (A) and with (B) linear prediction in t_1. Both versions were processed with linear prediction in t_2, as described in the text. The F_2 chemical shift is 42.15ppm. This region is crowded by peaks from several lysine residues at the frequencies (H_ε, C_ε, and H_δ) in (F_1, F_2, and F_3), respectively. Two such peaks are marked in the figure from K33 and K177. The peak from K33, in particular, is better resolved with linear prediction employed in t_1.

4.1.3 NOE Assignments

In order to obtain structural information in the form of interproton distance restraints, ^{15}N-edited NOESY-HSQC [141] spectra were collected with 40 msec and 100 msec mixing times, and a 3D ^{13}C-edited HMQC-NOESY [142] spectrum was collected with a 100 msec mixing time. NOE restraints were classified into three distance categories based on intensity: strong (1.8-2.8 Å), medium (1.8-3.4 Å), and weak (1.8-5.0 Å). The calibration of intensity vs. distance class was based on a consideration of NOE crosspeaks corresponding to known distances: intraresidue H_α and H_β, and H_α-H_N (i, i+3) and H_α-H_β (i, i+3) in helical regions.

4.1.4 Residual Dipolar Coupling Measurement

Residual dipolar couplings were obtained using Pf1 phage (from ASLA) as an alignment medium [143]. Each experiment was recorded on one aligned sample containing phage and one control sample not containing phage. The phage concentration in the aligned sample was 11 mg / mL, which yielded a ^{2}H quadrupolar splitting of 10.5 Hz. Samples contained 1.3 mM ^{13}C/^{15}N-labeled MerB/Hg/DTT in 90% H_2O, 10% D_2O, 10 mM sodium phosphate pH 7.5, 1 mM EDTA, and 10 mM NaCl. One-bond couplings were measured with a series of TROSY-HNCO-based 3D triple-resonance NMR experiments [144]. These experiments are capable of providing three types of residual dipolar coupling measured in heteronuclear dimensions (D_{N,H_N}, $D_{N,C'}$, and D_{C',C_α}), and two types of residual dipolar coupling measured in the directly detected dimension ($D_{H_N,C'}$ and D_{H_N,C_α}). The D_{C',C_α} dipolar coupling was taken as the difference in splitting between a spectrum recorded under aligned conditions and a spectrum recorded under isotropic conditions. Due to the negative sign of $^1J_{N,C'}$ and $^1J_{N,H_N}$, $D_{N,C'}$ and D_{N,H_N} were taken as the difference in splitting between the spectrum recorded under isotropic conditions and the spectrum recorded under aligned conditions. For structure calculations, residual dipolar

coupling restraints were included as harmonic potentials between the calculated and measured couplings [115]. The harmonic force constants at the beginning of the slow-cooling simulated annealing cycle were set to 0.01 kcal·mol^{-1}·Hz^{-2}, and were ramped up to final values of 1.0 kcal·mol^{-1}·Hz^{-2}, 3.0 kcal·mol^{-1}·Hz^{-2}, and 5.0 kcal·mol^{-1}·Hz^{-2} for D_{N,H_N}, D_{C',C_α}, and $D_{N,C'}$, respectively.

4.1.5 Dihedral Angle Restraints

Backbone ψ and ϕ dihedral angle restraints were obtained by a database search of sequence and chemical shift homology using the program TALOS [145]. H_α, N, C', C_α, and C_β chemical shifts were used for the TALOS prediction. The errors in ϕ and ψ were set to either a minimum of 15^o or to $\pm 1.5\sigma$, where σ is the standard deviation of the predicted angles from the database search.

4.1.6 Backbone ^{15}N Relaxation Data

^{15}N T_1 and T_2 relaxation rates and ^{15}N-^{1}H steady-state heteronuclear NOE values were measured using gradient-enhanced 2D spectra described by Farrow *et. al.* [146]. T_1 and T_2 decay rates were sampled with 11 and 9 points, respectively, and fit to single-exponential decays. Heteronuclear ^{15}N-^{1}H NOE values were measured as the ratio of peak intensities in the presence and absence of ^{1}H saturation before each scan.

4.1.7 Intermolecular NOE

NOE transfers between the DTT molecule and the protein in the MerB/Hg/DTT complex were measured with an F_1-(^{13}C)filtered, F_3-(^{13}C)edited NOESY-HSQC experiment [147] on a ^{13}C/^{15}N-labeled MerB/Hg/DTT sample in D_2O. The experiment utilized WURST purging pulses to remove magnetization originating on protons bound to ^{13}C prior to NOE transfer. The GARP sequence was used to decouple ^{13}C and ^{1}H during acquisition

[148]. Because the protein component was nearly completely ^{13}C enriched and the DTT molecule was at natural abundance, all observed crosspeaks were from DTT atoms to protein atoms. The chemical shifts of the DTT atoms in the MerB/Hg/DTT complex were measured with a 1D ^{13}C-filtered WATERGATE spectrum [149].

4.1.8 Partially Deuterated MerB/Hg/DTT Complex

A sample of 99%^{13}C, 99% ^{15}N, and ~70% ^{2}H - enriched MerB was prepared in a similar fashion to the $^{13}C/^{15}N$-labeled sample, except that the growth medium contained 70% D_2O. Prior to inoculation into large-scale deuterated minimal medium, cells were adapted to D_2O in several stages in small ($\sim$ 20 mL) cultures. Cells from an initial culture during the exponential growth phase in fully protonated medium were isolated by centrifugation and resuspended in a medium containing 70% D_2O. The cells were then again allowed to grow into the exponential phase, then harvested by centrifugation. This cycle was repeated once more, and the final growth was used to innoculate a liter-scale culture. This procedure was necessary because initial growth in D_2O is slow. The centrifugation / resuspension cycles prevent the accumulation of β-lactamase in the growth medium during the long period of D_2O adaptation, which can lead to loss of the MerB-expressing plasmid. The partially (70%) deuterated MerB/Hg/DTT sample was prepared as described for the non-deuterated version in Section 2.1.2.

The partially deuterated sample was used to obtain sequential correlations of C_α atoms through the HNCA-D and HN(CO)CA-D experiments [106, 107]. The sample was also used to obtain correlations of backbone amide (N, HN) moieties and side-chain protons through a H(CC-CO)NH-TOCSY experiment [109]. C_β resonances were detected with HN(CA)CB-D and HN(CACO)CB-D experiments on the partially deuterated sample [107], but these experiments did not yield any assignments that were not also obtainable from the fully protonated sample. Experiments on the partially deuterated sample utilized deuterium decoupling to minimize broadening of the ^{13}C resonances [106, 150, 151].

4.1.9 Structural Calculations of Individual Domains

The initial structure calculation of the MerB/Hg/DTT complex was performed separately on three segments of the protein. This was done for two reasons: to speed the initial calculations, and to allow an independent domain-by-domain analysis of the alignment tensor. The domains were chosen by an examination of the free MerB structure. The similarity of the backbone chemical shifts of free MerB and the MerB/Hg/DTT complex indicate that the two forms have a very similar secondary structure. Therefore, it was assumed that domain divisions valid in the free structure would also be valid in the unknown MerB/Hg/DTT structure. This assumption was found to be valid when the MerB/Hg/DTT structure was solved. The division into domains was based on a number of qualitative criteria: there should be no secondary structure elements shared between the two domains, there should be no backbone-backbone hydrogen bonds between them, and it should be possible to define a reasonably flat surface between the two domains that intersects the protein backbone only once. Using these criteria, the MerB structure was divided into an amino terminal domain consisting of residues 21-79, a central domain consisting of residues 80-137, and a carboxyl terminal domain consisting of residues 138-212 (see Figure 4.2). The first 20 residues do not give any observable NMR signals and so were not included in any of the structure calculations.

Structures of each domain were calculated by simulated annealing implemented in the program CNS [153, 96]. Calculations began from an extended strand and utilized a slow-cooling torsion angle dynamics stage followed by a Cartesian dynamics stage [154]. Structure calculations made use of NOE-derived interproton distance restraints, backbone ψ and ϕ angle restraints, and the three classes of residual dipolar coupling restraints described above (D_{N-HN}, $D_{C'-C_\alpha}$, and $D_{N-C'}$). Due to the inclusion of residual dipolar coupling restraints, cooling phases during simulated annealing were longer and had smaller time steps than what is normally employed in the absence of residual dipolar

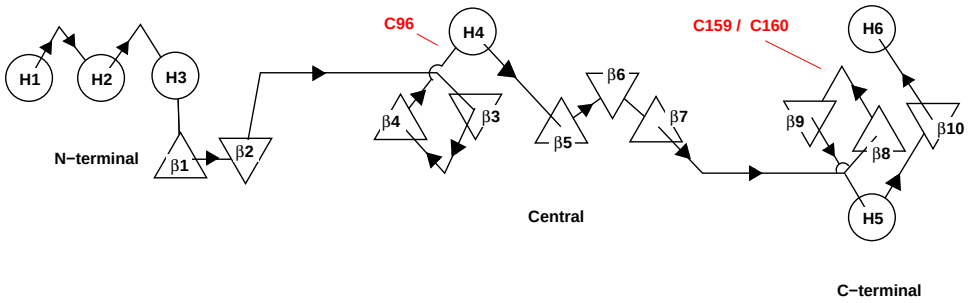

Figure 4.2: Secondary structure topology of MerB showing the three domains: the amino terminal α-helical domain, the central β sheet domain, and the carboxyl terminal domain. The diagram is in the notation of Sternberg and Thornton [152], in which an upwards triangle △ represents a β strand viewed from the amino terminus, and a downwards triangle ▽ represents a β strand viewed from the carboxyl terminus. Circles represent α helices. The lengths of the connecting segments are not proportional to the actual length of the connecting loops in the structure; they are drawn to emphasize the distinction between the domains. The locations of the three cysteine residues involved in the active site are shown.

coupling restraints [155]. For each domain, a population of 70 structures was calculated. For each domain, at least 50 of these had no dihedral angle violations greater than 5^o and no NOE distance violations greater than 0.5 Å. The 20 lowest energy structures were selected for further analysis.

The structural information contained in residual dipolar couplings was represented in simulated annealing calculations by the inclusion of four imaginary “anisotropy atoms” which exist only to define the orientation of the alignment tensor [115]. The group of anisotropy atoms consists of an origin atom and one atom for each of the Cartesian dimensions. The distances and angles between the atoms are fixed. The orientation of the tensor, together with the known magnitudes of the tensor’s components, are used to calculate expected residual dipolar couplings. An anisotropy energy is calculated based on a harmonic potential of the predicted vs. measured residual dipolar coupling for each vector. Two ways of using the anisotropy atoms are possible. If a pre-folded starting structure is available, this starting structure can be put in the principal alignment frame along with the

anisotropy atoms. The orientation of the anisotropy atoms is then fixed during simulated annealing. Alternately, if a pre-folded structure is not used or if the principal alignment frame is not known, the anisotropy atoms can be allowed to rotate freely. The latter method requires knowledge of the magnitude, but not the orientation, of the alignment tensor; the orientation is determined during the calculation through minimization of the anisotropy energy. Free rotation of the anisotropy atoms was employed in all structure calculations.

For each domain, the structure and alignment tensor magnitudes were determined together in an iterative cycle of simulated annealing and alignment tensor determination. For the first round of simulated annealing, residual dipolar coupling restraints were not included. The resulting structure was used to obtain a first estimate of the alignment tensor principal components (S_{XX}, S_{YY}, and S_{ZZ}) by singular value decomposition (SVD) [156]. The resulting alignment tensor was then used to include residual dipolar coupling restraints in a second round of simulated annealing. This process was repeated until the derived principal alignment tensor components did not change between successive cycles. In all cases, convergence happened by the third iteration.

4.1.10 Structure Calculation of the Full Protein

After the structure of each domain had been solved separately, the structure of the full-length polypeptide chain (excluding the unstructured region of the first 20 amino acids) was solved as a single unit. This calculation included several interdomain NOE restraints between the amino terminal and central domains, and several interdomain NOE restraints between the central and carboxyl terminal domains. There were no NOE restraints detected between the amino terminal and carboxyl terminal domains. A single orientation of the alignment tensor was used for the entire molecule. However, separate values of the principal component magnitudes (which had been determined in the individual domain calculations) were retained for each domain.

The full-length structure calculations also included a model of the Hg-DTT group bound to C96. The Hg-S bond lengths for both the C96-Hg bond and the DTT-Hg bonds were set to 2.4 Å, which is consistent with the EXAFS results (see Section 2.2.3). Intermolecular NOE restraints between protons of the DTT molecule and the protein were set to an upper bound of 5 Å, and a lower bound of 1.8 Å.

Simulated annealing calculations on the overall MerB/Hg/DTT structure began from an extended chain conformation with standard geometry and employed a slow-cooling torsion angle dynamics phase, followed by a second slow-cooling Cartesian dynamics phase [154]. A total of 50 structures with no NOE violation greater than 0.5 Å and no backbone dihedral angle restraint violation greater than 5 degrees were calculated. From this set, the 20 lowest-energy structures were selected for further analysis. The quality of the structures was assessed using PROCHECK [157]. Structure diagrams were generated with the program MOLMOL [158].

4.2 Results

4.2.1 Homology Searches

It has been published that MerB lacks sequence homology to any other known proteins [48], and this was confirmed by several database searches prior to structure determination. The full MerB sequence was first compared to the full NCBI sequence database, consisting of nearly 1 million sequences, using the search algorithm PSI-BLAST [159]. The best match found to a non-MerB sequence had an Expect (E) value of 2.3 which is not a significant match for a sequence of this size. The MerB sequence was then compared to the structures in the PDB database using the GenTHREADER algorithm [160]. All resulting matches were rated as low significance by the algorithm. The best matches do contain cysteine residues, but they are not clustered together in an active site as expected for MerB.

4.2.2 EXTENT OF ASSIGNMENTS

The initial backbone resonance assignment was described in Chapter 2. Using the experiments described in the current chapter, some gaps in the backbone assignment were filled. For the backbone ^{1}H, ^{15}N, and ^{13}C resonances of residues 26-212 of the MerB/Hg/DTT complex, 98% of $^{13}C_{\alpha}$, 95% of $^{1}H_{\alpha}$, 97% of the H_N, 92% of the ^{15}N, and 89% of the $^{13}C'$ were assigned. Most of the missing ^{15}N and $^{13}C'$ assignments belong to proline nitrogen atoms and the preceding C' atom.

68% of assignable side-chain resonances (^{1}H-bound ^{13}C and ^{15}N, and ^{1}H, except for ^{1}H-^{15}N and ^{15}N of lysine and arginine) were assigned in residues 26-212 of the MerB/Hg/DTT complex. For 68% of the residues, complete assignment was obtained; 29% of the side-chains were partially assigned, and for 3% of the residues only backbone resonances were assigned. Those residues for which no side-chain resonances were obtained are Y74, H202, M207, S208, T211, and P212, and occur for the most part in the last 10 residues of the protein. Other than the first 25 residues, P212 is the only residue to remain completely unassigned.

The HNCA-D and HN(CO)CA-D experiments were very useful for establishing sequential assignments in segments with overlap in the C_{α} region. For example, in the HNCACB spectrum of a fully protonated sample, the C_{α} resonances of E80 and T81 are not well resolved, and the C_{α} resonances of T81 and S82 are not resolved at all (Figure 4.3B). Both of these pairs are very well resolved in the HNCA-D spectrum of the partially deuterated sample (Figure 4.3A). The improved resolution in the ^{13}C (F_1) dimension in the HNCA-D spectrum is due to the longer acquisition time in this dimension, as well as the use of a constant-time evolution period in t_1 which refocusses the scalar C_{α}-C_{β} coupling. Employment of the constant-time evolution period is not possible with the fully protonated sample because the C_{α} relaxation time is too short compared to the required CT evolution period.

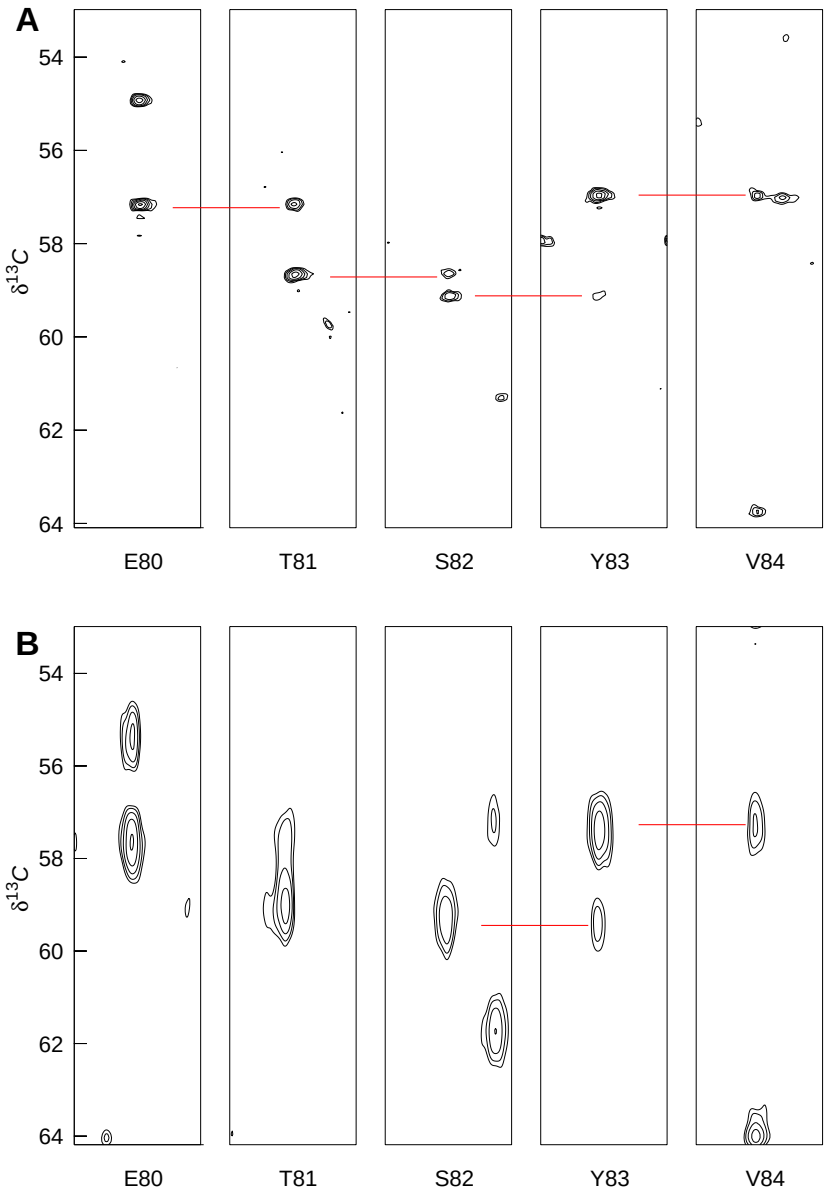

Figure 4.3: Strip plot showing sequential assignments through C_α as seen in (**A**) the HNCA-D [106, 107] experiment and (**B**) the HNCACB [122] experiment. The HNCA-D experiment was recorded on a 70% deuterated MerB/Hg/DTT sample and employed a constant-time evolution period in the carbon dimension.

The TROSY-HNCO based experiments yielded many useful D_{N,H_N}, $D_{N,C'}$, and D_{C',C_α} couplings. The extra separation afforded by the C' dimension greatly aided the resolution in crowded regions of the spectrum. The dipolar couplings measured in the directly detected dimension ($D_{H_N,C'}$ and D_{H_N,C_α}) were less useful due to distortions in the lineshape. The couplings measured in the directly-detected dimension are particularly sensitive to partially resolved, undesired ^{1}H-^{1}H residual dipolar couplings such as H_N-H_α. Such partially resolved couplings could clearly be seen in the spectra. Although alignment tensors and structures could be found that gave good agreement with the three types of heteronuclear-detected coupling, agreement was always poor with the two directly-detected coupling types, so the directly-detected couplings were not employed in structure calculations.

4.2.3 Alignment Tensor

The converged magnitudes of the alignment tensor components were quite similar for the central and carboxyl terminal domains of the MerB/Hg/DTT complex (see Figure 4.4). The magnitudes of the tensor components for the amino terminal domain were slightly different: the overall magnitude was 91% of that for the other two domains, and the rhombicity of the amino terminal was 0.17, vs. 0.50 for the other two domains.

4.2.4 Structure Calculation of the amino terminal Domain

The amino terminal domain of MerB consists of residues 21-79. The structural calculations for the amino terminal domain were based on 330 NOE restraints, 72 residual dipolar coupling restraints, and 61 ψ and ϕ dihedral angle restraints. There were an average of 5.7 NOE restraints per residue. The structure of the domain, and its principal alignment frame,

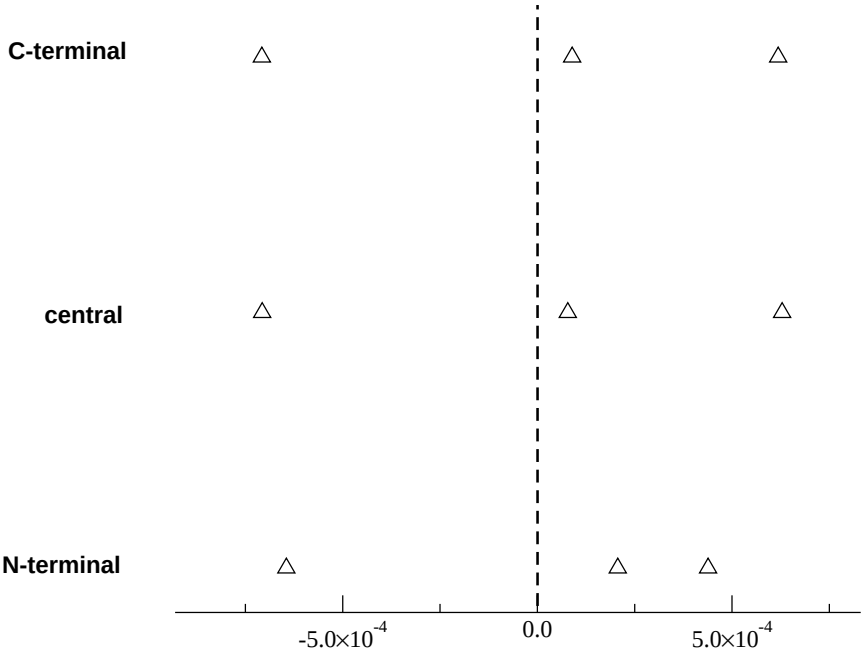

Figure 4.4: Comparison of the magnitudes of the principal components of the alignment tensor for the three domains of the MerB/Hg/DTT complex: amino terminal central, and carboxyl terminal. The magnitudes were determined by fitting the residual dipolar couplings for the domain to the lowest energy structure for that domain by SVD [156].

are shown in Figure 4.5. The secondary structure, using the diagram of Figure 4.2, consists of α-helix H1 (residues 26-32), α-helix H2 (residues 39-46), α-helix H3 (residues 50-58), and the two strands of β-sheet A: β1 (residues 65-66) and β2 (residues 70-71).

The NOE restraints for the amino terminal domain exhibit mainly intrahelical short-range connectivity, together with some long range connectivity between helices. H2 and H3 are defined by a large number of sequential and short-range NOE's (see Figure 4.6). There are also several long-range NOE's defining an interface between the carboxyl terminal cap of H1 and β-sheet A.

Residues 21-25 were included in the structure calculation, although the structure for this region is not well-defined. Resonance assignments in the 21-25 region were limited

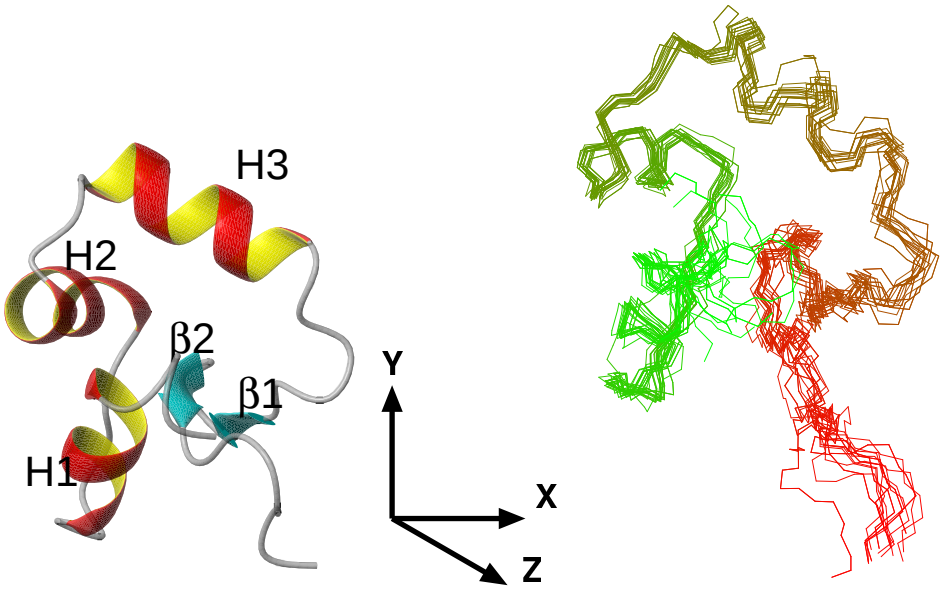

Figure 4.5: Structural diagram of the amino terminal domain (residues 21-80) of the MerB/Hg/DTT complex, placed in the principal alignment frame as determined by SVD [156]. Left: Ribbon diagram of the lowest-energy structure. Right: Bundle of the 20 lowest energy structures, shown as a trace through the backbone atoms. The color progresses from green at the amino terminal to red at the carboxyl terminal of this fragment. The pairwise RMSD for the alignment of the backbone atoms of residues 26-70 is 0.62 Å. The diagrams were generated with MOLMOL [158].

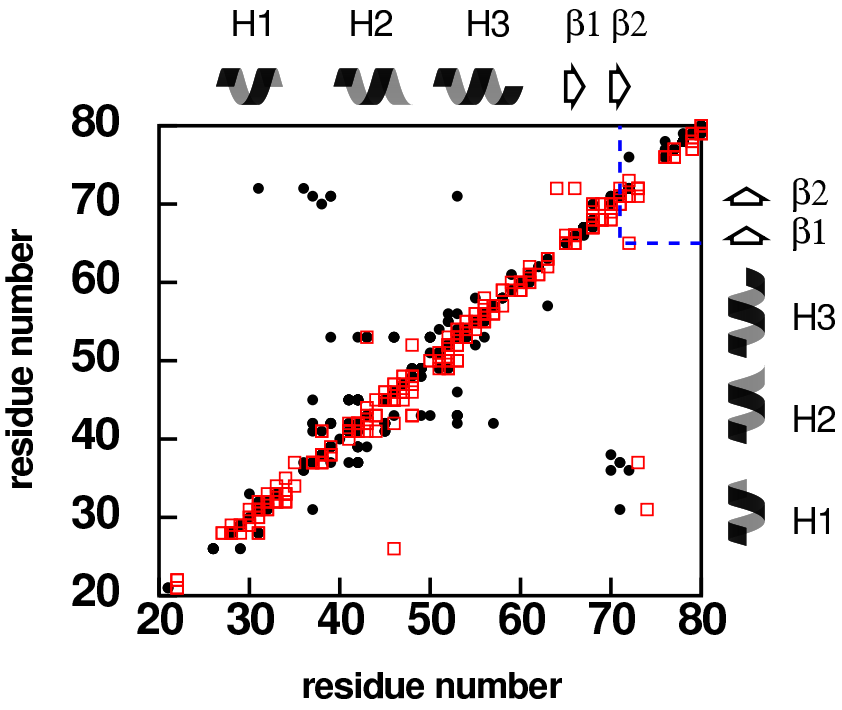

Figure 4.6: NOE connectivity for the amino terminal domain of the MerB/Hg/DTT complex. The residue number of the source proton (from the F_1 dimension) is shown vs. the residue number of the destination proton (from the F_3 dimension) for each NOE restraint derived from (circles) a 3D ^{13}C-edited HMQC-NOESY experiment [142] and (squares) an ^{15}N-edited NOESY-HSQC experiment [141]. Dashed lines show the adjacency of β-strands.

to residues 21 and 22. No NOE restraints were observed between these two residues and the remainder of the protein.

The NOE data support the orientation of H2 and H3 more strongly than that of H1. As seen in Figure 4.6, a group of long-range NOE restraints defines the relationship between H2 and H3. There are very few long-range NOE restraints between the interior of H1 and any other secondary structure elements, although there are NOE restraints between the carboxyl terminal cap of H1 and strand β2. In the absence of residual dipolar coupling restraints, the orientation of H1 relative to the other helices two is not well defined, and in the absence of both residual dipolar coupling and dihedral angle restraints, the helical nature of H1 becomes notably less well defined (data not shown).

The degree of definition of the amino terminal domain is shown by Figure 4.5. The three helices and β-sheet A are the best-defined parts. Residues 21-25 and 71-79 are less well defined. The RMSD of the backbone atoms for the 20 lowest-energy structures is 0.62 Å for residues 26-70, which includes the three helices and β-sheet A.

4.2.5 Structure Calculation of the Central Domain

The central domain of MerB consists of residues 80-137. The structure of the central domain, and its principal alignment frame, are shown in Figure 4.7. Structure calculations were based on 617 NOE restraints, 109 residual dipolar coupling restraints, and 72 dihedral angle restraints. There were an average of 10.8 distance restraints per residue. The secondary structure, following the diagram of Figure 4.2, consists of five extended strands and one helix: β3 (residues 83-87), β4 (residues 90-94), β5 (residues 111-116), β6 (residues 123-128), β7 (residues 132-137), and α-helix 4 (H4, residues 97-103).

The five β-strands of the central domain together form β-sheet B, the largest secondary structure element in the molecule. β3 and β5 are parallel and non-adjacent, and connected by H4. As usual for this type of connection, the crossing is right-handed [152]. C96 occurs near the amino-terminal end of H4; it is positioned over β-sheet B. C117 is also part of

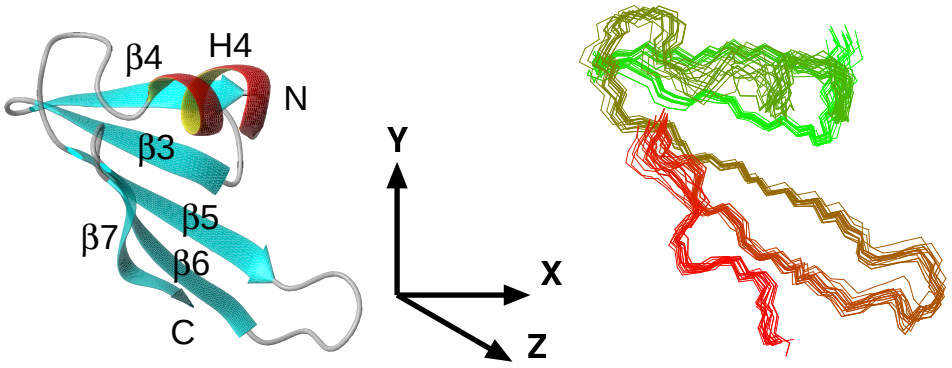

Figure 4.7: Structural diagram of the central domain (residues 80-137) of the MerB/Hg/DTT complex, placed in the principal alignment frame as determined by SVD [156]. Left: Ribbon diagram of the lowest-energy structure. Right: Bundle of the 20 lowest-energy structures, shown as a trace through the backbone atoms. The color progresses from green at the amino terminal to red at the carboxyl terminal of this fragment. The pairwise RMSD for the alignment of the backbone atoms is 0.85 Å. The diagrams were generated with MOLMOL [158].

this domain; it is located in the hairpin turn connecting the antiparallel, adjacent strands β5 and β6.

The NOE connectivity patterns (Figure 4.8) support the secondary structure description, with numerous long-range, inter-strand NOE's observed between all adjacent pairs of strands. There are characteristic short-range and sequential NOE's in H4, but not as many as in the other helices of the protein.

An overlay of the 20 lowest energy structures of the central domain is shown in Figure 4.7. The β strands are well-defined by the NMR data. The RMSD of backbone atoms for the central region is 0.85 Å. The definition is slightly lower in the loop from residues 104-110 connecting H4 and β5. However, the helical shape of H4 was clearly defined. In the free MerB structure, lack of observable NMR signals for several key resonances hindered definition of H4.

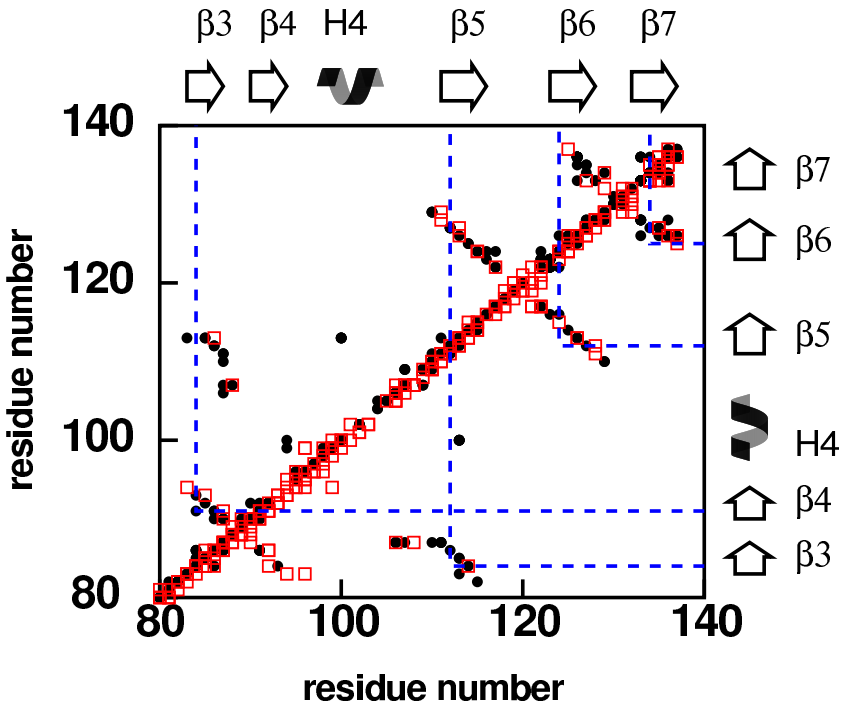

Figure 4.8: NOE connectivity for the central domain of the MerB/Hg/DTT complex. The residue number of the source proton (from the F_1 dimension) is shown vs. the residue number of the destination proton (from the F_3 dimension) for each NOE restraint derived from (circles) a 3D ^{13}C-edited HMQC-NOESY experiment [142] and (squares) an ^{15}N-edited NOESY-HSQC experiment [141]. Dashed lines show the adjacency of β-strands.

4.2.6 Structure Calculation of the Carboxyl-Terminal Domain

The carboxyl terminal domain of MerB consists of residues 138-212. For the structure calculations, residues 207-212 were omitted, because they lack structural restraints and were not well-defined in the free MerB structure. The structure of the carboxyl terminal domain, together with its principal alignment frame, is shown in Figure 4.9. Structure calculations for the carboxyl terminal region used a total of 488 NOE restraints, 101 residual dipolar coupling restraints, and 103 dihedral angle restraints. There were an average of 6.6 distance restraints per residue. Using the secondary structure scheme described in Figure 4.2, the carboxyl terminal region consists of three extended β-strands and two α-helices: β8 (residues 142-145), β9 (residues 163-165), α-helix 5 (H5, residues 168-176), β10 (residues 185-188), and α-helix 6 (H6, residues 190-206). β8, β9, and β10 form β-sheet C. β8 and β9 are adjacent and antiparallel. The loop connecting them is unusually long for this type of connection, and includes the key cysteine pair C159/C160. The connection between strands β9 and β10 has the same topology as the connection between strands β4 and β5. The two sequential strands β9 and β10 form a right-handed connection through the intervening helix H5. β9 and β10 are parallel and non-adjacent with respect to each other, with β8 running in antiparallel fashion between them.

The secondary structure corresponds well with the observed NOE connectivity patterns (Figure 4.10). Long-range, inter-strand NOE's were observed between β8 and its two flanking strands. A large number of sequential and short-range NOE's are seen in the two α helical regions. Several long-range NOE's are also observed between the helices and the β strands against which they are packed.

A superposition of the 20 lowest energy structures is shown in Figure 4.9. β sheet C at the core of this domain as well as the two flanking helices are well defined. The long loop between β8 and β9, containing C159 and C160, is less well defined. The loop consisting of residues 177-184, which connects H5 and β10, is also less well defined than the rest of

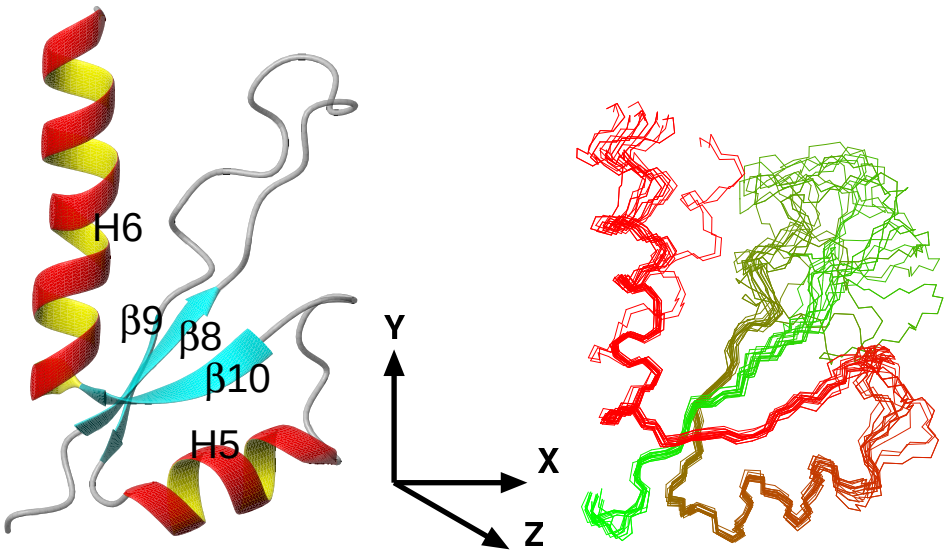

Figure 4.9: Structural diagram of the carboxyl terminal domain (residues 138-206) of the MerB/Hg/DTT complex, placed in the principal alignment frame as determined by SVD [156]. Left: Ribbon diagram of the lowest-energy structure. Right: Bundle of the 20 lowest-energy structures, shown as a trace through the backbone atoms. The color progresses from green at the amino terminal to red at the carboxyl terminal of this fragment. The pairwise RMSD for the alignment of the backbone atoms, excluding the two disordered loop regions consisting of residues 146-162 and 177-184, is 0.82 Å. The diagrams were generated with MOLMOL [158].

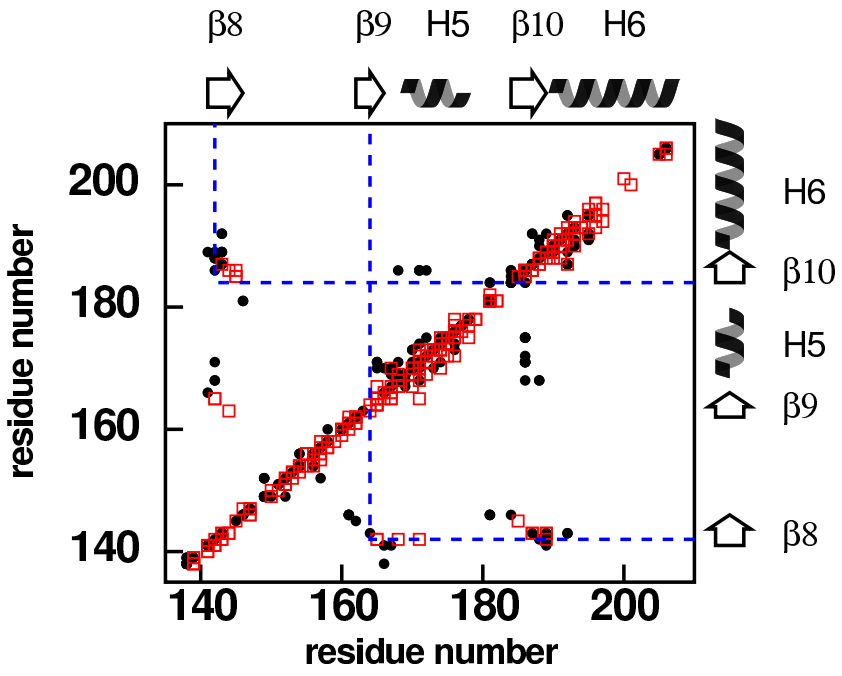

Figure 4.10: NOE connectivity for the carboxyl terminal domain of the MerB/Hg/DTT complex. The residue number of the source proton (from the F_1 dimension) is shown vs. the residue number of the destination proton (from the F_3 dimension) for each NOE restraint derived from (circles) a 3D ^{13}C-edited HMQC-NOESY experiment [142] and (squares) an ^{15}N-edited NOESY-HSQC experiment [141]. Dashed lines show the adjacency of β-strands.

the domain. The pairwise RMSD of the position of the backbone atoms of the 20 lowest energy structures, excluding residues 146-162 and 177-184 in the flexible loop regions, is 0.82 Å.

4.2.7 ^{15}N Relaxation Experiments

^{15}N relaxation experiments suggest that the lower definition observed in the 146-162 and 177-184 regions of the MerB/Hg/DTT structure reflects actual flexibility in the molecule, and not just lack of restraint data in those regions. ^{15}N T_1, ^{15}N T_2, and ^{15}N-^{1}H heteronuclear NOE data are shown in Figure 4.11. In both the loop connecting β8 and β9 (residues 146-162) and the loop connecting H5 and β10 (residues 177-184), the T_1 values (Figure 4.11A) and the ^{15}N-^{1}H heteronuclear NOE values (Figure 4.11C) are significantly below the average. This indicates motion for the loops on a time scale faster than the overall correlation time of the molecule. Low ^{15}N-^{1}H heteronuclear NOE values are also observed for several residues at the extreme carboxyl terminus due to fraying of the end of α-helix H6. In the loop connecting H3 and β1, one residue (Q59) has a low ^{15}N-^{1}H NOE value.

The loop connecting strands β2 and β3 (residues 71-79) forms the connection between the amino terminal domain and the central domain. In the full MerB/Hg/DTT structure, the relative orientation of the amino terminal domain and the other two domains is less well defined than the structure of the domains individually. The lack of definition may be due to motion of the amino terminal domain relative to the remainder of the molecule, via flexibility in the β2-β3 loop. Such motion may explain the observed differences in alignment tensor magnitudes between the domains (Figure 4.4). However, the ^{15}N relaxation parameters in the β2-β3 loop are similar to the average values for the MerB/Hg/DTT complex (Figure 4.11). Therefore, while the β2-β3 loop may be flexible, it does not undergo rapid (pS) motions similar to those experienced by the β8-β9 and H5-β10 loops.

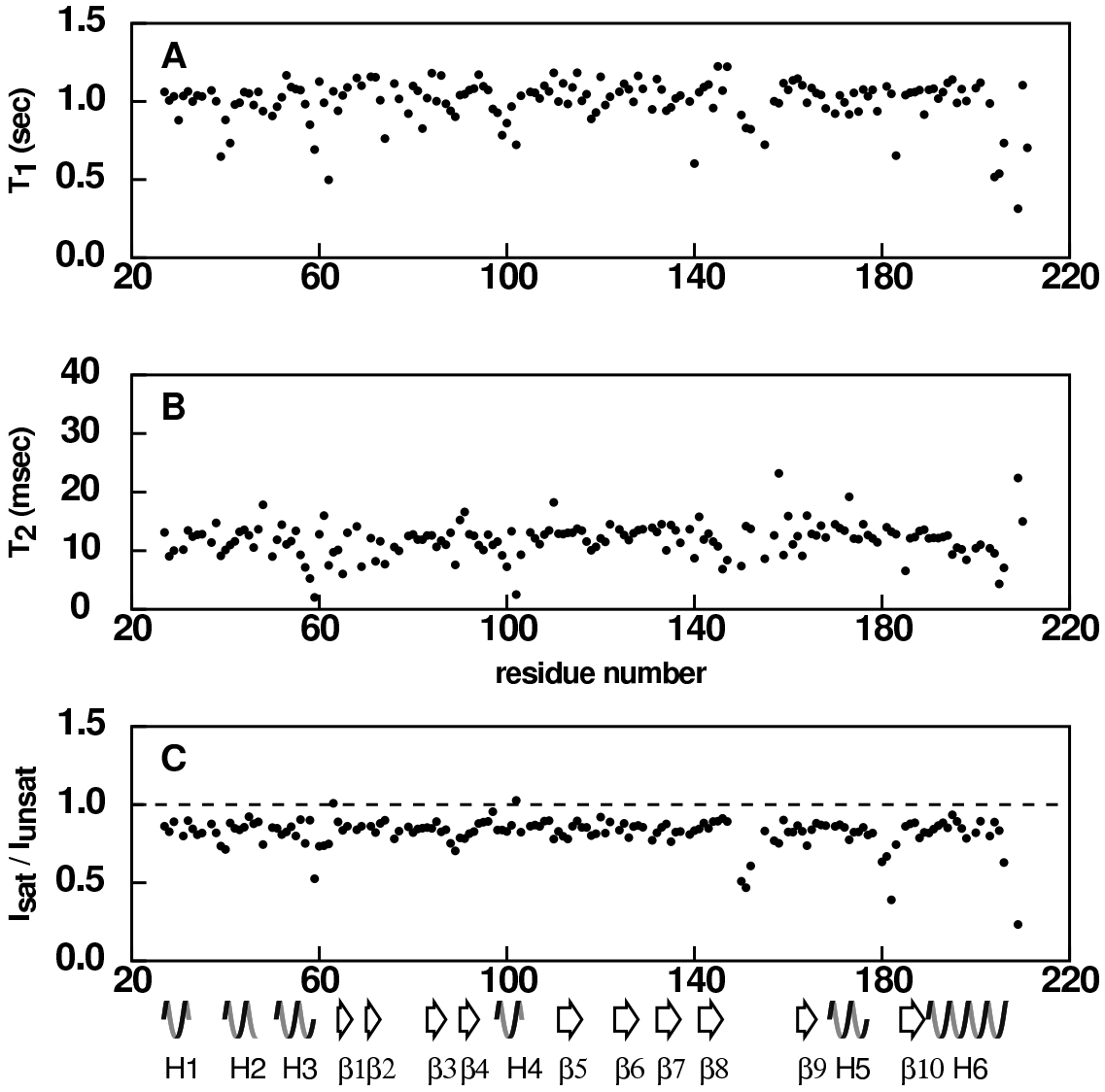

Figure 4.11: ^{15}N relaxation data for the MerB/Hg/DTT complex. (A) T_1, (B) T_2, and (C) heteronuclear ^{15}N-^{1}H NOE are shown as a function of residue number.

4.2.8 DTT BINDING

The DTT molecule contains three pairs of magnetically equivalent protons. The (magnetically equivalent) C2 and C3 protons of DTT resonate at 3.74 ppm in free DTT in standard NMR buffer. Even when the DTT molecule is bound to the chiral protein as part of a MerB/Hg/DTT complex, the C2 and C3 protons of DTT are magnetically equivalent if the DTT molecule is free to rotate about the bond joining Hg(II) to C96. There is a peak at this chemical shift in the 1D ^{13}C-filtered watergate spectrum (Figure 4.12) of the MerB/Hg/DTT complex, which is therefore assigned to the C2 and C3 protons of DTT in the complex. There are several other peaks apparent in the ^{13}C-filtered watergate spectrum (Figure 4.12). These peaks are probably due to the methylene protons of DTT, which resonate at 2.67 ppm in free DTT. NOE crosspeaks (see below) were only observed to the C2 and C3 protons of DTT.

The F_1-(^{13}C)filtered, F_3-(^{13}C)edited ^{13}C NOESY-HSQC experiment contained only four clear signals (Figure 4.13). All four appear at the chemical shift of the DTT C2 and C3 protons in the F_1 dimension. In the F_2 and F_3 dimensions, two of the signals were assigned to the methyl groups of V113 in the MerB protein, and one signal was assigned to a methyl group of V128 of MerB (see Figure 4.13). V113 is part of β5, and V128 is at the end of the adjacent strand β6. Both of these strands are part of the large β sheet in the central domain. The fourth signal (not shown) belonged to an unassigned aromatic resonance at 6.67 ppm. Several protons from the unassigned aromatic group of F164 are within 5 Å of the DTT molecule.

4.2.9 OVERALL STRUCTURE CALCULATIONS

The overall structure calculation included the restraints from the individual domain calculations, as well as some inter-domain NOE's and the intermolecular NOE's between the protein and the DTT molecule. There were only three interdomain NOE restraints

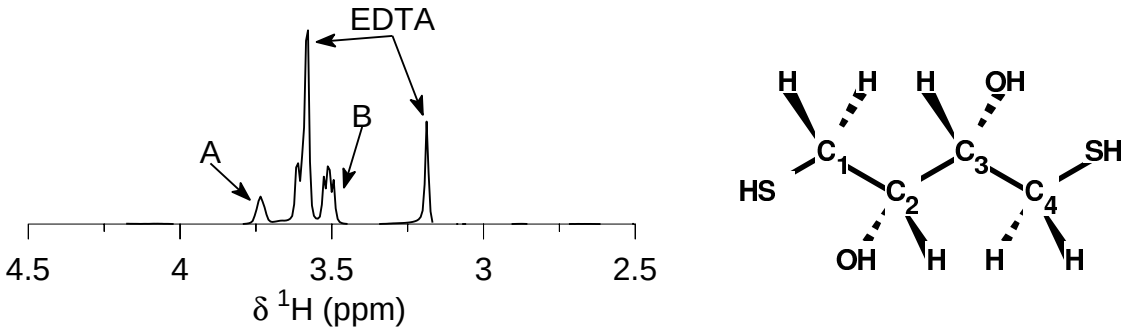

Figure 4.12: Left: 1D ^{13}C-filtered WATERGATE spectrum of $^{13}C/^{15}N$-labeled MerB/Hg/DTT complex [149]. The large peaks at 3.6 and 3.2 ppm are due to EDTA in the buffer. The other peaks are (A) the magnetically equivalent C2 and C3 protons of DTT and (B) the C1 and C4 methylene protons of DTT. Intermolecular NOE's between MerB and DTT were only observed to the C2 and C3 protons. The structure of DTT is shown at right.

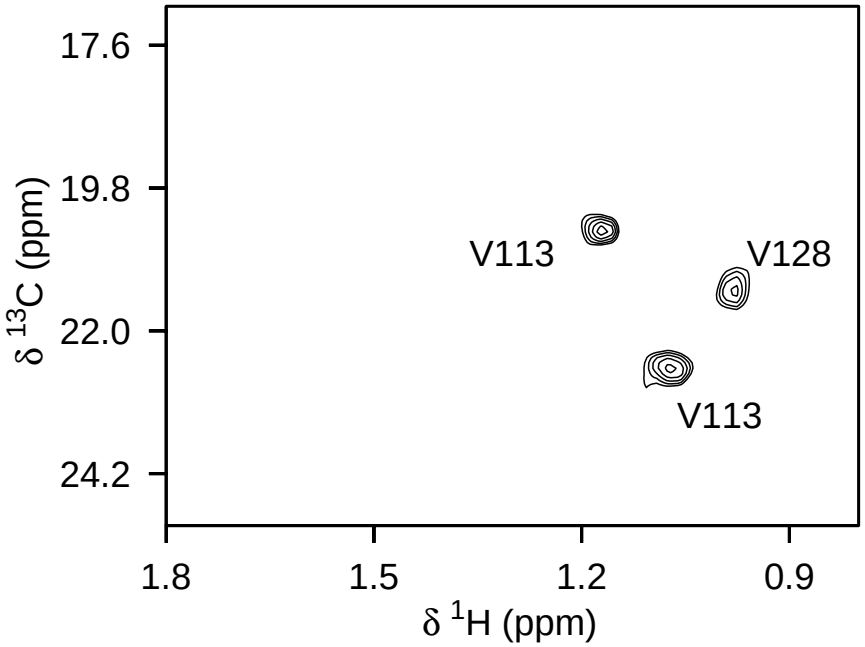

Figure 4.13: Intermolecular NOE crosspeaks observed between DTT and MerB in the MerB/Hg/DTT complex. An (F_2, F_3) slice at F_1 = 3.74 ppm of the F_1-(^{13}C)filtered, F_3-(^{13}C)edited NOESY-HSQC experiment is shown. The F_1 chemical shift corresponds to the chemical shift of the two protons bound to C2 and C3 of DTT. The chemical shifts in the F_2 and F_3 dimensions were assigned to several valine methyl resonances as labeled. The valine methyl groups are not stereospecifically assigned.

between the amino terminal and central domains: from H_δ of I107 to H_N of A32, from H_N of Y93 to H_N of T77, and from H_α of A94 to H_N of T77. There were 31 long-range, inter-domain NOE restraints between the central domain and the carboxyl terminal domain. These long-range NOE's were mostly between side-chain atoms, and could be grouped into four classes: between β6 and β9, between the amino terminal end of H6 and β7, between H5 and the hairpin loop connecting β5 and β6, and between β9 or β8 and H4. The overall structure calculations also included the three assigned NOE restraints between the protein and the DTT molecule. In total, the structure calculation was based on 1588 NOE restraints, 259 dihedral angle restraints, and 285 residual dipolar coupling restraints (see Table 4.1). A total of 50 structures with no NOE violation greater than 0.5 Å and no backbone dihedral angle restraint violation greater than 5 degrees were calculated. From this set, the 20 lowest-energy structures were selected for further analysis.

In the overall structure, the relative orientation of the carboxyl terminal and central domains is well-defined. The core domain of the protein is defined as the combination of the carboxyl terminal and central domains, consisting of residues 80-212. The resolution of the core domain, excluding the last 6 residues and the two flexible loops consisting of residues 146-162 and 177-184, is 0.85 Å pairwise RMSD for the backbone atoms, and 1.61 Å for all heavy atoms (see Table 4.1). The resolution of the amino terminal domain, consisting of residues 26-80, was also good in the overall structure: 0.71 Å pairwise RMSD for the backbone atoms, and 1.53 Å for all heavy atoms. When the entire structure consisting of all three domains is superimposed, the resolution is slightly lower: 1.11 Å pairwise RMSD for the backbone atoms and 1.80 Å for all heavy atoms. A superposition of the 20 lowest energy structures is shown in Figure 4.14. The decrease in resolution is due to differences in the relative orientation of the amino terminal domain and the core domain of the protein between different members of the ensemble of structures. The difference in alignment tensor asymmetry and magnitude seen for the core domain

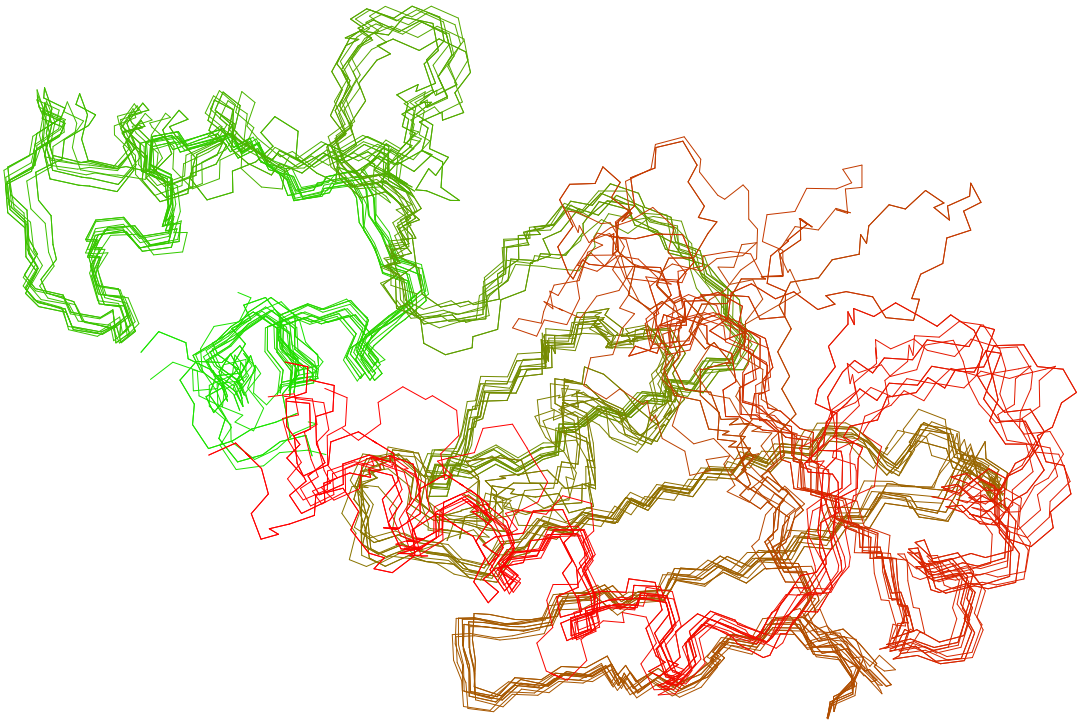

Figure 4.14: Bundle of the 20 lowest energy structures of the MerB/Hg/DTT complex. The pairwise RMSD of the backbone atoms is 1.11 Å, excluding the disordered loop regions from residues 146-162 and 177-184. The color of the backbone bonds progresses from green at the amino terminal to red at the carboxyl terminal.

vs. the amino terminal domain (see Figure 4.4) supports the idea that this variation in the relative orientation reflects the actual mobility of the amino terminal domain of MerB.

4.2.10 Description of the Overall Structure

The structure of the MerB/Hg/DTT complex is well-defined between residues 26 and 206. The overall structure is shown in Figure 4.16, and a stereo view is shown in Figure 4.15. The first 25 residues and the final 6 residues are less well-defined due to a lack of observable signals, and hence structural restraints, in these regions.

Table 4.1: Structural statistics for the MerB/Hg/DTT complex.

Restraints used for the structure calculation	
Total NOE distance restraints	1588
Intra-residue	721
Sequential($\|i-j\| \leq 4$)	580
Long-range($\|i-j\| > 4$)	287
Dihedral angle restraints (ϕ, ψ)	259
Residual dipolar coupling restraints ($^1D_{NH}$, $^1D_{NC'}$, $^1D_{C_\alpha C'}$)	275
Structural Statistics	
R.m.s. deviations from idealized geometry	
Bonds (Å)	0.003 ± 0.00003
Impropers (degrees)	0.48 ± 0.0061
R.m.s. deviation from dihedral restraints (degrees)	0.73 ± 0.012
Angles (degrees)	0.53 ± 0.0035
R.m.s. deviation from distance restraints (Å)	0.021 ± 0.00024
R.m.s. deviations from dipolar coupling restraints (Hz)[a]	
$^1D_{NH}$	1.82 ± 0.11
$^1D_{C_\alpha C'}{}^{(b)}$	1.41 ± 0.10 (7.05 ± 0.55)
$^1D_{NC'}{}^{(b)}$	0.69 ± 0.06 (5.72 ± 0.50)
Procheck statistics (%)	
Residues in most favored regions	79.3
Residues in additional allowed regions	15.9
Residues in generously allowed regions	1.8
Residues in disallowed regions	3.0
Atomic pairwise RMSD (Å) for backbone atoms (C', C_α, N)	
Overall structure[c]	1.11
Core domain[d]	0.85
N-terminal domain[e]	0.71
Atomic pairwise RMSD (Å) for all heavy atoms	
Overall structure[c]	1.80
Core domain[d]	1.61
N-terminal domain[e]	1.53

[a] Mean value, over the 20 lowest energy structures, of the root mean square deviation between the measured and the calculated values of the residual dipolar couplings.
[b] Values in parenthesis for $^1D_{C_\alpha C'}$ and $^1D_{NC'}$ are normalized to $^1D_{NH}$ by factors of 5.0 and 8.3, respectively.
[c] For residues 26-206, excluding the loop regions 146-162 and 177-184.
[d] For residues 80-206, excluding the loop regions 146-162 and 177-184.
[e] For residues 26-80.

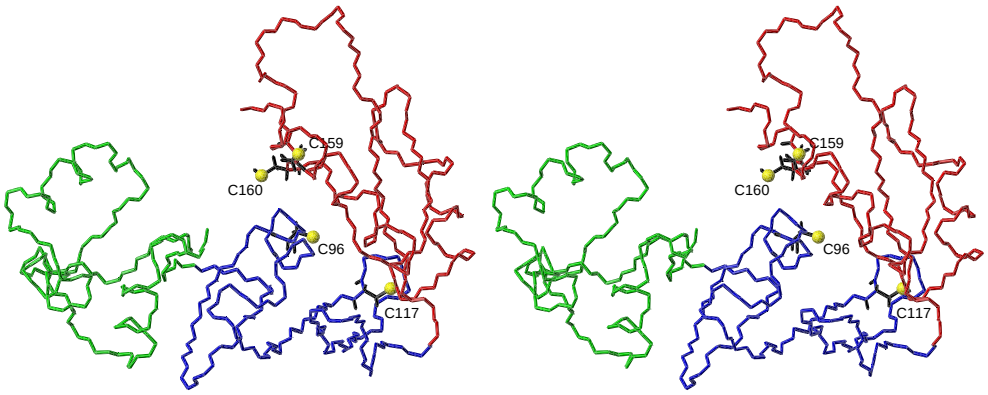

Figure 4.15: Stereo view of the backbone of the lowest-energy MerB/Hg/DTT structure. The amino terminal domain is shown in green, the central domain is shown in blue, and the carboxyl terminal domain is shown in red.

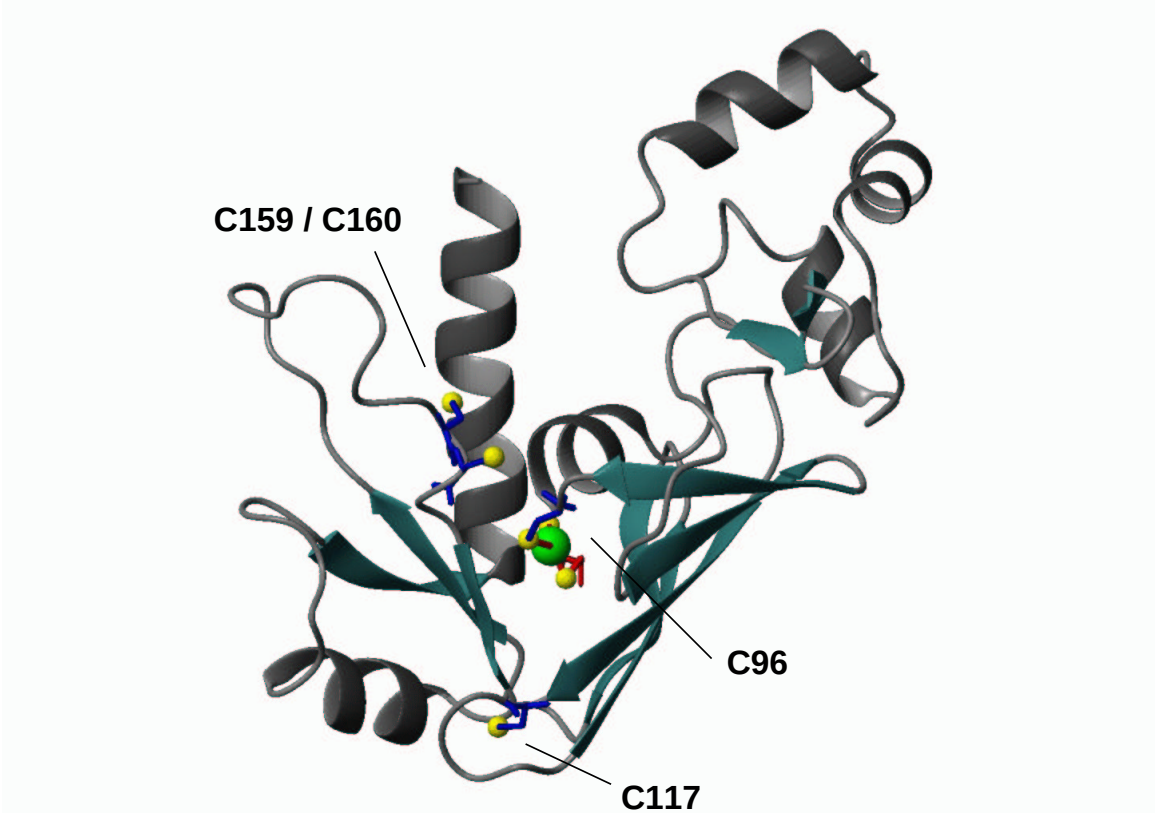

Figure 4.16: Ribbon diagram of the lowest-energy MerB/Hg/DTT structure showing the binding site of DTT. The mercury atom is shown in green. The DTT molecule is shown in red. Sulfur atoms are shown in yellow.

Residues 26-32 and 39-46 form α-helices H1 and H2, respectively. These α-helices pack against each other, with side-chain interactions occurring between residues P26 and E30 of H1, and T41, T45, and L46 of H2. The third α-helix H3 consists of residues 50-58. There are numerous hydrophobic interactions at the junction of α-helices H2 and H3, with contacts between the side-chains of A43, W48, A50, and V53. The two extended strands β1 (residues 65-66) and β2 (residues 70-71) form β-sheet A. The conformation of β-sheet A is supported by several inter-strand backbone NOE's (see Figure 4.18). Strands β1 and β2 are joined by a hairpin turn of type II′, which is stabilized by a hydrogen bond between the carbonyl oxygen of D66 and the amide proton of G69 [161, 162]. β2 also interacts with residues S38, V37, and R39 in the loop connecting H1 and H2.

The central domain contains β-sheet B, which is the largest secondary structure element in the molecule. The five β strands composing this sheet are held together in the structure by numerous inter-strand backbone NOE restraints (see Figure 4.18). An interesting feature of this β-sheet is a β bulge involving residues 133-135 in strand β7. The connection between β5 and β6 can be classified as a sequence of two hairpin turns of type IV (residues 117-120 and 118-121). These tetrads of residues are classified as turns because the (i) and (i+3) C_α carbons are within 7.1 Å [162]. However, these turns do not exhibit the (i, i+3) backbone hydrogen bonds often observed in hairpin turns. A type I turn, stabilized by a hydrogen bond between the carbonyl oxygen of S129 and the amide proton of E132, connects β6 and β7.

H4 is the shortest α-helix in the molecule, and contains the critical active-site residue C96. An interesting feature of this α-helix is the carboxyl terminal termination by P104 [163]. The pyrrolidine ring of P104 makes contacts with the side-chains of L101 and T100. Evidently, this structural motif is highly conserved among *merB* genes, because positions 101 and 104 are almost always conserved to leucine and proline, respectively [48].

β-sheet B in the central domain and β-sheet C of the carboxyl terminal domain are oriented nearly at right angles with respect to each other. P138 occurs at the junction of

the two domains, and helps introduce a sharp twist in the chain. This structural feature is apparently also highly conserved among *merB* genes, with position 138 always conserved to proline [48]. The observation of this highly conserved residue, and its structural role in MerB from plasmid R831b, suggests that the arrangement of the central and carboxyl terminal domains is similar in different MerB family members.

The carboxyl terminal domain of MerB consists of β-sheet C and α-helices H5 and H6. The structure of β-sheet C is supported by interstrand NOE restraints between β8 and the flanking strands β9 and β10 (Figure 4.18). There are several stabilizing hydrophobic interactions between β-sheet B and β-sheet C involving residues S115, V124, and F164. Several hydrophobic side-chains of H5, belonging to V168, A171, and A175, pack against residues A142, F165, I186, and S188 of β-sheet C. The hairpin loop from residues 117-122 between β5 and β6 in the central domain also makes contact with H5. At the base of H6, residues A192 and L195 interact with the side-chain of V187 in β10. Beyond the amino terminal base of H6, there is not much contact between this rather long α-helix and the remainder of the protein. Two loops within the carboxyl terminal domain are the least well-defined portions of the MerB/Hg/DTT structure, other than the first 25 residues. The first of these loops, consisting of residues 146-162, connects β8 and β9, and contains the C159/C160 pair. The second flexible loop consists of residues 177-184 and connects H5 to β10. The flexibility of both of these loops is supported experimentally by the ^{15}N-^{1}H heteronuclear NOE data (Figure 4.11C).

The solution of the MerB/Hg/DTT structure allowed a comparison between the obseved NOE crosspeaks and those expected based on the β-sheet topology (Figure 4.18). In some cases, the expected inter-strand H_α-H_α and H_α-H_N correlations were not present in the set of restraints used for structure calculations due to peak overlap, proximity to the diagonal, ambiguity, baseline artifacts, or a combination of these factors. However, re-examination of the ^{15}N-edited NOESY-HSQC and 3D ^{13}C-edited HMQC-NOESY experiments following structure determination allowed identification of several of the

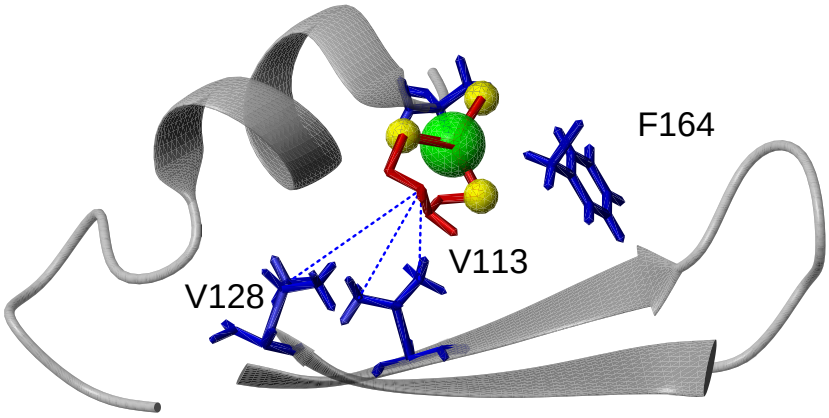

Figure 4.17: Closeup of the DTT binding pocket in the MerB/Hg/DTT structure. NOE restraints between the protein and the DTT molecule are shown as dashed lines. The bonds of the DTT molecule are shown in red. The sulfur atoms are yellow and the mercuric ion is green. Ribbons are shown for H4 and strands β5 and β6.

missing expected correlations. For the additional correlations identified, it was confirmed that the atoms involved were within 5 Å in the lowest-energy structure.

The DTT molecule, attached to C96 through the mercury atom, is situated in a pocket between the carboxyl terminal and central domains. A closeup view of this configuration is shown in Figure 4.17. Although this conformation of C96 places the Hg(II)/DTT moiety in a hydrophobic pocket, the Hg(II)/DTT moiety could be placed into the solvent by a simple rotation of the C96 C_α-C_β bond, without any reorganization of the backbone fold.

Of the four cysteine residues in the MerB/Hg/DTT complex, C159 and C160 are the most solvent-exposed, C96 is the next most solvent-exposed, and C117 is the least solvent-exposed. C159 and C160 are part of the flexible loop between strands β8 and β9. The side-chains of C159 and C160 point out into the solvent. C96 occurs at the amino terminal end of α-helix H4. C96 is on the surface of the protein, but the side-chain of C96 points

inwards due to the positioning of the bound Hg(II)/DTT moiety. C117 is part of the hairpin loop between strands β5 and β6. The side-chain of C117 is completely protected from the solvent by the side-chains of residues A119, T120, A122, A166, and T170. In addition, the side-chains of several residues in strand β9 form a barrier between C117 and the other three cysteine residues.

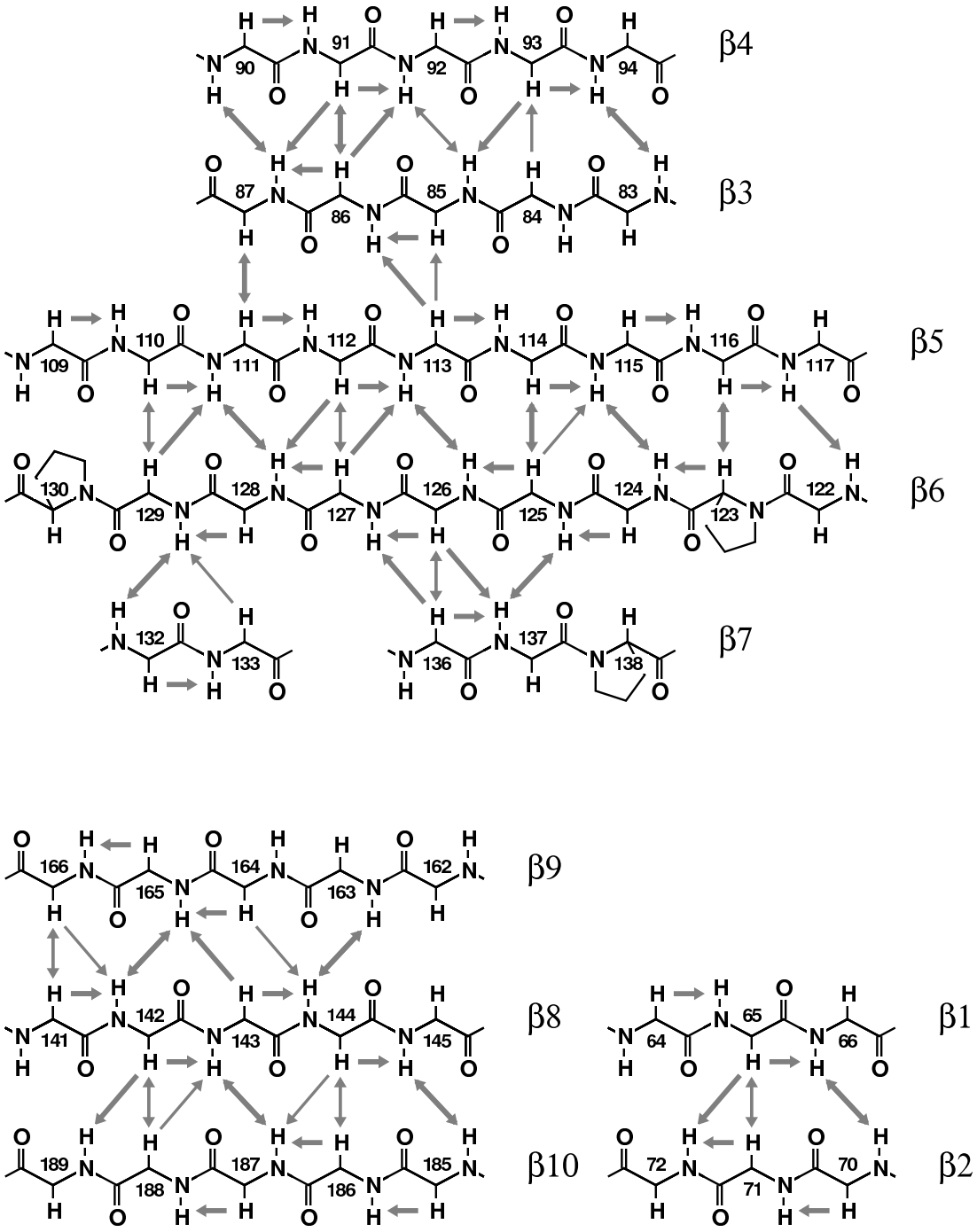

Figure 4.18: Sequential and long-range NOE's observed in the MerB/Hg/DTT complex between backbone atoms in β-sheet B (top), β-sheet C (lower left), and β-sheet A (lower right). Thin arrows represent weak NOE restraints. Thick arrows represent medium and strong NOE restraints.

4.3 DISCUSSION

4.3.1 DOMAIN ORIENTATION

The values of the alignment tensor magnitudes for the three domains of the MerB/Hg/DTT complex (Figure 4.4) are consistent with several observations about the structure. The central and carboxyl terminal domains were found to have very similar alignment tensors. There are numerous contacts between the central and carboxyl terminal domains, as well as a relatively large number (31 total) of long-range NOE restraints between the two. In contrast, there were only three observable long-range NOE restraints between the amino terminal domain and the central domain. Also, the amino terminal and central domains are only connected by a less well-defined loop consisting of residues 71-80. The lower resolution of the overall structure (Figure 4.14) as compared to the resolution of the individual domains is mainly due to a lack of definition of the orientation of the amino terminal domain relative to the other two domains. The alignment tensor data show that this is a real phenomenon in the MerB/Hg/DTT complex and not a consequence of the lesser extent of resonance assignments in the region of residues 70-80. Internal motions of molecules can lead to local average alignments different from the global average alignment [164]. In the MerB/Hg/DTT complex, the most pronounced difference in the alignment tensors calculated for each domain individually is a decrease in rhombicity for the amino terminal domain (R = 0.17) vs. the rhombicity of the other two domains (R = 0.50). Many different models for interdomain motion could explain this difference in rhombicity. One of the simplest is a model in which the amino terminal domain wobbles about the Z axis of the global alignment tensor. Calculations have shown that a wobbling motion averaging 40^o is sufficient to produce the observed change in rhombicity (see Appendix B).

4.3.2 INDIVIDUAL DOMAIN CALCULATION

The division of a larger molecule such as MerB into domains for separate structure calculation is useful because it speeds the initial stages of structure determination, and it allows a separate domain-by-domain consideration of the alignment tensor. The potential time savings through domain-by-domain calculations can be seen by a simple probability argument. Let there be a probability p that a particular restraint will be satisfied in a structure calculation. Then, to a first approximation, the probability of all restraints being simultaneously satisfied is p^n, where n is the number of restraints. Because $p < 1$, the probability of simultaneously satisfying all restraints decreases exponentially with increasing molecular size; for large structures, the probability becomes very low. The time needed to solve the structure as a single unit is proportional to p^{-n}. The time needed to solve the structure as separate domains is proportional to $m \sum_m p^{-n/m}$, where m is the number of domains. In protein structure determination, the number of restraints n is on the order of one thousand; therefore $p^{-n} \gg m \sum_m p^{-n/m}$. This is, of course, an oversimplification, because all restraints do not have an equal probability of satisfaction, nor are they uncorrelated. However, the strong inverse relationship between molecular size and probability of restraint satisfaction was always seen in the MerB/Hg/DTT calculations. Because structure determination is usually an iterative process, consisting of cycles of simulated annealing following the determination of parameters such as alignment tensor components, NOE calibrations, and force constants, it makes sense to optimize the parameters on small molecular fragments, and then use the optimized parameters in a final calculation of the whole molecule.

The separate domain-by-domain calculation was also useful because it allowed more flexibility in the interpretation of residual dipolar couplings. The magnitudes of residual dipolar couplings are a function of the overall alignment of the molecule as well as internal motions. For the sake of simplicity, it is often assumed that the internal motions influ-

ence all residual dipolar couplings in the molecule equally. In reality, internal motion in different parts of the molecule may influence the residual dipolar couplings differently [164]. One simple compromise between simplicity and accuracy is to assign each domain a separate alignment tensor with the same orientation, but different magnitudes. This amounts to the usual assumption of uniform internal motion effects within a domain, but allows for different degrees of motion for the different domains. In the case of the MerB/Hg/DTT complex, the observed residual dipolar couplings could be fit very well for the individual domains (Figure 4.4). The tensor magnitudes for the central and carboxyl terminal domains were similar to each other, but significantly different in both magnitude and asymmetry from the amino terminal domain's alignment tensor. Increased motion of the amino terminal domain relative to the rest of the protein would cause this change, and this is consistent with the observation that the amino terminal domain is connected to the rest of the protein through a single flexible loop that is not very well defined in the structure. The assumption that the alignment tensor should have an equal orientation in the three domains is in agreement with the observed interdomain NOE restraints. The imposition of equal orientations on each domain's alignment tensor did not disrupt the agreement between calculated and observed residual dipolar couplings seen in the individual domain calculations, even when the orientation between domains was also constrained by NOEs.

4.3.3 USE OF RDC RESTRAINTS

There are some fundamental differences in the interpretation of NOE restraints vs. residual dipolar coupling restraints in terms of structure calculation. An unambiguously assigned NOE which is not due to spin diffusion can only be satisfied by bringing two atoms to within a specified distance of each other. In contrast, there are several quite different ways that a residual dipolar coupling restraint can be satisfied. A residual dipolar coupling restraint does not constrain an internuclear vector to a single orientation, but rather to one of the many orientations which satisfy the condition $D \propto \left\langle 3cos^2\theta - 1 \right\rangle$. A residual

dipolar coupling restraint can be satisfied through rotation of the alignment tensor relative to the entire molecule, through adjustment of the relative orientations of different domains, or through local adjustments in conformation, including small changes in bond angles or impropers. The calculation of an anisotropy energy alone does not distinguish these possibilities very well. It is important to consider whether the calculated anisotropy energies correspond to global minima, and whether the alignment tensor orientations between different structure calculation trials agree. In calculations on the MerB/Hg/DTT complex, the agreement was good between alignment tensor orientations obtained from different simulated annealing calculations, suggesting that the calculated orientation is at a global minimum (Figure 4.19). Also, the orientation derived from simulated annealing is in agreement with the orientation derived from SVD [156].

4.3.4 DTT BINDING

The DTT molecule in the MerB/Hg/DTT complex is buried in a pocket between the central and carboxyl terminal domains (Figure 4.16). This is consistent with the high stability of the MerB/Hg/DTT complex (see Section 3.2.2), in contrast with standard HgS_3 complexes which are usually labile [131]. It is also consistent with the observation that even a small amount of DTT inhibits MerB turnover in the presence of cysteine or glutathione [48].

In Chapter 3, it was shown that the reaction rate of MerA with the MerB/Hg/DTT complex as a substrate is most consistent with a direct transfer of the mercuric ion from MerB to MerA. In the NMR structure of the MerB/Hg/DTT complex, the mercuric ion is situated in such a way that transfer to another protein would be possible. Although the most solvent-exposed cysteine residues in the MerB/Hg/DTT complex are C159 and C160, C96 is also on the surface of the protein. The mercuric ion occurs in the cleft between the carboxyl terminal domain and the central domain. No major reorientation of the secondary structure or global fold would be required to remove the mercuric ion. A

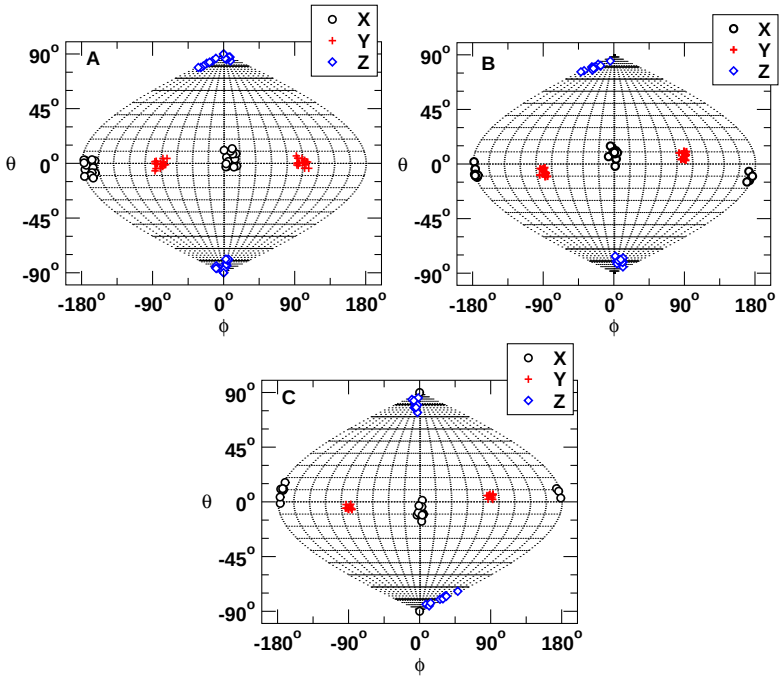

Figure 4.19: Orientation of the alignment tensor as obtained by simulated annealing, vs. the orientation of the tensor as obtained by SVD [156], for (A) the amino terminal domain, (B) the central domain, and (C) the carboxyl terminal domain. For each of the three domains, the lowest energy structure was placed in the principal alignment frame as determined by SVD. A bundle of 15 structures was then aligned to this first structure by minimizing the RMSD in the position of the backbone atoms. The anisotropy atoms rotate with the molecules as they are aligned. The orientation of the three Cartesian axes defined by the anisotropy atoms is shown in the principal alignment frame for the lowest-energy structure.

small change in the interdomain orientation between the central and carboxyl terminal domains would expose the bound mercuric ion to an even larger surface area, able to accomodate a larger portion of another protein.

An initial estimate of the binding site for Hg/DTT was discussed in Chapter 2 on the basis of chemical shift perturbations between a complex involving (R,R)-DTT and one involving (S,S)-DTT. Most of the perturbed residues are in fact near the DTT binding site in the MerB/Hg/DTT complex, but they do not form a tight cluster (see Figure 4.20). This observation might at first seem paradoxical, but it is actually consistent with the magnitude of the perturbations and the structural environment of the residues involved. None of the chemical shift differences between the (R,R)-DTT and (S,S)-DTT complex are very large; all changes are below 0.2 ppm in ^{15}N chemical shift and below 0.05 ppm in ^{1}H chemical shift. Changes of this magnitude are observed throughout the protein sequence upon transition from the free form to the MerB/Hg/DTT complex (Figure 2.8). Clearly, changes of this small magnitude do not require close proximity to the mercury binding site. For residues that are near the binding site, the change in backbone chemical shift upon transition from free to mercury-bound form is much larger, often greater than 0.2 ppm in ^{1}H chemical shift (see Figure 2.8). All of the perturbed residues are either near the point of chemical attachment of DTT (residue 96), or on adjacent flexible loops which would be easily perturbed by small changes in the C96 region. Residues V113 and V128 are not perturbed residues, although these residues exhibit NOE crosspeaks to the DTT molecule. Both of these residues are part of the central β sheet which is the most rigid part of the molecule, and which would not be easily perturbed by a change as small as the substitution of (R,R)-DTT for (S,S)-DTT. The chemical shift perturbations seen in the MerB/Hg/DTT complex upon exchange of (R, R)-DTT for (S, S)-DTT are therefore illustrative of several considerations for the use of chemical shift perturbations in general. The chemical shift perturbation of a residue depends not only on the proximity of that residue to the perturbing ligand, but also on the structural flexibility of that residue. Further, small

structural changes can generate small chemical shift perturbations which propagate over considerable distances.

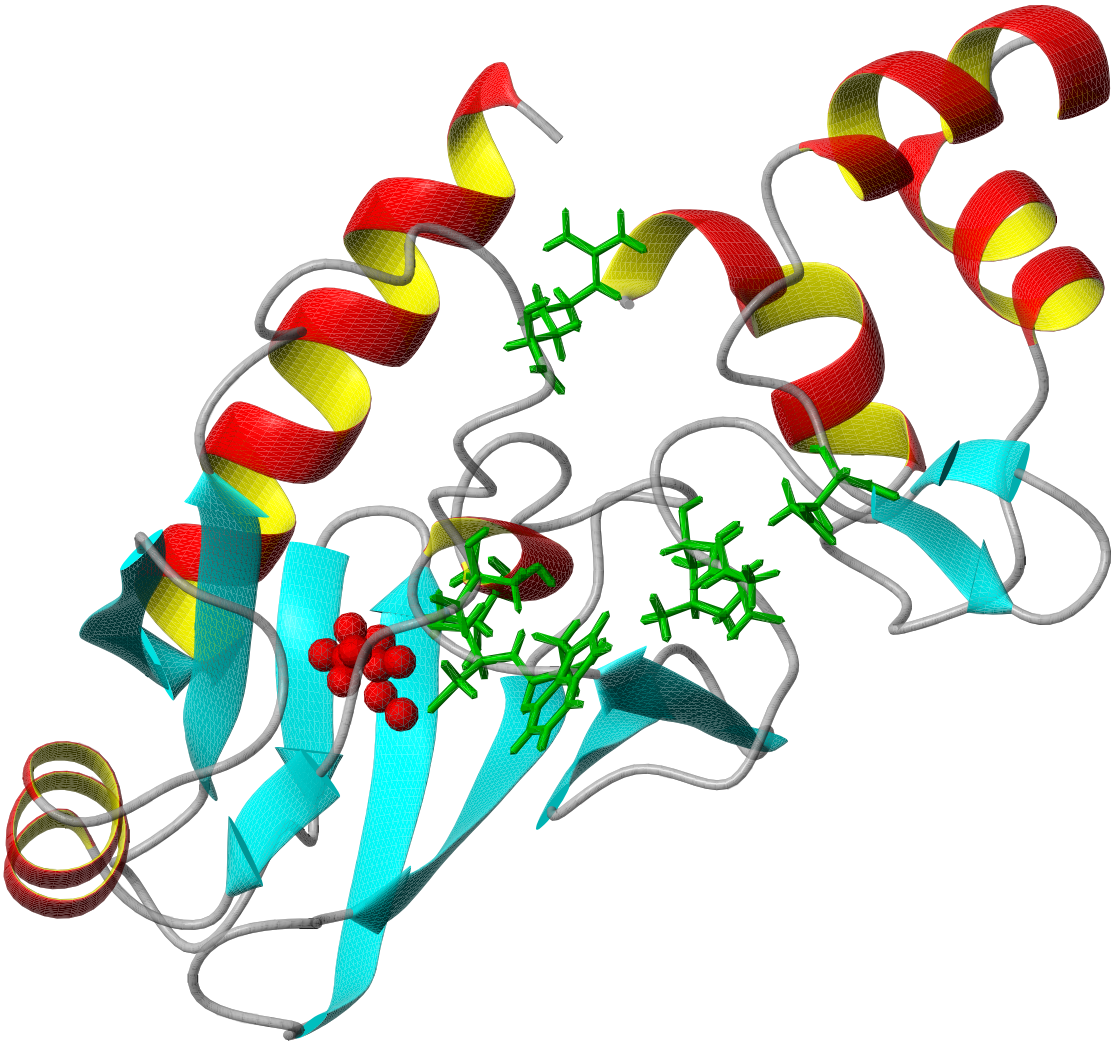

Figure 4.20: Ribbon diagram of MerB/Hg/DTT complex showing the DTT molecule (red) and the residues (green) which exhibit chemical shift perturbations upon exchange of (R,R)-DTT for (S,S)-DTT.

CHAPTER 5

CONCLUSIONS

5.1 COMPARISON OF FREE AND MERB/HG/DTT STRUCTURES

The difference in backbone chemical shift between the free MerB and MerB/Hg/DTT structures (Figure 2.8) predicts structural differences in two regions: around C96, and around C159/C160. A domain-by-domain comparison of the structures shows that the observed structural differences are consistent with the chemical shift differences.

The α-helical structure of the amino terminal domain is very similar between the free MerB protein and the MerB/Hg/DTT complex. When residues 26-71 of the free and MerB/Hg/DTT structures are aligned, the RMSD of the backbone atoms is 1.33 Å (see Figure 5.1). The largest differences are seen in the loop from residues 71-80 which connects the amino terminal and central domains. However, this difference may reflect the poorer quality of the data in this region, more than actual structural differences. The extent of assignments in this loop was lower than average for both forms, and there are not many long-range NOE restraints in this region.

In the core domain of the protein (composed of both the central and carboxyl terminal domains), the largest differences are in the unstructured regions and around C96, as expected. The remainder of the structure is similar between the two forms. If the loop regions consisting of residues 95-104, 147-161, and 178-184 are omitted, the RMSD for the backbone atoms is 2.01 Å. A large part of this difference was seen to be due to a translation of the carboxyl terminal helix between the two forms. This helix is poor in assignments and long-range NOE restraints in both forms, so this difference may only

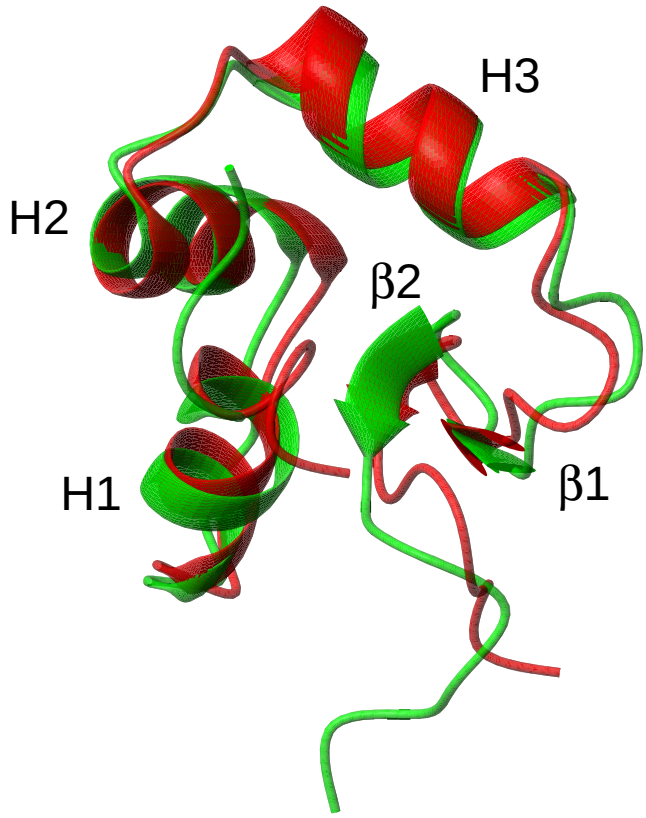

Figure 5.1: Ribbon diagram overlay of the lowest-energy free MerB structure (green) and the lowest-energy MerB/Hg/DTT structure (red) for the amino terminal domain. The RMSD of the backbone atoms is 1.33 Å.

reflect the accuracy of the data. If the carboxyl terminal helix is omitted, the RMSD of the backbone atoms between the two forms is 1.62 Å (Figure 5.2). Upon formation of the MerB/Hg/DTT complex, α-helix H4 comprising residues 97-103 adopts a more clearly helical conformation. Also, C96 shifts towards the interior of the protein.

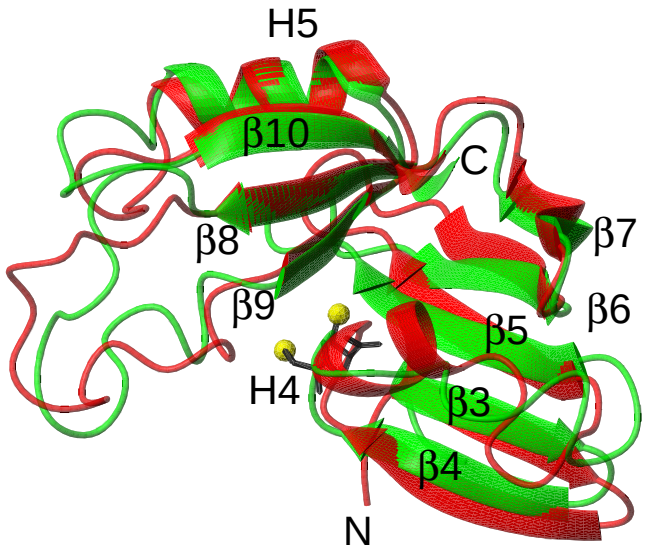

Figure 5.2: Ribbon diagram of the overlay of the lowest-energy MerB/Hg/DTT structure (red) and the lowest-energy free MerB structure (green) for residues 84-192. The RMSD of the backbone atoms, excluding the flexible loop regions and the carboxyl terminal α-helix H6 (see text), is 1.62 Å. The sulfur atom of C96 is shown in yellow.

5.2 MERCURIC RESISTANCE PROTEIN MECHANISMS

The recently solved MerB structure reveals some similarity between the arrangement of cysteine residues in MerA and MerB. Both proteins have a pair of adjacent cysteine residues which are exposed to solvent and located on a flexible portion of the molecule. In MerB, the flexible pair of cysteine residues is C159 and C160 located on the loop between strands β8 and β9. In MerA, the flexible pair of cysteines is C628/C629 on the carboxyl-terminal extension. In both MerA and MerB, the flexible cysteine pair is near in space to another “inner” cysteine residue (or pair of cysteine residues) which is distant in the sequence. In MerA, the inner cysteine pair is C207 / C212, and in MerB, the inner cysteine is C96.

The inner / outer cysteine arrangement is highly conserved in both MerA and MerB. Because MerA and MerB are quite dissimilar in both sequence and structure, it appears that both proteins arrived at this cysteine arrangement independently, which shows that the arrangement is particularly well suited to reactions involving mercurial substrates.

The outer cysteine pair C628 / C629 of MerA is involved in initial contact with the mercuric substrate. The structure of MerB, together with biochemical evidence, suggests that the outer cysteine pair C159 / C160 of MerB has a function similar to the outer cysteine pair of MerA. In both proteins, this outer cysteine pair occurs on a flexible, solvent exposed part of the molecule: In MerA, both the flexibility and solvent accessibility of the C628 / C629 outer cysteine pair was seen in the crystal structure [56]. The flexibility of C159 / C160 in MerB is demonstrated by ^{15}N relaxation data. Thiol modification experiments have identified C159 of MerB as the most solvent-exposed cysteine residue [48], and this was confirmed in the recently solved NMR structure.

The function of the outer cysteine pair in MerA, as demonstrated by single-turnover experiments, is to remove thiol ligands from the mercuric ion substrate [62]. Based on the structural similarity, the outer cysteine pair C159 / C160 in MerB may have the same function. Both MerA and MerB are capable of accepting substrates with a wide variety of thiol ligands, differing in size and charge. In both proteins, having a flexible outer cysteine pair which displaces exogenous thiol ligands may be what allows the wide substrate acceptance.

In the MerA mechanism, the mercuric ion is transferred from the outer cysteines to the inner cysteines where catalysis occurs. It has been suggested that this transfer is important for an alternating sites mechanism, in which the two active sites of the dimer alternate between a substrate-binding and a catalytic phase [60]. Because the inner and outer cysteine pairs are located on opposite monomers, a small change in interdomain orientation would allow a relatively large change in the distance between the inner and outer cysteine pairs. In MerB, a similar transfer of the mercuric ion may occur from C159 /

C160 to C96. In both the free MerB structure and the MerB/Hg/DTT structure, C159 is within 9 Å of C96. A small change in the conformation of the flexible C159 / C160 loop would be sufficient to bring C159 and C96 close enough for transfer of the mercuric ion. The MerB/Hg/DTT complex, in which the mercuric ion is bound to C96, forms after the transfer has taken place.

5.3 Implications for Phytoremediation

Initial attempts to use the MerA and MerB proteins for phytoremediation have shown that genetically engineered plants can indeed usefully express both MerA and MerB [37, 35]. This insertion of the target genes into the genetically engineered plants is the necessary first step in phytoremediation. However, further improvement in the engineered organisms could be achieved by consideration of details such as the localized expression of the transgenes, and the interaction of the new proteins with their non-native environment [10]. In the case of mercury resistance proteins and phytoremediation, one such detail to consider is the interaction between the proteins and phytochelatins.

In response to heavy metals, plants synthesize a series of multiple-sulfur-containing chelating compounds known as phytochelatins [165, 166]. The phytochelatins are similar in function to the metallothioneins present in animals [167], but metallothioneins are small gene-encoded proteins, whereas phytochelatins are synthesized from amino acids in a dedicated pathway [168]. Phytochelatins are ubiquitous in plants and form the principal initial response to heavy metals [169]. The phytochelatin synthesis pathway is rare outside of the plant kingdom, although a gene for a key step in phytochelatin synthesis has been identified in *C. elegans* [170].

Phytochelatins are synthesized from glutathione and normally contain 3-7 thiol groups [169, 171]. It has been shown that phytochelatins chelate ionic mercury in a 1:1 complex, and that phytochelatins easily outcompete monothiols such as glutathione (GSH) for

ionic mercury [172]. Therefore, in the presence of phytochelatins and organomercurial substrates, it is likely that MerB would form a MerB/Hg/phytochelatin complex similar to the MerB/Hg/DTT complex. It is clear from kinetic evidence and this structural study that small thiol molecule cofactors have a large influence on all steps of the mercury detoxification pathway. The effort to incorporate mercury resistance proteins into plants may benefit from a consideration of the interaction of phytochelatins with the mercury resistance proteins, especially MerB, because the presence of phytochelatins is one of the largest known differences between the plant cell environment and the native prokaryotic environment of the Mer proteins.

There are several avenues for the exploration of the interaction of phytochelatins with MerA and MerB. For *in vivo* experiments, it is possible to synthesize phytochelatins in large quantities [173]. These could be used in kinetic assays of MerA and MerB, and it may be possible to prepare a stable MerB/Hg/phytochelatin complex. If significant interactions were found, this would indicate that manipulation of the phytochelatin pathway in the modified plants would be a useful complement to the control of MerA and MerB expression in these plants. For example, if phytochelatins were found to significantly reduce transfer of mercuric ions from MerA to MerB *in vivo*, this would suggest that a reasonable strategy for increasing turnover in this pathway in plants would be to reduce the phytochelatin content of these plants. Total plant phytochelatin content could be manipulated by alterations in the phytochelatin synthesis pathway [168] or alterations in the synthesis pathway of the precursor GSH [171]. Such manipulations may prove equally important to the manipulation of the MerA and MerB proteins themselves for the creation of an effective phytoremediation system.

5.4 NMR AND STRUCTURE DETERMINATION

The structure of MerB demonstrates several advantages of NMR as a structure determination method. NMR may be preferred over X-Ray crystallography for structure determination of proteins with a significant proportion of disordered or flexible regions. In a recent comparison of X-Ray and NMR structures in the PDB, it was observed that NMR becomes the preferred method for proteins when over 5% of the structure is disordered [174]. In the case of MerB, the first 25 residues were not defined in the structure. The fact that these residues are not observed (or only weakly observed) in NMR spectra indicates that the disorder in the NMR structure probably reflects real disorder in this part of the protein, and not just the accuracy of the structure determination process. This amino terminal segment accounts for $\sim$ 12% of the sequence. If one includes the flexible loop containing C159 and C160 in the disordered regions of MerB, the extent of disorder rises to $\sim$ 17%, significantly higher than the 5% cutoff point where NMR becomes a preferred method. As with the amino terminal segment, the disorder in the C159 loop appears to be real mobility in the structure, and not just inaccuracy in the structure determination process. This is supported by the ^{15}N relaxation data (Figure 4.11).

For MerB, or other flexible proteins like it, one possible strategy for crystal structure determination would be to reduce the flexibility by eliminating problematic regions. In MerB, the two flexible regions are the amino terminal stretch and the C159 loop. The first 25 residues could be removed through mutagenesis. Removal of the C159 loop through mutagenesis would also be possible, although there are problems with this approach. By the kinetic evidence and analogy with MerA, it appears that the flexibility of the C159 loop is essential for the protein's function, so alteration of this region would impact the biological relevance of the resulting construct. Thus, it appears that, even if the amino terminal segment could be removed, the C159 loop would need to remain, resulting in a minimum of 5% unstructured region in the protein. A benefit of NMR is seen in that the

necessary presence of these disordered regions does not detract from the ability to obtain a precise structure of the remainder of the molecule.

5.5 Recommended Future Directions

5.5.1 Alternative MerB/Hg complexes

It would be interesting to obtain a mercury-containing MerB complex with a physiologically important thiol. Attempts to create MerB/Hg complexes with glutathione and cysteine did result in well-folded protein, but suffered from issues of homogeneity and reproducibility (Chapter 2). This is probably because these thiols promote turnover, so it is difficult to capture the enzyme in any one catalytic state. Although all known "physiological" thiols promote turnover [53], there are some small monothiols such as 2-aminoethanethiol which are similar to physiological thiols yet do not promote turnover. One of these non-turnover-promoting monothiols may form a stable complex with MerB, allowing a better characterization of the interaction with physiological thiols such as GSH. One interesting trend is that thiols which promote turnover tend to be charged, whereas those that do not promote turnover tend to be neutral, which would enhance their ability to fit into the binding pocket identified for DTT.

Another particularly useful sample would be a complex of MerA and MerB. If it is true that the carboxyl terminal cysteines of MerA behave similarly to the DTT molecule (Figure 3.3), then it is apparent that the difference between the two is that MerA is able to complete the process of complete removal of the mercuric ion, whereas DTT is not. MerA may have this capability due to its inner pair of active-site cysteine residues, which accept mercuric ions from the carboxyl terminal pair. If this is true, it may be possible to obtain a stable MerB/Hg/MerA complex by using a MerA peptide containing only the carboxyl terminal cysteine pair, or by using a full length mutant MerA which lacks the inner cysteine pair [62].

5.5.2 Other Channeling Evidence

In general, the conclusion of substrate channeling between an enzyme pair is stronger if more than one type of test for channeling can be applied. The known types of test are discussed in Chapter 1. For the proposed MerA/MerB interaction, some of the tests are complicated by the fact that MerA clearly can utilize Hg(II) not bound to protein in addition to MerB-bound Hg(II). For this reason the isotope dilution test may be inconclusive, because it depends on a preference by the E2 enzyme for E1-bound substrate (preference of MerB-bound Hg(II) by MerA in this case). Although such a preference clearly indicates channeling, it is not necessary for channeling. In the case of MerA and MerB, it seems likely that there would be no preference, because MerA has evolved to accept mercury both from MerB and from other sources. Perhaps a better alternative test for channeling would be the competing reaction test. The conclusion of the enzyme buffering test was that Hg(II) transfer from MerB to MerA preferentially occurs via direct transfer and not through solution. In the competing reaction test, some third molecule (a “reporter molecule”) would be present that was capable of detecting the intermediate mercuric ion in some way. One type of “reporter molecule” could be an enzyme inhibited by the mercuric ion. Due to the reactivity of Hg(II), such an enzyme should be easily found.

BIBLIOGRAPHY

[1] Ditri, P. A. and Ditri, F. M. (1978) Mercury contamination- human tragedy, *Environ. Manage. 2*, 3–16.

[2] Chang, L. W. (1979). Pathological effects of mercury poisoning, in *The Biogeochemistry of Mercury in the Environment* (Nriagu, J. O., Ed.) pp 519–580, Elsevier, New York.

[3] Nagashima, K. (1997) A review of experimental methylmercury toxicity in rats: Neuropathology and evidence for apoptosis, *Toxicol. Pathol. 25*, 624–631.

[4] Suzuki, T. (1979). Dose-Effect and Dose-Response Relationships of Mercury and its Derivatives, in *The Biogeochemistry of Mercury in the Environment* (Nriagu, J. O., Ed.) pp 399–422, Elsevier, New York.

[5] Kerper, L. E., Ballatori, N., and Clarkson, T. W. (1992) Methylmercury transport across the blood-brain barrier by an amino acid carrier, *Am. J. Physiol. 262*, R761–R765.

[6] Ou, Y. C., Thompson, S. A., Ponce, R. A., Schroeder, J., Kavanagh, T. J., and Faustman, E. M. (1999) Induction of the cell cycle regulatory gene p21 (Waf1, Cip1) following methylmercury exposure *in vitro* and *in vivo*, *Toxicol. Appl. Pharmacol. 157*, 203–212.

[7] Walsh, C. T., Distefano, M. D., Moore, M. J., Shewchuk, L. M., and Verdine, G. L. (1988) Molecular basis of bacterial resistance to organomercurial and inorganic mercuric salts, *FASEB J. 2*, 124–130.

[8] Lebel, J., Mergler, D., Branches, F., Lucotte, M., Amorim, M., Larribe, F., and Dolbec, J. (1998) Neurotoxic effects of low-level methylmercury contamination in the Amazonian basin, *Environ. Res. 79*, 20–32.

[9] Pak, K. R. and Bartha, R. (1998) Mercury methylation and demethylation in anoxic lake sediments and by strictly anaerobic bacteria, *Appl. Environ. Microbiol. 64*, 1013–1017.

[10] Meagher, R. B. (2000) Phytoremediation of toxic elemental and organic pollutants, *Curr. Opin. Plant Biol. 3*, 153–162.

[11] Barkay, T., Miller, S. M., and Summers, A. O. (2003) Bacterial mercury resistance from atoms to ecosystems, *FEMS Microbiology Reviews 27*, 355–384.

[12] Mason, R. P., Rolfhus, K. R., and Fitzgerald, W. F. (1995) Methylated and elemental mercury cycling in surface and deep ocean waters of the North Atlantic, *Water Air Soil Pollut. 80*, 665–677.

[13] Schroeder, W. H. and Munthe, J. (1998) Atmospheric mercury- an overview, *Atmos. Environ. 32*, 809–822.

[14] Mason, R. P., Fitzgerald, W. F., and Morel, F. M. M. (1994) The biogeochemical cycling of elemental mercury- anthropogenic influences, *Geochim. Cosmochim. Acta 58*, 3191–3198.

[15] Ikingura, J. R. and Akagi, H. (1999) Methylmercury production and distribution in aquatic systems, *Sci. Total Environ. 234*, 109–118.

[16] Mason, R. P., Reinfelder, J. R., and Morel, F. M. M. (1995) Bioaccumulation of mercury and methylmercury, *Water Air Soil Pollut. 80*, 915–921.

[17] Morel, F. M. M., Kraepiel, A. M. L., and Amyot, M. (1998) The chemical cycle and bioaccumulation of mercury, *Annu. Rev. Ecol. Syst. 29*, 543–566.

[18] Wood, J. M. (1974) Biological cycles for toxic elements in environment, *Science 183*, 1049–1052.

[19] Mason, R. P. and Sullivan, K. A. (1999) The distribution and speciation of mercury in the South and equatorial Atlantic, *Deep-Sea Res. Part II-Top. Stud. Oceanogr. 46*, 937–956.

[20] Choi, S. C. and Bartha, R. (1993) Cobalamin-mediated mercury methylation by *Desulfovibrio desulfuricans*, *Appl. Environ. Microbiol. 59*, 290–295.

[21] Jensen, S. and Jernelov, A. (1969) Biological methylation of mercury in aquatic organisms, *Nature 223*, 753.

[22] Fagerstrom, T. and Jernelov, A. (1971) Formation of methyl mercury from pure mercuric sulphide in aerobic organic sediment, *Water Res. 5*, 121.

[23] Bertilsson, L. and Neujahr, H. Y. (1971) Methylation of mercury compounds by methylcobalamin, *Biochemistry 10*, 2805.

[24] Choi, S. C., Chase, T., and Bartha, R. (1994) Metabolic pathways leading to mercury methylation in *Desulfovibrio desulfuricans*, *Appl. Environ. Microbiol. 60*, 4072–4077.

[25] Nriagu, J. O. (1993) Legacy of mercury pollution, *Nature 363*, 589–589.

[26] Joensuu, O. I. (1971) Fossil fuels as a source of mercury pollution, *Science 172*, 1027.

[27] Rodgers, D. W., Dickman, M., and Han, X. (1995) Stories from old reservoirs-sediment Hg and Hg methylation in Ontario hydroelectric developments, *Water Air Soil Pollut. 80*, 829–839.

[28] Choi, S. C. and Bartha, R. (1994) Environmental factors affecting mercury methylation in estuarine sediments, *Bull. Environ. Contam. Toxicol. 53*, 805–812.

[29] Mulligan, C. N., Yong, R. N., and Gibbs, B. F. (2001) Remediation technologies for metal-contaminated soils and groundwater: an evaluation, *Eng. Geol. 60*, 193–207.

[30] Moore, M. J., Distefano, M. D., Zydowsky, L. D., Cummings, R. T., and Walsh, C. T. (1990) Organomercurial lyase and mercuric ion reductase- Nature's mercury detoxification catalysts, *Accounts Chem. Res. 23*, 301–308.

[31] Summers, A. O. and Lewis, E. (1973) Volatilization of mercuric chloride by mercury-resistant plasmid-bearing strains of *Escherichia coli*, *Staphylococcus aureus*, and *Pseudomonas aeruginosa*, *J. Bacteriol. 113*, 1070–1072.

[32] Rugh, C. L., Senecoff, J. F., Meagher, R. B., and Merkle, S. A. (1998) Development of transgenic yellow poplar for mercury phytoremediation, *Nat. Biotechnol. 16*, 925–928.

[33] Wagner-dobler, I., Canstein, H., Li, Y., Timmis, K. N., and Deckwer, W. D. (2000) Removal of mercury from chemical wastewater by microoganisms in technical scale, *Environ. Sci. Technol. 34*, 4628–4634.

[34] Rugh, C. L. (2001) Mercury detoxification with transgenic plants and other biotechnological breakthroughs for phytoremediation, *In Vitro Cell. Dev. Biol.-Plant 37*, 321–325.

[35] Bizily, S. P., Rugh, C. L., and Meagher, R. B. (2000) Phytodetoxification of hazardous organomercurials by genetically engineered plants, *Nat. Biotechnol. 18*, 213–217.

[36] Rugh, C. L., Wilde, H. D., Stack, N. M., Thompson, D. M., Summers, A. O., and Meagher, R. B. (1996) Mercuric ion reduction and resistance in transgenic *Arabidopsis thaliana* plants expressing a modified bacterial *merA* gene, *Proc. Natl. Acad. Sci. U. S. A. 93*, 3182–3187.

[37] Bizily, S. P., Rugh, C. L., Summers, A. O., and Meagher, R. B. (1999) Phytoremediation of methylmercury pollution: *merB* expression in *Arabidopsis thaliana* confers resistance to organomercurials, *Proc. Natl. Acad. Sci. U. S. A. 96*, 6808–6813.

[38] Schottel, J., Mandal, A., Clark, D., and Silver, S. (1974) Volatilization of mercury and organomercurials determined by inducible R-factor systems in enteric bacteria, *Nature 251*, 335–337.

[39] Summers, A. O. (1986) Organization, expression, and evolution of genes for mercury resistance, *Annu. Rev. Microbiol. 40*, 607–634.

[40] Miller, S. M. (1999) Bacterial detoxification of Hg(II) and organomercurials, *Essays in Biochemistry 34*, 17–30.

[41] Summers, A. O. (1992) Untwist and shout- a heavy metal-responsive transcriptional regulator, *J. Bacteriol. 174*, 3097–3101.

[42] Kulkarni, R. D. and Summers, A. O. (1999) MerR cross-links to the α, β, and $\sigma(70)$ subunits of RNA polymerase in the preinitiation complex at the *mer*TPCAD promoter, *Biochemistry 38*, 3362–3368.

[43] Zeng, Q. D., Stalhandske, C., Anderson, M. C., Scott, R. A., and Summers, A. O. (1998) The core metal-recognition domain of MerR, *Biochemistry 37*, 15885–15895.

[44] Hamlett, N. V., Landale, E. C., Davis, B. H., and Summers, A. O. (1992) Roles of the Tn21 MerT, MerP, and MerC gene products in mercury resistance and mercury binding, *J. Bacteriol. 174*, 6377–6385.

[45] Steele, R. A. and Opella, S. J. (1997) Structures of the reduced and mercury-bound forms of MerP, the periplasmic protein from the bacterial mercury detoxification system, *Biochemistry 36*, 6885–6895.

[46] Nakahara, H., Silver, S., Miki, T., and Rownd, R. H. (1979) Hypersensitivity to Hg(II) and hyper-binding activity associated with cloned fragments of the mercurial resistance operon of plasmid NR1, *J. Bacteriol. 140*, 161–166.

[47] Begley, T. P., Walts, A. E., and Walsh, C. T. (1986) Mechanistic studies of a protonolytic organomercurial cleaving enzyme- bacterial organomercurial lyase, *Biochemistry 25*, 7192–7200.

[48] Pitts, K. E. and Summers, A. O. (2002) The roles of thiols in the bacterial organomercurial lyase (MerB), *Biochemistry 41*, 10287–10296.

[49] Kreevoy, M. M. and Kayser, W. V. (1966) Acid cleavage of allylmercuric iodide, *J. Am. Chem. Soc. 88*, 124.

[50] Sayre, L. M. and Jensen, F. R. (1979) Mechanism in electrophilic aliphatic substitution- kinetic and stereochemical study of bromodemercuration with bromide ion catalysis, *J. Am. Chem. Soc. 101*, 6001–6008.

[51] Gopinath, E. and Bruice, T. C. (1987) Assistance of protodemercuration by bis-thiol ligation and nucleophilic catalysis- a model study which relates to the organomercurial lyase reaction, *J. Am. Chem. Soc. 109*, 7903–7905.

[52] Barbaro, P., Cecconi, F., Ghilardi, A., Midollini, S., Orlandini, A., and Vacca, A. (1994) Metal coordination and Hg-C bond protonolysis in organomercury(II) compounds., *Inorg. Chem. 33*, 6163–6170.

[53] Begley, T. P., Walts, A. E., and Walsh, C. T. (1986) Bacterial organomercurial lyase-overproduction, isolation, and characterization, *Biochemistry 25*, 7186–7192.

[54] Petsko, G. A. (1991) Enzyme evolution- deja-vu all over again, *Nature 352*, 104–105.

[55] Fox, B. S. and Walsh, C. T. (1983) Mercuric reductase- homology to glutathione-reductase and lipoamide dehydrogenase- iodoacetamide alkylation and sequence of the active-site peptide, *Biochemistry 22*, 4082–4088.

[56] Schiering, N., Kabsch, W., Moore, M. J., Distefano, M. D., Walsh, C. T., and Pai, E. F. (1991) Structure of the detoxification catalyst mercuric ion reductase from *Bacillus sp.* strain RC607, *Nature 352*, 168–172.

[57] Brown, N. L., Ford, S. J., Pridmore, R. D., and Fritzinger, D. C. (1983) Nucleotide sequence of a gene from the *Pseudomonas* transposon Tn501 encoding mercuric reductase, *Biochemistry 22*, 4089–4095.

[58] Fox, B. and Walsh, C. T. (1982) Mercuric reductase- purification and characterization of a transposon-encoded flavoprotein containing an oxidation-reduction active disulfide, *J. Biol. Chem. 257*, 2498–2503.

[59] Rinderle, S. J., Booth, J. E., and Williams, J. W. (1983) Mercuric reductase from R-plasmid NR1- characterization and mechanistic study, *Biochemistry 22*, 869–876.

[60] Miller, S. M., Massey, V., Williams, C. H., Ballou, D. P., and Walsh, C. T. (1991) Communication between the active-sites in dimeric mercuric ion reductase- an alternating sites hypothesis for catalysis, *Biochemistry 30*, 2600–2612.

[61] Marshall, J. L., Booth, J. E., and Williams, J. W. (1984) Characterization of the covalent mercury(II)-NADPH complex, *J. Biol. Chem. 259*, 3033–3036.

[62] Engst, S. and Miller, S. M. (1999) Alternative routes for entry of HgX_2 into the active site of mercuric ion reductase depend on the nature of the X ligands, *Biochemistry 38*, 3519–3529.

[63] Engst, S. and Miller, S. M. (1998) Rapid reduction of Hg(II) by mercuric ion reductase does not require the conserved C-terminal cysteine pair using $HgBr_2$ as the substrate, *Biochemistry 37*, 11496–11507.

[64] Raybuck, S. A., Distefano, M. D., Teo, B. K., Ormejohnson, W., and Walsh, C. T. (1990) An EXAFS investigation of Hg(II) binding to mercuric reductase-comparative-analysis of the wild-type enzyme and a mutant enzyme generated by site-directed mutagenesis, *J. Am. Chem. Soc. 112*, 1983–1989.

[65] Brown, N. L., Camakaris, J., Lee, B. T. O., Williams, T., Morby, A. P., Parkhill, J., and Rouch, D. A. (1991) Bacterial resistances to mercury and copper, *J. Cell. Biochem. 46*, 106–114.

[66] Brown, N. L. (1985) Bacterial resistance to mercury- reductio ad absurdum, *Trends Biochem.Sci. 10*, 400–403.

[67] Moore, M. J. and Walsh, C. T. (1989) Mutagenesis of the N-terminal and C-terminal cysteine pairs of Tn501 mercuric ion reductase- consequences for bacterial detoxification of mercurials, *Biochemistry 28*, 1183–1194.

[68] Ovadi, J. (1991) Physiological significance of metabolic channeling, *J. Theor. Biol. 152*, 1–22.

[69] Srivastava, D. K. and Bernhard, S. A. (1986) Metabolite transfer via enzyme-enzyme complexes, *Science 234*, 1081–1086.

[70] Miles, E. W., Rhee, S., and Davies, D. R. (1999) The molecular basis of substrate channeling, *J. Biol. Chem. 274*, 12193–12196.

[71] Srere, P. A. (1987) Complexes of sequential metabolic enzymes, *Annu. Rev. Biochem. 56*, 89–124.

[72] Spivey, H. O. and Ovadi, J. (1999) Substrate channeling, *Methods 19*, 306–321.

[73] Negrutskii, B. S., Stapulionis, R., and Deutscher, M. P. (1994) Supramolecular organization of the mammalian translation system, *Proc. Natl. Acad. Sci. U. S. A. 91*, 964–968.

[74] Miziorko, H. M., Laib, F. E., and Behnke, C. E. (1990) Evidence for substrate channeling in the early steps of cholesterogenesis, *J. Biol. Chem. 265*, 9606–9609.

[75] Kis, K. and Bacher, A. (1995) Substrate channeling in the lumazine synthase-riboflavin synthase complex of *Bacillus subtilis*, *J. Biol. Chem. 270*, 16788–16795.

[76] Liang, P. H. and Anderson, K. S. (1998) Substrate channeling and domain-domain interactions in bifunctional thymidylate synthase-dihydrofolate reductase, *Biochemistry 37*, 12195–12205.

[77] Anderson, K. S., Miles, E. W., and Johnson, K. A. (1991) Serine modulates substrate channeling in tryptophan synthase- a novel intersubunit triggering mechanism, *J. Biol. Chem. 266*, 8020–8033.

[78] Bulock, K. G., Beardsley, G. P., and Anderson, K. S. (2002) The kinetic mechanism of the human bifunctional enzyme ATIC (5-amino-4-imidazolecarboxamide ribonucleotide transformylase/inosine 5’-monophosphate cyclohydrolase)- a surprising lack of substrate channeling, *J. Biol. Chem. 277*, 22168–22174.

[79] Schlichting, I., Yang, X. J., Miles, E. W., Kim, A. Y., and Anderson, K. S. (1994) Structural and kinetic-analysis of a channel-impaired mutant of tryptophan synthase, *J. Biol. Chem. 269*, 26591–26593.

[80] Morgunov, I. and Srere, P. A. (1998) Interaction between citrate synthase and malate dehydrogenase- substrate channeling of oxaloacetate, *J. Biol. Chem. 273*, 29540–29544.

[81] Srivastava, D. K. and Bernhard, S. A. (1984) Direct transfer of reduced nicotinamide adenine-dinucleotide from glyceraldehyde-3-phosphate dehydrogenase to liver alcohol dehydrogenase, *Biochemistry 23*, 4538–4545.

[82] Fukushima, T., Decker, R. V., Anderson, W. M., and Spivey, H. O. (1989) Substrate channeling of NADH and binding of dehydrogenases to complex I, *J. Biol. Chem. 264*, 16483–16488.

[83] Ushiroyama, T., Fukushima, T., Styre, J. D., and Spivey, H. O. (1992) Substrate channeling of NADH in mitochondrial redox processes, *Curr. Top. Cell. Regul. 33*, 291–307.

[84] Chock, P. B. and Gutfreund, H. (1988) Reexamination of the kinetics of the transfer of NADH between its complexes with glycerol-3-phosphate dehydrogenase and with lactate dehydrogenase, *Proc. Natl. Acad. Sci. U. S. A. 85*, 8870–8874.

[85] Aris, W. M. and Pettersson, G. (1997) Mechanism of NADH transfer between alcohol dehydrogenase and glyceraldehyde-3-phosphate dehydrogenase, *Eur. J. Biochem. 250*, 158–162.

[86] Wu, X. M., Gutfreund, H., Lakatos, S., and Chock, P. B. (1991) Substrate channeling in glycolysis- a phantom phenomenon, *Proc. Natl. Acad. Sci. U. S. A. 88*, 497–501.

[87] Geck, M. K. and Kirsch, J. F. (1999) A novel, definitive test for substrate channeling illustrated with the aspartate aminotransferase-malate dehydrogenase system, *Biochemistry 38*, 8032–8037.

[88] James, C. L. and Viola, R. E. (2002) Production and characterization of bifunctional enzymes. Substrate channeling in the aspartate pathway, *Biochemistry 41*, 3726–3731.

[89] Holden, H. M., Thoden, J. B., and Raushel, F. M. (1998) Carbamoyl phosphate synthetase: a tunnel runs through it, *Curr. Opin. Struct. Biol. 8*, 679–685.

[90] Wallis, N. G., Allen, M. D., Broadhurst, R. W., Lessard, I. A. D., and Perham, R. N. (1996) Recognition of a surface loop of the lipoyl domain underlies substrate channelling in the pyruvate dehydrogenase multienzyme complex, *J. Mol. Biol. 263*, 463–474.

[91] Malhotra, O. P., Prabhakar, P., Sengupta, T., and Kayastha, A. M. (1995) Phosphoglycerate-kinase glyceraldehyde-3-phosphate-dehydrogenase interaction-molecular mass studies, *Eur. J. Biochem. 227*, 556–562.

[92] Brooks, S. P. J. and Storey, K. B. (1991) The effect of enzyme-enzyme complexes on the overall glycolytic rate *in vivo*, *Biochemistry international 25*, 477–489.

[93] Olsson, U., Billberg, A., Sjovall, S., Al-karadaghi, S., and Hansson, M. (2002) *In vivo* and *in vitro* studies of *Bacillus subtilis* ferrochelatase mutants suggest substrate channeling in the heme biosynthesis pathway, *J. Bacteriol. 184*, 4018–4024.

[94] Williams, C. H., Stillman, T. J., Barynin, V. V., Sedelnikova, S. E., Tang, Y., Green, J., Guest, J. R., and Artymiuk, P. J. (2002) *E. coli* aconitase B structure reveals a HEAT-like domain with implications for protein-protein recognition, *Nature Struct. Biol. 9*, 447–452.

[95] Elcock, A. H. (2002) Atomistic simulations of competition between substrates binding to an enzyme, *Biophys. J. 82*, 2326–2332.

[96] Nilges, M., Clore, G. M., and Gronenborn, A. M. (1988) Determination of 3-dimensional structures of proteins from interproton distance data by dynamical simulated annealing from a random array of atoms- circumventing problems associated with folding, *FEBS Lett. 239*, 129–136.

[97] Ikura, M., Kay, L. E., and Bax, A. (1990) A novel approach for sequential assignment of ^{1}H, ^{13}C, and ^{15}N spectra of larger proteins- heteronuclear triple-resonance 3-dimensional NMR spectroscopy- application to calmodulin, *Biochemistry 29*, 4659–4667.

[98] Grzesiek, S. and Bax, A. (1992) Correlating backbone amide and side-chain resonances in larger proteins by multiple relayed triple resonance NMR, *J. Am. Chem. Soc. 114*, 6291–6293.

[99] Kay, L. E., Ikura, M., Tschudin, R., and Bax, A. (1990) 3-dimensional triple-resonance NMR spectroscopy of isotopically enriched proteins, *J. Magn. Reson. 89*, 496–514.

[100] Yamazaki, T., Yoshida, M., and Nagayama, K. (1993) Complete assignments of magnetic resonances of ribonuclease H from *Escherichia coli* by double-resonance and triple-resonance 2D and 3D NMR spectroscopies, *Biochemistry 32*, 5656–5669.

[101] Clore, G. M. and Gronenborn, A. M. (1991) Structures of larger proteins in solution- 3-dimensional and 4-dimensional heteronuclear NMR spectroscopy, *Science 252*, 1390–1399.

[102] Clore, G. M., Robien, M. A., and Gronenborn, A. M. (1993) Exploring the limits of precision and accuracy of protein structures determined by Nuclear Magnetic Resonance spectroscopy, *J. Mol. Biol. 231*, 82–102.

[103] Wagner, G. (1997) An account of NMR in structural biology, *Nature Struct. Biol. 4*, 841–844.

[104] Gardner, K. H. and Kay, L. E. (1998) The use of ^{2}H, ^{13}C, ^{15}N multidimensional NMR to study the structure and dynamics of proteins, *Annu. Rev. Biophys. Biomolec. Struct. 27*, 357–406.

[105] Kay, L. E. and Gardner, K. H. (1997) Solution NMR spectroscopy beyond 25 kDa, *Curr. Opin. Struct. Biol. 7*, 722–731.

[106] Yamazaki, T., Lee, W., Revington, M., Mattiello, D. L., Dahlquist, F. W., Arrowsmith, C. H., and Kay, L. E. (1994) An HNCA pulse scheme for the backbone assignment of ^{15}N,^{13}C,^{2}H-labeled proteins- application to a 37-kDa Trp repressor DNA complex, *J. Am. Chem. Soc. 116*, 6464–6465.

[107] Yamazaki, T., Lee, W., Arrowsmith, C. H., Muhandiram, D. R., and Kay, L. E. (1994) A suite of triple-resonance NMR experiments for the backbone assignment of ^{15}N, ^{13}C, ^{2}H labeled proteins with high sensitivity, *J. Am. Chem. Soc. 116*, 11655–11666.

[108] Nietlispach, D., Clowes, R. T., Broadhurst, R. W., Ito, Y., Keeler, J., Kelly, M., Ashurst, J., Oschkinat, H., Domaille, P. J., and Laue, E. D. (1996) An approach to the structure determination of larger proteins using triple resonance NMR experiments in conjunction with random fractional deuteration, *J. Am. Chem. Soc. 118*, 407–415.

[109] Lin, Y. X. and Wagner, G. (1999) Efficient side-chain and backbone assignment in large proteins: Application to tGCN5, *J. Biomol. NMR 15*, 227–239.

[110] Prestegard, J. H. (1998) New techniques in structural NMR- anisotropic interactions, *Nature Struct. Biol. 5*, 517–522.

[111] Bax, A., Kontaxis, G., and Tjandra, N. (2001) Dipolar couplings in macromolecular structure determination, *Methods Enzymol. 339*, 127–174.

[112] Clore, G. M. and Schwieters, C. D. (2002) Theoretical and computational advances in biomolecular NMR spectroscopy, *Curr. Opin. Struct. Biol. 12*, 146–153.

[113] Prestegard, J. H. and Kishore, A. I. (2001) Partial alignment of biomolecules: an aid to NMR characterization, *Curr. Opin. Chem. Biol. 5*, 584–590.

[114] Kanelis, V., Forman-Kay, J. D., and Kay, L. E. (2001) Multidimensional NMR methods for protein structure determination, *IUBMB Life 52*, 291–302.

[115] Tjandra, N., Omichinski, J. G., Gronenborn, A. M., Clore, G. M., and Bax, A. (1997) Use of dipolar ^{1}H-^{15}N and ^{1}H-^{13}C couplings in the structure determination of magnetically oriented macromolecules in solution, *Nature Struct. Biol. 4*, 732–738.

[116] Fowler, C. A., Tian, F., Al-Hashimi, H. M., and Prestegard, J. H. (2000) Rapid determination of protein folds using residual dipolar couplings, *J. Mol. Biol. 304*, 447–460.

[117] Amor, J. C., Seidel, R. D., Tian, F., Kahn, R. A., and Prestegard, J. H. (2002) Letter to the editor: ^{1}H, ^{15}N and ^{13}C assignments of full length human ADP Ribosylation Factor 1 (ARF1) using triple resonance connectivities and dipolar couplings, *J. Biomol. NMR 23*, 253–254.

[118] Ogawa, H. I., Tolle, C. L., and Summers, A. O. (1984) Physical and genetic map of the organomercury resistance (omr) and inorganic mercury resistance (hgr) loci of the IncM plasmid R831B, *Gene 32*, 311–320.

[119] Kay, L. E., Keifer, P., and Saarinen, T. (1992) Pure absorption gradient enhanced heteronuclear single quantum correlation spectroscopy with improved sensitivity, *J. Am. Chem. Soc. 114*, 10663–10665.

[120] Delaglio, F., Grzesiek, S., Vuister, G. W., Zhu, G., Pfeifer, J., and Bax, A. (1995) NMRPipe- a multidimensional spectral processing system based on Unix pipes, *J. Biomol. NMR 6*, 277–293.

[121] Scott, R. A. (2000). X-Ray Absorption Spectroscopy, in *Physical Methods in Bioinorganic Chemistry. Spectroscopy and Magnetism* (Que, L., Ed.) pp 465–503, University Science Books, Sausalito, CA.

[122] Muhandiram, D. R. and Kay, L. E. (1994) Gradient-enhanced triple-resonance 3-dimensional NMR experiments with improved sensitivity, *J. Magn. Reson. Ser. B 103*, 203–216.

[123] Kay, L. E., Xu, G. Y., and Yamazaki, T. (1994) Enhanced-sensitivity triple-resonance spectroscopy with minimal H_2O saturation, *J. Magn. Reson. Ser. A 109*, 129–133.

[124] Logan, T. M., Olejniczak, E. T., Xu, R. X., and Fesik, S. W. (1993) A general method for assigning NMR spectra of denatured proteins using 3D HC(CO)NH-TOCSY triple resonance experiments, *J. Biomol. NMR 3*, 225–231.

[125] Grzesiek, S., Anglister, J., and Bax, A. (1993) Correlation of backbone amide and aliphatic side-chain resonances in $^{13}C/^{15}N$-enriched proteins by isotropic mixing of ^{13}C magnetization, *J. Magn. Reson. Ser. B 101*, 114–119.

[126] Emerson, S. D. and Montelione, G. T. (1992) Accurate measurements of proton scalar coupling-constants using ^{13}C isotropic mixing spectroscopy, *J. Am. Chem. Soc. 114*, 354–356.

[127] Shaka, A. J., Keeler, J., Frenkiel, T., and Freeman, R. (1983) An improved sequence for broad-band decoupling- WALTZ-16, *Journal of Magnetic Resonance 52*, 335–338.

[128] Utschig, L. M., Wright, J. G., and O'Halloran, T. V. (1993) Biochemical and spectroscopic probes of mercury(II) coordination environments in proteins, *Methods Enzymol. 226*, 71–97.

[129] Farmer, B. T. (1996) Localizing the NADP(+) binding site on the MurB enzyme by NMR, *Nature Struct. Biol. 3*, 995–997.

[130] Sharma, D. and Rajarathnam, K. (2000) ^{13}C NMR chemical shifts can predict disulfide bond formation, *J. Biomol. NMR 18*, 165–171.

[131] Cheesman, B. V., Arnold, A. P., and Rabenstein, D. L. (1988) Nuclear magnetic resonance studies of the solution chemistry of metal complexes. Hg(thiol)$_3$ complexes and Hg(II)-thiol ligand exchange kinetics, *J. Am. Chem. Soc. 110*, 6359–6364.

[132] Gutfreund, H. and Chock, P. B. (1991) Substrate channeling among glycolytic-enzymes- fact or fiction, *J. Theor. Biol. 152*, 117–121.

[133] Spivey, H. O. (1991) Evidence of NADH channeling between dehydrogenases, *J. Theor. Biol. 152*, 103–107.

[134] Di Lello, P., Benison, G. C., Legault, P., Summers, A. O., and Omichinski, J. G. (2004) NMR structural studies reveal a novel protein fold for MerB, the organomercurial lyase involved in the bacterial mercury resistance system. In preparation.

[135] Ikura, M., Spera, S., Barbato, G., Kay, L. E., Krinks, M., and Bax, A. (1991) Secondary structure and side-chain ^{1}H and ^{13}C resonance assignments of calmodulin in solution by heteronuclear multidimensional NMR spectroscopy, *Biochemistry 30*, 9216–9228.

[136] Kay, L. E., Xu, G. Y., Singer, A. U., Muhandiram, D. R., and Forman-Kay, J. D. (1993) A gradient-enhanced HCCH-TOCSY experiment for recording side-chain ^{1}H and ^{13}C correlations in H_2O samples of proteins, *J. Magn. Reson. Ser. B 101*, 333–337.

[137] Vuister, G. W. and Bax, A. (1992) Resolution enhancement and spectral editing of uniformly ^{13}C- enriched proteins by homonuclear broad-band ^{13}C decoupling, *J. Magn. Reson. 98*, 428–435.

[138] Zhu, G. and Bax, A. (1990) Improved linear prediction for truncated signals of known phase, *Journal of Magnetic Resonance 90*, 405–410.

[139] Zhu, G. and Bax, A. (1992) Improved linear prediction of damped NMR signals using modified forward backward linear prediction, *J. Magn. Reson. 100*, 202–207.

[140] Zhu, G. A. and Bax, A. (1992) 2-dimensional linear prediction for signals truncated in both dimensions, *J. Magn. Reson. 98*, 192–199.

[141] Zhang, O. W., Kay, L. E., Olivier, J. P., and Forman-Kay, J. D. (1994) Backbone ^{1}H and ^{15}N resonance assignments of the N-terminal SH3 domain of *drk* in folded and unfolded states using enhanced-sensitivity pulsed-field gradient NMR techniques, *J. Biomol. NMR 4*, 845–858.

[142] Zuiderweg, E. R. P., Mcintosh, L. P., Dahlquist, F. W., and Fesik, S. W. (1990) 3-dimensional ^{13}C-resolved proton NOE spectroscopy of uniformly ^{13}C-labeled

proteins for the NMR assignment and structure determination of larger molecules, *J. Magn. Reson. 86*, 210–216.

[143] Hansen, M. R., Mueller, L., and Pardi, A. (1998) Tunable alignment of macromolecules by filamentous phage yields dipolar coupling interactions, *Nature Struct. Biol. 5*, 1065–1074.

[144] Yang, D. W., Venters, R. A., Mueller, G. A., Choy, W. Y., and Kay, L. E. (1999) TROSY-based HNCO pulse sequences for the measurement of (HN)-^{1}H-^{15}N, ^{15}N-(CO)-^{13}C, (HN)-^{1}H-(CO)-^{13}C, (CO)-^{13}C-^{13}C$_{\alpha}$ and (HN)-^{1}H-^{13}C$_{\alpha}$ dipolar couplings in ^{15}N, ^{13}C, ^{2}H-labeled proteins, *J. Biomol. NMR 14*, 333–343.

[145] Cornilescu, G., Delaglio, F., and Bax, A. (1999) Protein backbone angle restraints from searching a database for chemical shift and sequence homology, *J. Biomol. NMR 13*, 289–302.

[146] Farrow, N. A., Muhandiram, R., Singer, A. U., Pascal, S. M., Kay, C. M., Gish, G., Shoelson, S. E., Pawson, T., Forman-Kay, J. D., and Kay, L. E. (1994) Backbone dynamics of a free and a phosphopeptide-complexed *src* homology-2 domain studied by ^{15}N NMR relaxation, *Biochemistry 33*, 5984–6003.

[147] Zwahlen, C., Legault, P., Vincent, S. J. F., Greenblatt, J., Konrat, R., and Kay, L. E. (1997) Methods for measurement of intermolecular NOEs by multinuclear NMR spectroscopy: Application to a bacteriophage lambda N-peptide/boxB RNA complex, *J. Am. Chem. Soc. 119*, 6711–6721.

[148] Ogura, K., Terasawa, H., and Inagaki, F. (1996) An improved double-tuned and isotope-filtered pulse scheme based on a pulsed field gradient and a wide-band inversion shaped pulse, *J. Biomol. NMR 8*, 492–498.

[149] Piotto, M., Saudek, V., and Sklenar, V. (1992) Gradient tailored excitation for single quantum NMR spectroscopy of aqueous solutions, *J. Biomol. NMR 2*, 661–665.

[150] Grzesiek, S., Anglister, J., Ren, H., and Bax, A. (1993) ^{13}C line narrowing by ^{2}H decoupling in $^{2}H/^{13}C/^{15}N$-enriched proteins- application to triple-resonance 4D J-connectivity of sequential amides, *J. Am. Chem. Soc. 115*, 4369–4370.

[151] Matsuo, H., Li, H. J., and Wagner, G. (1996) A sensitive HN(CA)CO experiment for deuterated proteins, *J. Magn. Reson. Ser. B 110*, 112–115.

[152] Sternberg, M. J. E. and Thornton, J. M. (1977) Conformation of proteins- handedness of connection between parallel β-strands, *J. Mol. Biol. 110*, 269–283.

[153] Brunger, A. T., Adams, P. D., Clore, G. M., Delano, W. L., Gros, P., Grosse-kunstleve, R. W., Jiang, J. S., Kuszewski, J., Nilges, M., Pannu, N. S., Read, R. J., Rice, L. M., Simonson, T., and Warren, G. L. (1998) Crystallography & NMR system: A new software suite for macromolecular structure determination, *Acta Crystallogr. Sect. D-Biol. Crystallogr. 54*, 905–921.

[154] Stein, E. G., Rice, L. M., and Brunger, A. T. (1997) Torsion-angle molecular dynamics as a new efficient tool for NMR structure calculation, *J. Magn. Reson. 124*, 154–164.

[155] Choy, W. Y., Tollinger, M., Mueller, G. A., and Kay, L. E. (2001) Direct structure refinement of high molecular weight proteins against residual dipolar couplings and carbonyl chemical shift changes upon alignment: an application to maltose binding protein, *J. Biomol. NMR 21*, 31–40.

[156] Losonczi, J. A., Andrec, M., Fischer, M. W. F., and Prestegard, J. H. (1999) Order matrix analysis of residual dipolar couplings using singular value decomposition, *J. Magn. Reson. 138*, 334–342.

[157] Laskowski, R. A., Macarthur, M. W., Moss, D. S., and Thornton, J. M. (1993) PROCHECK - A program to check the stereochemical quality of protein structures, *J. Appl. Crystallogr. 26*, 283–291.

[158] Koradi, R., Billeter, M., and Wuthrich, K. (1996) MOLMOL: A program for display and analysis of macromolecular structures, *J. Mol. Graph. 14*, 51–52.

[159] Altschul, S. F., Madden, T. L., Schaffer, A. A., Zhang, J. H., Zhang, Z., Miller, W., and Lipman, D. J. (1997) Gapped BLAST and PSI-BLAST: a new generation of protein database search programs, *Nucleic Acids Res. 25*, 3389–3402.

[160] Jones, D. T. (1999) Genthreader: An efficient and reliable protein fold recognition method for genomic sequences, *J. Mol. Biol. 287*, 797–815.

[161] Chou, P. Y. and Fasman, G. D. (1977) β turns in proteins, *J. Mol. Biol. 115*, 135–175.

[162] Chou, K. C. and Blinn, J. R. (1997) Classification and prediction of β-turn types, *J. Protein Chem. 16*, 575–595.

[163] Aurora, R. and Rose, G. D. (1998) Helix capping, *Protein Sci. 7*, 21–38.

[164] Tolman, J. R., Al-Hashimi, H. M., Kay, L. E., and Prestegard, J. H. (2001) Structural and dynamic analysis of residual dipolar coupling data for proteins, *J. Am. Chem. Soc. 123*, 1416–1424.

[165] Gupta, S. C. and Goldsbrough, P. B. (1991) Phytochelatin accumulation and cadmium tolerance in selected tomato cell-lines, *Plant Physiol. 97*, 306–312.

[166] Steffens, J. C. (1990) The heavy-metal binding peptides of plants, *Annu. Rev. Plant Physiol. Plant Molec. Biol. 41*, 553–575.

[167] Furey, W. F., Robbins, A. H., Clancy, L. L., Winge, D. R., Wang, B. C., and Stout, C. D. (1986) Crystal structure of Cd, Zn metallothionein, *Science 231*, 704–710.

[168] Chen, J. J., Zhou, J. M., and Goldsbrough, P. B. (1997) Characterization of phytochelatin synthase from tomato, *Physiol. Plant. 101*, 165–172.

[169] Grill, E., Winnacker, E. L., and Zenk, M. H. (1985) Phytochelatins- the principal heavy-metal complexing peptides of higher plants, *Science 230*, 674–676.

[170] Clemens, S., Schroeder, J. I., and Degenkolb, T. (2001) *Caenorhabditis elegans* expresses a functional phytochelatin synthase, *Eur. J. Biochem. 268*, 3640–3643.

[171] Mendum, M. L., Gupta, S. C., and Goldsbrough, P. B. (1990) Effect of glutathione on phytochelatin synthesis in tomato cells, *Plant Physiol. 93*, 484–488.

[172] Mehra, R. K., Miclat, J., Kodati, V. R., Abdullah, R., Hunter, T. C., and Mulchandani, P. (1996) Optical spectroscopic and reverse-phase HPLC analyses of Hg(II) binding to phytochelatins, *Biochem. J. 314*, 73–82.

[173] Friederich, M., Kneer, R., and Zenk, M. H. (1998) Enzymic synthesis of phytochelatins in gram quantities, *Phytochemistry 49*, 2323–2329.

[174] Prestegard, J. H., Valafar, H., Glushka, J., and Tian, F. (2001) Nuclear magnetic resonance in the era of structural genomics, *Biochemistry 40*, 8677–8685.

APPENDIX A

NMR EXPERIMENTS PERFORMED ON MERB/HG/DTT COMPLEX

Table A.1: NMR experiments for MerB/Hg/DTT structure determination.

			np_i^a	np_f^b	sw / Hz	dr^c / ppm
3D ^{13}C-edited HMQC-NOESY^d	^{1}H	f3	560	2048	10000	0.022
	^{1}H	f1	128	256	5599	0.055
	^{13}C	f2	50	256	7066	0.703
HNCACB	^{1}H	f3	512	2048	8000	0.026
	^{13}C	f1	50	256	9199	1.220
	^{15}N	f2	42	128	2000	0.783
HNCO	^{1}H	f3	512	2048	8000	0.026
	^{13}C	f1	90	256	1849	0.136
	^{15}N	f2	42	128	2000	0.783
HBCBCACONNH	^{1}H	f3	512	2048	8000	0.026
	^{13}C	f1	50	256	9199	1.220
	^{15}N	f2	42	128	2000	0.783

C(CC)TOCSY-NNH	^{1}H	f3	512	2048	8000	0.026
	^{13}C	f1	64	256	9199	0.953
	^{15}N	f2	42	128	2000	0.783
H(CC)TOCSY-NNH	^{1}H	f3	512	2048	8000	0.026
	^{1}H	f1	64	256	4100	0.107
	^{15}N	f2	42	128	2000	0.783
^{13}C/^{15}N-edited NOESY-HSQC	^{1}H	f3	427	2048	8000	0.031
	^{13}C	f1	146	512	7000	0.318
	^{15}N	f2	32	128	3600	1.851
^{15}N-edited NOESY-HSQC	^{1}H	f3	512	2048	8000	0.026
	^{1}H	f1	100	256	7199	0.120
	^{15}N	f2	60	128	2000	0.548
HCCH-COSY	^{1}H	f3	512	2048	8000	0.026
	^{1}H	f1	70	256	4100	0.098
	^{13}C	f2	40	256	5300	0.879
HCCH-TOCSY	^{1}H	f3	512	2048	8000	0.026
	^{1}H	f1	70	256	4100	0.098
	^{13}C	f2	40	256	5300	0.879

HNHA	^{1}H	f3	512	2048	8000	0.026
	^{1}H	f1	72	256	7099	0.164
	^{15}N	f2	50	128	2000	0.658
F_1-(^{13}C)filtered, F_3-(^{13}C)edited NOESY-HSQC	^{1}H	f3	382	2048	7499	0.033
	^{1}H	f1	116	256	4199	0.060
	^{13}C	f2	40	256	4200	0.696
TROSY-HNCO-COCA	^{1}H	f3	1024	4096	8000	0.013
	^{13}C	f1	72	256	1600	0.147
	^{15}N	f2	42	128	1700	0.666
TROSY-HNCO-HN	^{1}H	f3	1024	4096	8000	0.013
	^{13}C	f1	36	256	1600	0.295
	^{15}N	f2	41	128	1700	0.682
TROSY-HNCO-NCO	^{1}H	f3	1024	4096	8000	0.013
	^{13}C	f1	36	256	1600	0.295
	^{15}N	f2	48	128	1700	0.583
^{15}N-edited DIPSI-HSQC	^{1}H	f3	512	2048	8000	0.026
	^{1}H	f1	140	256	7099	0.085
	^{15}N	f2	42	128	2000	0.783

[a] np_i is the number of acquired complex points before any processing.

[b] np_f is the number of complex points after linear prediction and zero filling.

[c] dr_f is the digital resolution.

[d] recorded at a field of 800 MHz.

APPENDIX B

CHANGES IN ASYMMETRY DUE TO DOMAIN MOTION

In this section it will be shown that the difference in rhombicity observed between the amino terminal domain and the remainder of the protein can be explained by a wobbling motion of the domains about the Z axis of the principal alignment frame.

For an internuclear vector $\vec{v}$ the observed residual dipolar coupling is related to the orientation by [111]:

$$D_v \propto \left\langle 3cos^2\theta - 1 \right\rangle \tag{B.1}$$

where θ is the angle between $\vec{v}$ and the magnetic field and angle brackets denote an average over time.

The angle θ between the internuclear vector and the magnetic field can be broken down into its components in a Cartesian frame, so that:

$$D_v \propto \left\langle 3(B_x \cdot v_x + B_y \cdot v_y + B_z \cdot v_z)^2 - 1 \right\rangle \tag{B.2}$$

where B_x represents the cosine of the angle between the magnetic field and the x axis of the Cartesian frame and v_x represents the cosine of the angle between the internuclear vector and the Cartesian frame; similar terms exist for the other two axes.

We now introduce the key modification to the above theory: Assume that the vector $\vec{v'}$ represents the equilibrium position of the internuclear vector in the Cartesian frame. The actual position of the internuclear vector $\vec{v}$ is related to the equilibrium position $\vec{v'}$ by a rotation through the angle ϕ about the Z axis, so we have:

$$D_v \propto \left\langle 3\left(B_x \cdot (v'_x cos\phi + v'_y sin\phi) + B_y \cdot (-v'_x sin\phi + v'_y cos\phi) + B_z \cdot v_z\right)^2 - 1 \right\rangle \tag{B.3}$$

Let us assume that the Cartesian frame corresponds to the principal alignment frame so that cross terms such as $\langle B_x \cdot B_y \rangle$ vanish:

$$\begin{aligned} D_v &\propto 3\left(\left\langle B_x^2 (v'_x cos\phi + v'_y sin\phi)^2 \right\rangle + \right. \\ &\quad \left. \left\langle B_y^2 (-v'_x sin\phi + v'_y cos\phi)^2 \right\rangle + \left\langle B_z^2 \right\rangle v_z^2 \right) - 1 \end{aligned} \tag{B.4}$$

Further, the overall orientation of the molecule is not correlated to the instantaneous wobbling position as given by ϕ. Therefore, equalities such as $\left\langle B_x^2 sin^2\phi \right\rangle = \left\langle B_x^2 \right\rangle \left\langle sin^2\phi \right\rangle$ hold. This allows the following simplification of (B.4):

$$\begin{aligned} D_v &\propto 3\left(\left\langle B_x^2 \right\rangle \left\langle (v'_x cos\phi + v'_y sin\phi)^2 \right\rangle + \right. \\ &\quad \left. \left\langle B_y^2 \right\rangle \left\langle (-v'_x sin\phi + v'_y cos\phi)^2 \right\rangle + \left\langle B_z^2 \right\rangle v_z^2 \right) - 1 \end{aligned} \tag{B.5}$$

If we assume that the probability distribution of ϕ is an even function (i.e. leftwards and rightwards wobbles are of equal liklihood), then terms such as $\langle sin\phi \cdot cos\phi \rangle$ vanish, and (B.5) becomes:

$$\begin{aligned} D_v &\propto 3\left(\left\langle B_x^2 \right\rangle \left({v'_x}^2 \left\langle cos^2\phi \right\rangle + {v'_y}^2 \left\langle sin^2\phi \right\rangle \right) + \right. \\ &\quad \left. \left\langle B_y^2 \right\rangle \left({v'_x}^2 \left\langle sin^2\phi \right\rangle + {v'_y}^2 \left\langle cos^2\phi \right\rangle \right) + \left\langle B_z^2 \right\rangle v_z^2 \right) - 1 \end{aligned} \tag{B.6}$$

Regrouping terms, we obtain:

$$\begin{aligned} D_v &\propto 3\left({v'_x}^2 \left(\left\langle B_x^2 \right\rangle \left\langle cos^2\phi \right\rangle + \left\langle B_y^2 \right\rangle \left\langle sin^2\phi \right\rangle \right) + \right. \\ &\quad \left. {v'_y}^2 \left(\left\langle B_y^2 \right\rangle \left\langle cos^2\phi \right\rangle + \left\langle B_x^2 \right\rangle \left\langle sin^2\phi \right\rangle \right) + v_z^2 \left\langle B_z^2 \right\rangle \right) - 1 \end{aligned} \tag{B.7}$$

From (B.7) we can define an effective rhombicity R' and compare it to the rhombicity of the overall alignment frame, R:

$$\begin{aligned} \frac{R'}{R} &= \frac{\left(\left\langle B_x^2 \right\rangle \left\langle cos^2\phi \right\rangle + \left\langle B_y^2 \right\rangle \left\langle sin^2\phi \right\rangle \right) - \left(\left\langle B_y^2 \right\rangle \left\langle cos^2\phi \right\rangle + \left\langle B_x^2 \right\rangle \left\langle sin^2\phi \right\rangle \right)}{\left\langle B_x^2 \right\rangle - \left\langle B_y^2 \right\rangle} \\ &= \left\langle cos^2\phi - sin^2\phi \right\rangle \end{aligned} \tag{B.8}$$

The magnitude of the scaling factor $\left\langle cos^2\phi - sin^2\phi \right\rangle$ depends on the probability distribution of the wobble angle, ϕ. As an example, we will now consider the case where the

displacement angle ϕ is normally distributed: $P(\phi) = \frac{1}{\sqrt{2\pi\sigma^2}} e^{\frac{-\phi^2}{2\sigma^2}}$ where σ is the standard deviation in ϕ. Note that the mean of ϕ is always zero by definition. We can now calculate:

$$\frac{R'}{R} = \langle cos^2\phi - sin^2\phi \rangle = \int_\phi (cos^2\phi - sin^2\phi) P(\phi) d\phi \tag{B.9}$$

A numerical integration of (B.9) for several values of the standard deviation σ shows that a normal distribution of the wobble angle ϕ with a standard deviation of 40^o results in a scale factor of 0.3 (i.e. the rhombicity of the wobbling domain is scaled down by a factor of 0.3 relative to the rhombicity of the overall molecule.) This corresponds to the scaling observed for the amino terminal of MerB relative to the whole MerB/Hg/DTT complex ($R'/R = 0.17/0.50 \sim 0.3$), so the residual dipolar couplings observed in the MerB/Hg/DTT complex are consistent with a wobbling of the amino terminal domain with respect to the rest of the protein about the Z axis of the principal alignment frame with a normally distributed displacement angle of 40^o standard deviation.